PADERBORN UNIVERSITY

The University for the Information Society

Design and characterization of silicon nanophotonic elements

Dissertation zur Erlangung des akademischen Titels

doctor rerum naturalium

(Dr. rer. nat.)

vorgelegt

der Fakultät für Naturwissenschaften der Universität Paderborn

von M. Sc. Jinlong Lu

März 2022

Kurzfassung

Ähnlich wie die Entwicklung von Feldeffekttransistoren, die im 20. Jahrhundert zur Miniaturisierung elektronischer Geräte führte, wird die Miniaturisierung photonischer Systeme durch die Nachfrage nach Hochgeschwindigkeitsdatenübertragung und rein optischem Computing vorangetrieben. In letzter Zeit sind nanophotonische Elemente aus Silizium (Si) auf diesem Gebiet von großem Interesse, da sie möglicherweise mit der gut entwickelten Nanofabrikationstechnologie und einigen bereits vorhandenen Geräten kompatibel sind. In dieser Arbeit werden topologische photonische Kristalle (TPhCs) und mit Si realisierte Metaoberflächen verwendet, um die Lichtausbreitung in verschiedenen Anwendungen nach der Miniaturisierung bis in den Nanobereich zu untersuchen.

Erstens sind TPhCs basierend auf der Theorie der schwachen Topologie so konzipiert, dass sie robuste und vielseitige topologisch geschützte nulldimensionale (0D) lokalisierte Moden bei optischen Frequenzen erreichen. Die Lichtlokalisierung in der Mitte der Bandlücke wird durch streuende optische Nahfeld-Rastermikroskopie (s-SNOM) in einem TPhC verifiziert, das mit einer nichttrivialen Zak-Phase und einer Kantenversetzung konstruiert ist. Wir zeigen, dass aufgrund der schwachen Topologie unterschiedlich ausgedehnte Versetzungszentren eine ähnlich starke Lichtlokalisierung mit einstellbaren Lokalisierungseigenschaften induzieren, was ein vielseitiges Design mit einem Konzept der schwachen Topologie für verwandte Anwendungen bietet.

Darüber hinaus nutzen wir einen neuen Freiheitsgrad zur Realisierung eines topologisch geschützten Lichttransports in sogenannten talabhängigen photonischen Kristallen (VPCs), entwickeln mehrere Designs mit topologisch geschützten Moden und verifizierten experimentell die Vorteile von VPCs für die On-Chip-Lichtkontrolle in Silizium auf Isolator (SOI) Materialsystemen. Dieser Freiheitsgrad bietet die Möglichkeit, verschiedene komplexe Funktionalitäten zu erhalten, d. h. topologisch geschützte Resonatoren und Strahlteiler, die wichtige Komponenten für photonische integrierte Schaltungen sind. Mit den verifizierten Ergebnissen der klassischen Lichtmessung möchten wir unser Design auf quantenoptische Systeme erweitern, was sehr vielversprechend ist, um robuste quantenintegrierte optische Schaltungen mit Photonenerzeugung, -übertragung und -interferenz in kleinflächiger topologischer Photonik zu erhalten.

Obwohl nanophotonische Elemente vielversprechend für die Lichtkontrolle im Nanomaßstab sind, gibt es entscheidende Probleme und Herausforderungen, die Systeme vor Staub zu schützen oder die unvermeidliche Kontamination zu reinigen, die während des täglichen Gebrauchs auftritt. Hier bringen wir die optischen Elemente durch eine Veränderung

der Benetzbarkeit einen Schritt weiter in reale Anwendungsumgebungen mit einer vielseitigen dielektrischen Metaoberfläche als Beispiel. Der superhydrophile Zustand profitiert von dem speziellen Benetzbarkeitsdesign und ermöglicht eine verbesserte optische Reaktion, während der quasi-superhydrophobe Zustand den empfindlichen Strukturen die Fähigkeit verleiht, Staubkontamination relativ einfach zu entfernen. Darüber hinaus kann zwischen dieses beiden Benetzbarkeits- bzw. Funktionszustände durch entsprechende Behandlungen leicht und stabil geschaltet werden.

Abstract

Similar to the development of field-effect transistors that led to the miniaturization of electronic devices in the 20th century, the miniaturization of photonic systems is driven by the demand for high-speed data transmission and all-optical computing. Recently, silicon (Si) nanophotonic elements are of great interest in this field as for the potential to be compatible with the well-developed nanofabrication technology and some devices already in place. In this thesis, topological photonic crystals (TPhCs) and metasurface realized with Si are used to investigate the light tailoring performance in various applications after the miniaturization of the devices' size down to the nanoscale.

First, based on the weak topology theory, TPhCs are designed to achieve robust and versatile topologically protected zero-dimensional (0D) localized modes at optical frequencies. The mid-bandgap light localization is verified by scattering-type scanning near-field optical microscopy (s-SNOM), in a TPhC that is designed with a nontrivial Zak phase and an edge dislocation. We show that due to the weak topology, differently extended dislocation centers induce similarly strong light localization, with adjustable localization properties, providing a versatile design using a weak topology concept for related applications.

Further, taking advantage of a new degree of freedom for realizing topologically protected light transport in the valley-dependent photonic crystals (VPCs), we designed several devices with topologically protected modes and experimentally verified the advantages of VPCs for on-chip light control by fabricating them with silicon on insulator (SOI) material. This degree of freedom provides the possibility to obtain different complex functionalities, i.e., topologically protected resonators and beam splitters, which are important components for photonic integrated circuits. With the verified results obtained by classical light measurement, we seek to extend our design to quantum optical circuits, which is highly promising to obtain robust quantum integrated optical circuits, with photon generation, transfer, and interference in small area topological photonics.

On the other hand, although nanophotonic elements are promising for light control at the nanoscale, this also gives rise to the crucial problem and challenge of protecting the devices from dust or cleaning the unavoidable contaminants that appear during daily usage. Here, we make the devices one step further to real application environments with a versatile dielectric metasurface as an example. Benefiting from the special wettability design, the superhydrophilic state enables an enhanced optical response, while the quasi-superhydrophobic state imparts the fragile antennas the ability to self-clean dust contamination. These two wettability or functional states can be easily switched and repeated stably by appropriate treatments.

Declaration

I hereby declare that this work is based on my work and effort, and it has not been submitted anywhere for any other degree or professional qualification. If other sources of information have been used, they have been acknowledged.

Some of these works have already been published in peer-reviewed journals. A list of included publications can be found in the appendix.

30th, March, 2022, Paderborn
Jinlong Lu

List of Abbreviations

A list of abbreviations is shown below to define all abbreviations used in this thesis.

Abbreviation	**Meaning**
Si	Silicon
TPhCs	Topological photonic crystals
D	Dimensional
s-SNOM	Scattering-type scanning near-field optical microscopy
VPCs	Valley-dependent photonic crystals
SOI	Silicon on insulator
CMOS	Complementary metal-oxide-semiconductor
BZ	Brillouin zone
SSH	Su–Schrieffer–Heeger
QSH	Quantum spin Hall
QVH	Quantum Valley Hall
T	Time reversal symmetry
EBL	Electron beam lithography
NA	Numerical aperture
HOTIs	Higher-order topological insulators
PECVD	Plasma-enhanced chemical vapor deposition
S_2	Second-order normalized amplitude
AFM	Atomic force microscope
PCM	Phase changing material
Q	Quality factor
THG	Third-harmonic generation
OPO	Optical parametric oscillator
CA	Contact angle

ODP	Octadecylphosphonic acid
RCWA	Rigorous coupled-wave analysis
ITO	Indium tin oxide

Contents

Kurzfassung I

Abstract III

Declaration IV

List of Abbreviations V

Contents VII

1. Introduction 1

2. Introduction to Si nanophotonic elements in photonic crystals and metasurfaces 5

2.1 Development of Si nanophotonics 5

2.2 Introduction to TPhCs 7

2.2.1 Topology of the band structure and realization in photonic crystals 7

2.2.2 Several topological models in the optical range with Si 12

2.2.3 Some applications of Si TPhCs 16

2.3 Introduction to Si metasurfaces 20

2.3.1 Introduction to metasurfaces and the working principle 20

2.3.2 Typical applications of Si metasurfaces 22

2.3.3 Multifunction metasurfaces to meet more requirements 25

2.4 Fabrication of Si-TPhCs and Si-metasurfaces 26

2.4.1 EBL introduction 26

2.4.2 Plasma dry etching 28

2.5 Conclusion 30

3. Si TPhCs with 0D light localization protected by weak topology 33

3.1 Recent progress of topologically protected lower-dimensional localization 33

3.2 Introduction to the weak topology 35

3.3 Defect design and localization from weak topology 36

3.3.1 Band structure topology from different ways of unit cell selection 36

3.3.2 Edge states in the TPhCs based on the SSH model 38

3.3.3 Comparison of nontrivial and trivial designs with a dislocation 39

3.3.4 Versatility of localization achievement for different dislocation extensions 41

3.3.5 Characterization of the localization from simulation 44

3.3.6 Simulation results for more trivial and versatile cases 47

3.3 TPhC fabrication and optical near-field measurements 49

3.3.1 TPhC fabrication 50

3.3.2 Near-field measurement and data processing 51

3.3.3 Spectral comparison between simulation and experiment 53

3.4 Conclusion and outlook 57

4. TPhCs with QVH phase for integrated optical circuits 59

4.1 Prospects and recent progress of TPhCs in integrated quantum optical circuits 59

4.2 Design of the VPCs 60

4.2.1 Band structure analysis and valley Chern number 60

4.2.2 Kink states and robust light transmission 62

4.2.3 Resonator and beam splitter design based on VPCs 64

4.3 Characterization of the on-chip light control with VPCs. 67

4.3.1 Sample fabrication 67

4.3.2 Characterization of classical light transmission with VPCs 71

4.3.3 Observing the kink states by THG 72

4.4 Conclusion and outlook 74

5. A Si metasurface enabling both self-cleaning and dynamic color response 77

5.1 Some recent achievements of metasurfaces with wettability design 77

5.2 Design of metasurfaces with superwettability and obvious optical response 79

5.2.1 Selection of antennas for the metasurface and design criteria for supporting structures 80

5.2.3 Fabrication strategy toward the real situation 83

5.3 Experiment characterization of the multifunction metasurface 84

5.3.1 Sample fabrication 84
5.3.2 Wettability performance 85
5.3.3 Optical response and self-cleaning performance of the metasurface 86
5.3.4 Stability working of the multifunction metasurface 92
5.4 Conclusion 96
6. Conclusion and outlook 97
Acknowledgments 101
Appendix 103
A. Simulation of band structure with COMSOL and data plotting 103
B. Zak phase calculation from simulation 106
C. Grating coupler simulation with COMSOL and measured grating efficiency 108
D. Optimizing the fabrication of partly etched grating coupler 112
E. Reflective spectrum simulation with RCWA method 113
F. Scientific publications 114
References 115

1. Introduction

The 21st century is considered the era of photonics and optics, like electronics in the last century. During the development of electronic devices in the last decades, it is the presence of field-effect transistors that led to the miniaturization of complex integrated circuits on a small scale and has enabled the unprecedentedly powerful mobile phones and laptops today. In contrast to electronic devices, photonic devices are believed to possess several advantages like immunity from electromagnetic interference, low-loss, and high-speed transmission, large bandwidth, and so on, which grant them great superiority for signal transmission and data processing.[1, 2] Similar to complex electronic devices that are constructed by lots of basic components at the nanoscale, the miniaturization of optical elements is driven by the demand for fast information processing and the expectation to realize similarly commercial all-optical devices, like computers for data processing.

As for the miniaturization of optical systems, silicon (Si) nanophotonic elements are of special interest because of the well-developed nanomanufacturing technologies already available and can be used to integrate with some already existing electronic circuits easily if required.[3] This possibility of components integration to small areas will enable the possibility to produce photonics and electronics in the same wafer at high resolutions for industrial production. Different functionalities are included with these integrated optical systems so that the goal to realize all-optical computing can be moved one step further. In addition, during the integration and miniaturization of the optical system, an important branch of this field is based on the on-chip integration of nanophotonic structures with silicon on insulator (SOI) material, which is traditionally realized with optical waveguides in the early states.[4, 5] These waveguides are the most important basic-element of photonic integrated devices, which connect different functional parts and transmit light information between them. Regarding the on-chip integration, one always needs to consider the design and fabrication of several nanophotonic components on the same substrate with the wave optics principles. However, an important issue we need to consider is the light loss inside the structures, especially for some designs with the presence of sharp bending if one needs to realize highly integrated systems. Furthermore, most nanophotonic elements are very sensitive to fabrication deviations or disorders, which give crucial requirements for real fabrication and final realization. To achieve high performance compact integrated system, the above crucial requirements for fabrication and transmission loss have to be reduced.

Recently, the presence of topological nanophotonics is revolutionizing this field for light guiding, with light transmission across sharp bending without loss or functional devices that are robust to fabrication deviation or disorder under the topological protection.[6-9] In this field, a lot of models and applications have been realized, such as the Su–Schrieffer–Heeger (SSH) model,[10, 11] the quantum Hall model,[9] the quantum spin Hall (QSH) model,[12] and the quantum

valley Hall (QVH) model.[13, 14] Based on these topologies, various researchers have demonstrated unexpected optical behavior in a variety of platforms like photonic crystals, waveguides, and resonators. To date, progresses in topological photonics based on Si already found lots of applications like robust light guiding, photonic routing, photon-pair generation, and spatial entanglement at optical wavelengths, all of which foresee a bright future for the integrated optical circuits.[4, 15, 16] However, as an especially new research field that just started in 2008, these researches are just the tip of the iceberg, and much more interesting phenomena remains to be further studied and unlocked.

Another form of an optical device that is important for the miniaturization of optical systems is based on the well-known metasurfaces, which are artificial planar optical-components that consist of nanostructured periodic structures with carefully designed metallic or dielectric building blocks.[17-19] Compared to conventional optical elements that accumulate changes in amplitude, phase, or polarization while light propagates along the optical path, metasurfaces can be used to tailor these electromagnetic properties abruptly within sub-wavelength structures. After the development for more than 10 years, it is now possible to design and fabricate a deterministic arrangement, shape, and orientation of these so-called meta-atoms to apply substantial optical modulation to an incident electromagnetic wave and reduce lots of devices to a minimum size.

Based on these two forms of nanophotonic elements and the advantages of Si for the application in this field, the paper aims to design and characterize the performance of Si nanophotonics in related applications. It is structured as follows: Section 2 focuses on the building blocks for topological photonic crystals and the working principles of metasurfaces. Starting from the topology in mathematics and condensed matter, we make it clear how these models can be transferred and realized in classic waves, especially with Si. Recent progress and typical applications in TPhCs are also introduced. Further, the working principle, typical design strategy, applications, and recent requirements of metasurface are also introduced. Finally, the two most important steps in the fabrication of Si nanophotonic elements, i.e., electron beam lithography (EBL) and plasma dry etching are induced in detail.

Section 3 provides one of our major achievements in optical localization at the sub-wavelength scale with a weak topology design. Based on the weak topology theory, TPhCs are designed to realize robust and versatile topologically protected zero-dimensional localized modes at optical frequencies. Further, we use scattering-type scanning near-field optical microscopy (s-SNOM) to verify the mid-bandgap light localization, in a TPhC with a nontrivial Zak phase and an edge dislocation. We show that due to the weak topology, differently extended dislocation centers induce similarly strong light localization. We believe these results lay a foundation for the application of TPhCs based on weak topology in active topological nanophotonics, and nonlinear and quantum optic integrated devices due to their robust light localization.

Section 4 focuses on the advances in the manipulation of light on-chip with TPhCs. Taking advantage of the valley-dependent photonic crystals (VPCs), which provide a new degree of freedom for realizing topologically protected robust light transport. We simulate the topologically protected kink states and experimentally verified the VPCs for on-chip light control by fabricating devices with SOI material. Furthermore, the new degree of freedom provides the possibility to obtain more complex functionalities, i.e., topological protected resonator and beam splitter, which are important fundament components for on-chip photonic integrated circuits. With the verified results by classical light measurement, we seek to extend our design to quantum optical circuits, which is highly promising to obtain robust quantum integrated optical circuits, with photon generation, transmission, and interference in a single substrate with a small area.

In section 5, we present another work based on amorphous Si (a-Si) metasurface, which aims to protect fragile nanophotonic elements. By embedding the metasurface inside a large area of wettability supporting structures, we obtained superhydrophilic or quasi-superhydrophobic states for the metasurface, which is highly efficient in fabrication, and achieves both optical and wettability functionality at the same time. Here, the superhydrophilic state enables an enhanced optical response with water, while the quasi-superhydrophobic state imparts the fragile antennas an ability to self-clean dust contamination. Furthermore, the metasurface can be easily switched between these two wettability or functional states by appropriate treatments in a repeatable way, without degrading the optical performance. The proposed design strategy will bring opportunities to smart nanophotonic elements with improved performance, versatility, and physical stability.

In Section 6, we summarize all the work in this thesis, highlighting the remaining challenges and the unique opportunities that can be pursued using Si nanophotonic elements.

2. Introduction to Si nanophotonic elements in photonic crystals and metasurfaces

Si nanophotonic elements may provide a low-cost approach to overcome the drawbacks of the high data rate transmission in traditional electronic circuits, which is realized by replacing the widely used electronic connections with photonic integrated circuits and devices. Although most of the commercial applications are still underway, this perspective already gave a huge impetus to the development of Si nanophotonics in recent years. Among them, shrinking the device size down to the nanoscale is extremely useful for devices integration stands out, similar to the integrated electronic circuits that highly increase the convenience of our daily life nowadays. In this chapter, starting from the development and prospect of Si-based nanophotonic elements, we will focus on some fundamentals and recent progress of two kinds of them, i.e., TPhCs and metasurfaces. These two forms of nanophotonic elements are extremely important and widely explored in the past few years, we try to summarize some recent progress and make it clear why they are useful for optical devices at the nanoscale and further system integration.

2.1 Development of Si nanophotonics

As one of the most important materials in the electronic industry, Si has been used in a lot of electronic devices for more than 40 years. Although the development of electronic processors can still follow the well-known Moore's law and meet most of our current applications, more precise lithography techniques or the employing of multi-core structure design should be employed to achieve this goal. However, if bandwidth requirements increase further, parasitics in metal interconnects gradually become a major obstacle, as electrical signal attenuation and power consumption rise sharply with data transfer rates.[1, 2, 20] Fortunately, optical interconnection is thought to be a promising solution that can overcome the bottleneck of the high-speed data transmission and processing with electronic devices, which is realized by carrying the information signals with photons instead of electrons. Photons have zero mass and charge, which guarantees that they can travel at a velocity of light without interference with the electromagnetic field. This is one of the most important advantages of all-optical information processing, which means optical systems are possible to achieve a much higher processing rate and better stability than electrical systems. Indeed, the recent development of optical nanodevices is promoted by the desire to replace traditional electrical systems with integrated optical circuits for data transmission or processing.[20-22]

On the other hand, when applied for the transmission of the light signal, Si has an apparent window approximately in the infrared range, which is a quite broad range and at the same time

includes the well-developed telecommunication band from 1300–1550 nm.[3] Lots of excellent optical properties, like excellent thermal conductivity and large optical damage threshold, have been proved during the development of Si in optical systems. In addition, the mature complementary metal-oxide-semiconductor (CMOS) techniques have been well-developed for several decades, allowing for the large-scale manufacturing of Si nanophotonic elements and further integration with some electronic devices already existed. All of these advantages select Si as a highly remarkable candidate for applications in integrated photonics.[4, 20, 23]

The above advantages of Si photonics have been explored for a long time, which can be traced back to the mid-1980s. They can be applied to design high-performance waveguides and modulators, or integrated with other functional components to realize more complex circuits.[21] In recent years, obvious performance improvements like ultrafast Si modulators and detectors have also been achieved due to the rapid progress of nanofabrication technology. Furthermore, great breakthroughs in some more complex devices, such as Si sources, and epitaxial devices that are directly grown on Si substrate, have been made into light sources.[21] These technical advances with both light sources and transmission on one single Si substrate are considered great features for optical integrated systems if we want to achieve the goal of all-optical computing.[23] More recently, the progress of metasurfaces provides idea solutions to control and couple light into these on-chip systems. Just as the vision of a future on-chip integrated optical system shown in Figure 2.1, a single Si substrate can be used to integrate different functional parts for optical information processing like the integrated electric circuit we see now.[23]

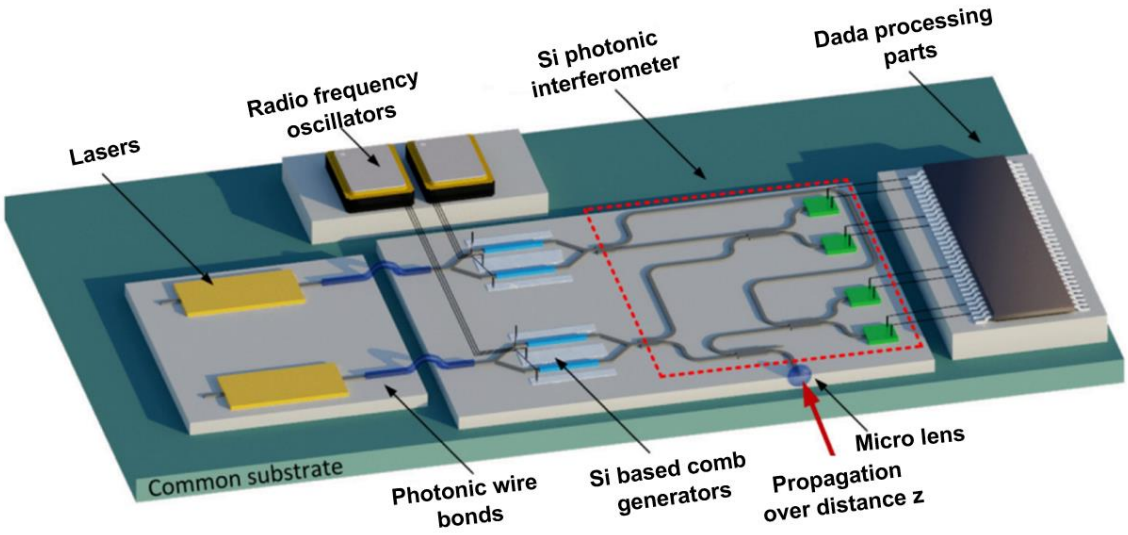

Figure 2.1 Illustration of a future on-chip integrated optical system. The system comprises laser sources, Si-based frequency comb generators, and an interferometer with photodetectors. The electronic components are not fully depicted in the picture, RF oscillators are used to drive the comb generators, readout, and processing circuitry. Here, different elements can be integrated on the same substrate like Si. Electrical connections are realized by standard techniques we use nowadays, while the light transmission is mainly realized by single-mode waveguides. Furthermore, microlenses can be fabricated at the edge of the chip to collimate the light into and out of the device. The figure is taken from Ref. 23.

However, despite these breakthroughs and the fact that lots of novel optical devices have been achieved based on Si in the past few years, there still exist some challenges for the further development of this field. Among these challenges, the scattering and transmission loss in the optical system, and how to shrink some basic components down to the nanoscale for better integration stand out. Fortunately, the presence of TPhCs, which we investigate in our thesis foreshows a bright future to eliminate the energy loss in optical systems and also provides solutions to achieve a compact design layout for topological protection even in the presence of sharp corners.[7-9, 24]

While the other kind of optical device, metasurfaces, could provide lots of functional designs with Si nanoantennas at small sizes for more device integration. However, the real application of metasurfaces for most cases still needs more effort, like how to realize more functionalities with improved physical stability as introduced later in this Chapter.

2.2 Introduction to TPhCs

TPhCs originated from ideas that were first developed in solid-state physics, which began from the discovery of the quantum Hall effect in the 1980s.[25] Later, Haldane and Raghu made the most important theory verification that topological band structures are, in fact, a ubiquitous property of waves inside a periodic medium, regardless of the classical or quantum nature of the waves, and paved the way for TPhCs in classical waves.[26] In the past decades, TPhCs are getting more and more attention to not only explore the topological theory but also as a promising platform to control the behavior of light that is robust immune to fabrication or backscattering.[27] Here, we will introduce some fundamentals of topological theory. First, the topology concept, or more specifically, the band structure topology in condensed matter and classical waves is introduced. Then, some basic concepts like the Berry phase, topological invariants, and bulk boundary correspondence are included later. Further, we explain how the topology that is discovered in condensed matter physics can be transferred to classical waves, especially based on the platform with Si photonic crystals is explained by band structure introduction. Finally, several frequently used models that can be realized for optical wavelengths and related applications are introduced with more detail.

2.2.1 Topology of the band structure and realization in photonic crystals

Topology is originated from the mathematical study of the shape properties that are invariant or not through the deformation of an object. Based on the definition in this field, two objects that have the same topological invariants are topologically equivalent, for example, the sphere and spoon (Figure 2.2). They are considered topologically equivalent is because the topological invariants are defined by the number of holes for the geometry shape (both with zero holes). Accordingly, a donut and a cup are also topologically equivalent with only one hole, and the same for the last group with two holes. With this classification, objects can be transformed into each other freely by a continuous deformation if they are considered

topologically equivalent. In contrast, deformations like cutting and tearing are possible to change the topological invariant of an object. Correspondingly, these deformations that change the topological invariant abruptly are called discontinuous transformations.

This topological invariant determined by the number of holes in a real geometry shape is based on the well-known Gauss-Bonnet theorem, which is connected to the total Gaussian curvatures (K) of a 2D closed surface and is always an integer. It is named as genus (g), or the number of holes within this shape, with the relation of them is:[7]

$$\frac{1}{2\pi}\int KdA = 2(1-g), \tag{2.1}$$

where the integration is over the whole surface of the geometry.

Figure 2.2 Illustration of the classification of topology in real geometry. Six objects can be grouped into three pairs based on whether the topology is the same or not. Objects that have the same topological invariant (the number of holes in real space) are put together in each group.

1. Understanding the band structure topology with quantum Hall effect

Similar to the topological invariants in real space, topology can also be defined on the dispersion bands in reciprocal (wave vector) space. The quantity of topological invariant in reciprocal space is the same as the determination and calculation of holes in the real space above. This characterization gives rise to the well-known topological insulator, which behaves as an insulator in the interior but with conducting states on the boundary. This can be understood intuitively, as the band structure of two topologically equivalent insulators can transform into each other by a continuous deformation like real space, and the bandgap remains open during this deformation.[7, 8] In contrast, if two systems are topologically inequivalent, for example, a topological insulator and a traditional insulator cannot be transformed into each other adiabatically. Instead, they can only be transformed into each other if the bandgap is closed and reopened again, this process is known as a topological phase transition. The close of the bandgap ensures these gapless boundary modes or edge states at the interfaces between two topologically inequivalent band structures. In addition, the existence of these edge states across the bandgap is closely related to the bulk topology, with the number of them is equal to the difference between their topological invariants. This relation is the so-called bulk-boundary correspondence, which provides the relation between the number of lower-dimensional modes

(or edge states) and the topology of the band structure.[8]

This classification was first discovered in condensed matter physics for the well-known quantum Hall effect, which is especially important for the understanding of topology in the band structure. In this model, an out-of-plane strong magnetic field is applied to the electrons, which are then flowing in a unidirectional way along the edge of the system. In this situation, the Hall conductance only takes the quantized values h/e^2C, in which e is the electron charge, h is the Plank constant, and C is the quantized integer, corresponding to the topological invariant of the system.[8] Similar to the calculation of the number of holes in real space with the Gauss-Bonnet theorem, in the quantum Hall effect, the topological invariant is the well-known Chern number, which is defined as a surface integral over the entire Brillouin zone (BZ) with similar form. The strong magnetic field breaks the time-reversal symmetry of the electronic gas, which resulted in the nonzero Chern number. But outside the electronic gas, the system is trivial with a zero Chern number, this means a unidirectional transport of the edge of the physical boundary is observed in the quantum Hall effect due to the difference in topology. The integral to calculate the Chern number is expressed as

$$C = \frac{1}{2\pi}\oint F(\boldsymbol{k})d\boldsymbol{k} \tag{2.2}$$

The parameter $F(\boldsymbol{k})$ in Equation (2.2) is the so-called Berry curvature defined as $F(\boldsymbol{k}) = \nabla_{\boldsymbol{k}} \times A(\boldsymbol{k})$, and $A(\boldsymbol{k}) = \langle u(\boldsymbol{k})|i\nabla_{\boldsymbol{k}}|u(\boldsymbol{k})\rangle$ is the Berry connection, $|u(\boldsymbol{k})\rangle$ is the periodic Bloch function.[7, 8]

Here, the Berry phase (also known as the geometric phase) occurs in a quantum mechanical system when adiabatically traversing a closed path in the parameter space of the system, with the system does not return to its initial state. And this phase factor its wave function receives during this adiabatically traversing process includes the Berry phase can be analyzed below. For example, if a system at its initial state (described by H_0) changes with time adiabatically and goes back to its initial state after time T (where $H_0 = H_T$). The states of the particle at different times have the relation:

$$|\psi(T)\rangle = e^{i\gamma(T)}e^{i\int_0^T H(t)dt}|\psi(0)\rangle, \tag{2.3}$$

Where the phase change includes both a dynamical phase linked with time and a Berry phase $\gamma(T)$ determined by the momentum-space path, with the Berry phase that is gauge-dependent and cannot be eliminated by a gauge transformation.[28] This means the state remains in the corresponding initial state with $H_0 = H_T$, with the phase as the only change. With this definition, the Berry phase can be calculated by integrating the inner product of this state with the time derivative over a time interval:

$$\gamma_n(T) = \int_0^T i\langle n(t)|\partial_t n(t)\rangle dt. \tag{2.4}$$

In condensed matter, although the Hamiltonian is stationary in most cases, the particles do not acquire this phase concerning time. But the BZ naturally provides this condition for the presence of the periodicity in the momentum space. Then with a d dimensional periodical system, we will have a lattice momentum version of this Berry phase:[8]

$$\gamma_n = \oint i\langle n(\boldsymbol{k})|\partial_{\boldsymbol{k}} n(\boldsymbol{k})\rangle \cdot d\boldsymbol{k}, \tag{2.5}$$

The Berry phase is important in the determination of the topology of the band structure is because it provides the geometrical properties (in topology, the 2D BZ is topologically equivalent to a donut) of how these eigenstates $u(\boldsymbol{k})$ vary as a function of $\boldsymbol{k}$. While before bringing in the concept of band structure topology, the analysis of it is decided by the energy dispersion of each band barely, which is not complete to analyze a system.

2. Band structure and the topology in photonic crystals

Although topological insulators were firstly discovered in condensed matter systems, they are not the specific characteristic of quantum systems and can be also realized in classical systems based on a similar analysis. These researches extend similar models in condensed matter systems to classical waves starting with a path-breaking work from Haldane and Raghu. In their work, they propose the first idea to extend the well-known Chern topological insulators in condensed matter systems to classic waves systems with magnetically periodic media.[25, 26] Their work then sparked a search for topological phases and applications in classical systems from electromagnetics to acoustics and photonics. With these topological design ideas, classical wave systems are robust to defects and disorders similar to the robustness that is observed in the quantum Hall effect. On the other hand, classical topological systems provide a larger control of their space and time properties than electronic systems, which have been an ideal platform to investigate, design, fabricate and detect different kinds of topological effects that may not be straightforwardly observed in condensed matter systems.[8, 29]

Among these classical wave systems, photonic crystals stand out, which are designed to interact with the light wave in the same way that electrons in semiconductors. Similarly, the topological property of a photonic crystal is closely linked with its band structure in wave vector space. In traditional photonic crystals, the most interesting region is the photonic bandgap range where no states can exist for the photons to propagate, as this provides the possibility to control light in the photonic crystal. Accordingly, the bandgap during the design of TPhCs is also the most important one to achieve topologically protected modes inside the bandgap. Normally, the physics of the band structure in a photonic crystal can be understood by examining the dispersion diagram, which provides information on the possible interactions of electromagnetic fields in this system. In real cases, the band structure of photonic crystals can be calculated by commercial software. The band structure in this thesis is calculated by COMSOL as provided with more details in Appendix Part A.

3. Design of TPhCs with the photonic crystal slab

In ideal 2D photonic crystals, the z-direction is infinitely extended, but this ideal case can only be realized by fabricating periodical structures in a dielectric slab with finite thickness in the z-direction. The confinement of light for the vertical direction in these real structures is provided by the dramatically refractive index difference, while the in-plane confinement is realized with photonic crystal bandgap properties by unit cell design.[22] A combination of these two confinement mechanisms allows us to realize different optical modes based on a photonic crystal slab.

In a 2D photonic crystal slab, since the Bloch wave vector k is conserved, the bulk and in-plane components project a set of states which can radiate out of the plane. These states in the projected band diagram form the light cone as shown in Figure 2.3, which can be used to distinguish between leaky and non-leaky modes of a photonic crystal system.[22] Since the permittivity of the material used to form the photonic crystal is larger than that of air, guided modes that lie below the light cone can be confined and guided in the slab.

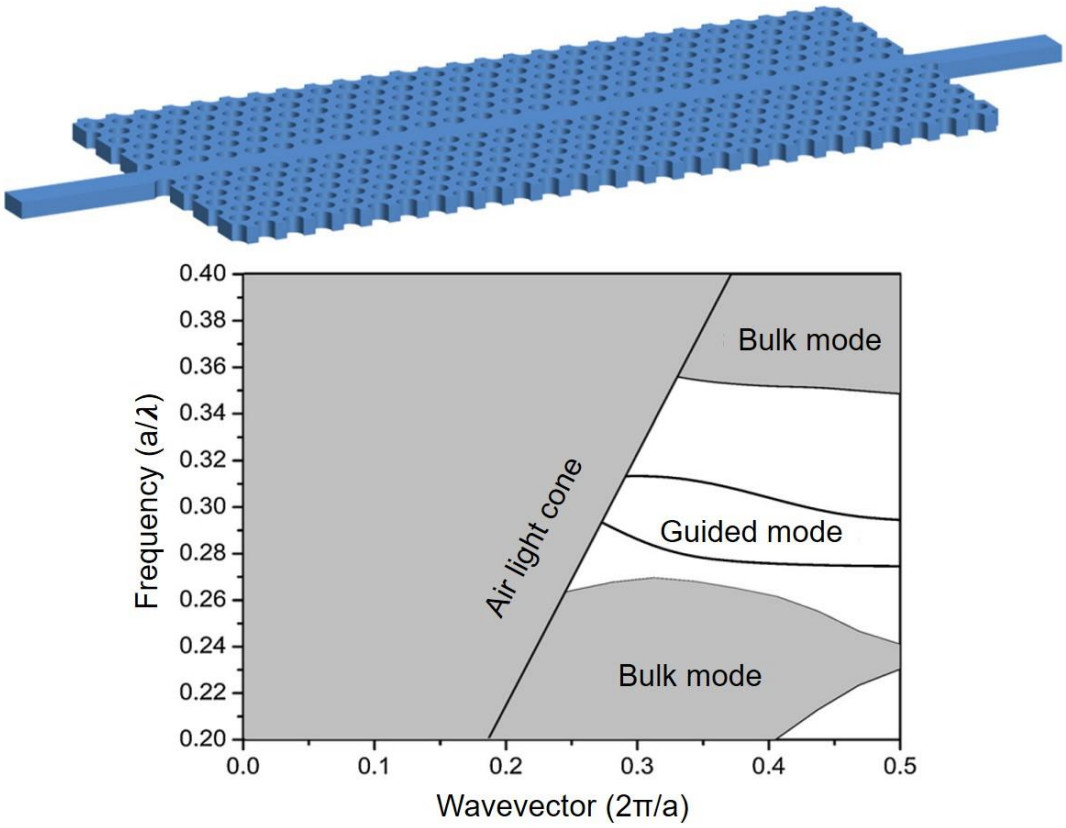

Figure 2.3 An example of the band structure from a 2D photonic crystal slab. The light cone is decided by the velocity of light due to the air surrounding it. In the bandgap, two guided modes are observed by designing a line defect in the photonic crystal (illustrated in the top row). Both modes can be used to transmit light inside the photonic crystal as they are below the light cone (bottom row in the band structure). a is the lattice constant of the photonic crystal, λ is the wavelength. Figures are taken from Ref. 22.

On the other hand, the polarization of the modes inside the slab can be either even or odd

if the photonic crystal has a horizontal plane of mirror-symmetry at the center of the slab. It's then important to note that a bandgap sometimes may appear for the even modes while no gaps appear for the odd modes in some special cases. During the design, another important thing that needs to be considered is the thickness of the photonic crystal slab and the regions below and above the slab, which play an important role in determining whether the bandgaps open or not. Based on the photonic crystal slabs with these design ideas, we can then design different applications related to their band structure, particularly the TPhCs we designed in this thesis, which is one specific application related to the topology.

2.2.2 Several topological models in the optical range with Si

To design TPhCs that work at optical wavelengths that we are interested in for all-optical information processing, Si is of great interest due to the advantages we introduced so far. Additionally, the selection of topological models that can be realized from design and fabrication is also important. Currently, most systems and applications with Si rely on the mature SSH, QSH, and QVH models, which are relatively easy to realize and have shown good performance. In addition, as we introduced above, TPhCs are also great platforms to investigate new topological phases beside them, such as high order phases, Floquet topological insulators, Dirac vortex method, and so on. Here, we only introduce the fundamentals of the three models and show how they can be used to design real devices for light control.

1. TPhCs based on the SSH model

The 1D SSH model is the most frequently used configuration for a 1D topological structure, where the topological invariant is determined by the Zak phase (Berry phase in the 1D case).[30] As shown in Figure 2.3A (top row), the model considers a periodic array with two sites in a single unit cell, and the coupling strength between intracell and intercell sites is different. By only considering the nearest-neighbor interactions between the individual cells in a chain, v and w (both are real numbers) can be used to represent the coupling coefficients for intra-unit cell hopping and inter-unit cell hopping, respectively.[30] The bulk Hamiltonian of this SSH model can be written as

$$\widehat{H} = v\sum_{m=1}^{N}(|m,B\rangle\langle m,A| + \text{h.c.}) + w\sum_{m=1}^{N-1}(|m+1,A\rangle\langle m,B| + \text{h.c.}) \qquad (2.6)$$

where, N represents the total number of structures, |m, B > represents one state of the chain on unit cell m, |m, A > is the other one in the unit cell, and *h.c.* represents the Hermitian conjugation. By solving for the eigenvalues of the above Hamiltonian, the band structure of the system is obtained. The physical meaning of the obtained band structure is that if the number of unit cells in a system is fixed, a specific point k in the Brillouin zone and the energy of the corresponding band are decided. The relations between them are shown in Equation (2.7) below:[30]

$$E(k) = \pm\left|\text{v} + e^{-ik}w\right| = \pm\sqrt{v^2 + w^2 + 2vw\cos k} \qquad (2.7)$$

Figure 2.3 below shows the dispersion of five hopping amplitudes based on Equation 2.7.

As long as the hopping amplitudes are different, an energy gap between the two bands is observed. However, the bandgap closes if $v = w$, which corresponds to a conductor. This dispersion relation is useful to understand a lot of physical properties of the bulk of the system like the classification of insulator and conductor. However, there is also important information about the bulk that it does not reveal completely, for example, the band structures in Figure 2.3 C and E are the same but show different behavior. This is not difficult to understand as stationary states do not only have wavenumber eigenvalue and energy, but also an internal structure. This internal structure of the eigenstates with momentum k can be given by the direction in which the vector $\boldsymbol{d}(k)$ points, with this $\boldsymbol{d}(k)$, read below:[31]

$$d_x(k) = v + w\cos k,$$
$$d_y(k) = w\sin k,$$
$$d_z(k) = 0. \tag{2.8}$$

As the wavenumber runs through the BZ, the path that the endpoint of the vector $\boldsymbol{d}(k)$ traces out is a closed circle of radius w on the d_x, d_y plane as shown in the lower row of each case in Figure 2.4. The topology of this loop can be determined by an integer known as the winding number, and an edge state arises in the nontrivial case when $v < w$. The winding number here and the Zak phase have a π factor difference (the Zak phase is π times the winding number).

In practice, precise control of the coupling (v and w) can be realized by lots of formats or configurations, including waveguides, ring resonators, and photonic crystals. For example, in the work of Blanco-Redondo et al., they investigate the use of Si waveguides in this model, and Si waveguides are acted as the dimer. By using a fixed separation distance between an array of parallel Si waveguides, the required alternating coupling strengths (v and w) can be implemented. Consider an array defined by a series of inter-element coupling, no bandgap exists in the band diagram if the constant coupling is designed in the whole array. A bandgap opens if we alternate the coupling strengths by changing the distance between the waveguides in the array. Here, the ratio of the intra dimer to inter dimer coupling is more than (less than) 1 corresponding to zero (π) Zak phase. And an edge state arises at the boundary between two regions with different Zak phases as for the difference from band structure topology.

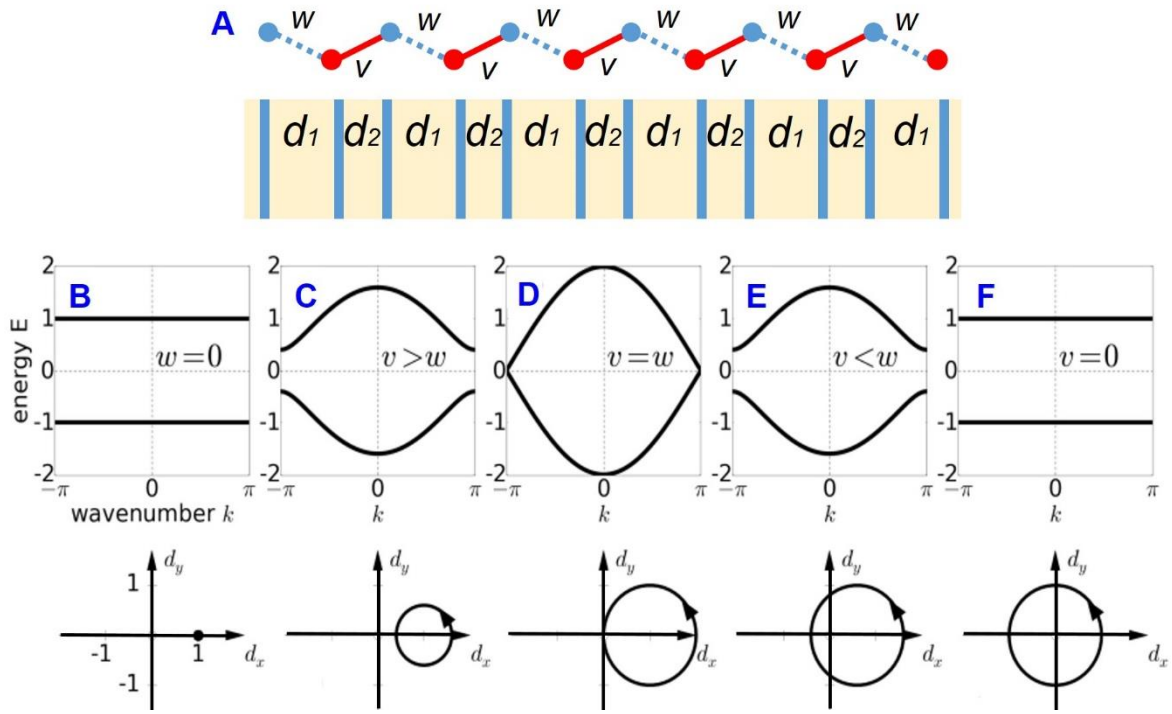

Figure 2.4 Topology in the 1D SSH model. (A) illustration of the 1D SSH model and realization with waveguide by distance tuning. The distance between the waveguides (d_1 and d_2) are used to tuning the coupling strength. (B-F) Dispersion relations of the 1D SSH model for five hopping amplitudes. (B) $w = 0$, $v = 1$; (C) $w = 0.6$, $v = 1$; (D) $w = v = 1$; (E) $w = 1$, $v = 0.6$; (F) $w = 1$, $v = 0$. In each case, the path of the endpoints of the vector ***d(k)*** (which representing the bulk momentum-space Hamiltonian), are also shown on the d_x, d_y plane, as the wavenumber is sweeper across the BZ. Figure B-F are taken from Ref. 31.

2. TPhCs based on the QSH model

For 2D TPhCs, the graphene lattice or "photonic graphene" is extremely important because of the Dirac cone, which is the most fundamental 2D point degeneracy with linear dispersions between two bands, and opening it properly can result in topologically protected states.[32, 33] First, a simple tight-binding lattice in a graphene lattice with two sublattices exhibiting different onsite energies is considered. The corresponding Hamiltonian of this graphene can be written as

$$H = t\sum_{\langle i,j\rangle} c_i^{\dagger} c_j + M\sum_i c_i^{\dagger} c_i \tag{2.9}$$

where $c\dagger$(c) is the creation (annihilation) operator, t is the nearest-neighbor coupling strength, and M is the difference of on-site energy. $\sum_{\langle i,j\rangle} c_i^{\dagger} c_j$ sum over nearest-neighbor sites, and ε_i is ± 1 when i is on different sublattices. The lattice here hosts massless Dirac cones at the corners of BZ if no on-site detuning ($M = 0$) is presented.

Based on this Hamiltonian, we can recognize that several approaches can be used to lift

the Dirac cones, which result in different topological phases.[33] For example, complex next nearest-neighbor couplings can be introduced to break the time-reversal symmetry (*T*) of the system and open a bandgap (Figure 2.5A). This approach corresponds to the well-known quantum Hall phase in the Haldane model, which is the first topological phase realized in photonics. Here, the quantum Hall phase is characterized by the Chern number that is introduced before, which provides a unidirectional edge state that is robust against certain perturbations like the quantum Hall effect. However, it is difficult to realize a quantum Hall phase at optical frequencies, as one needs to break *T*, with a widely adopted approach that applies gyromagnetic effect in related materials. But the weak effect at optical frequencies limits the applications in the optical range.

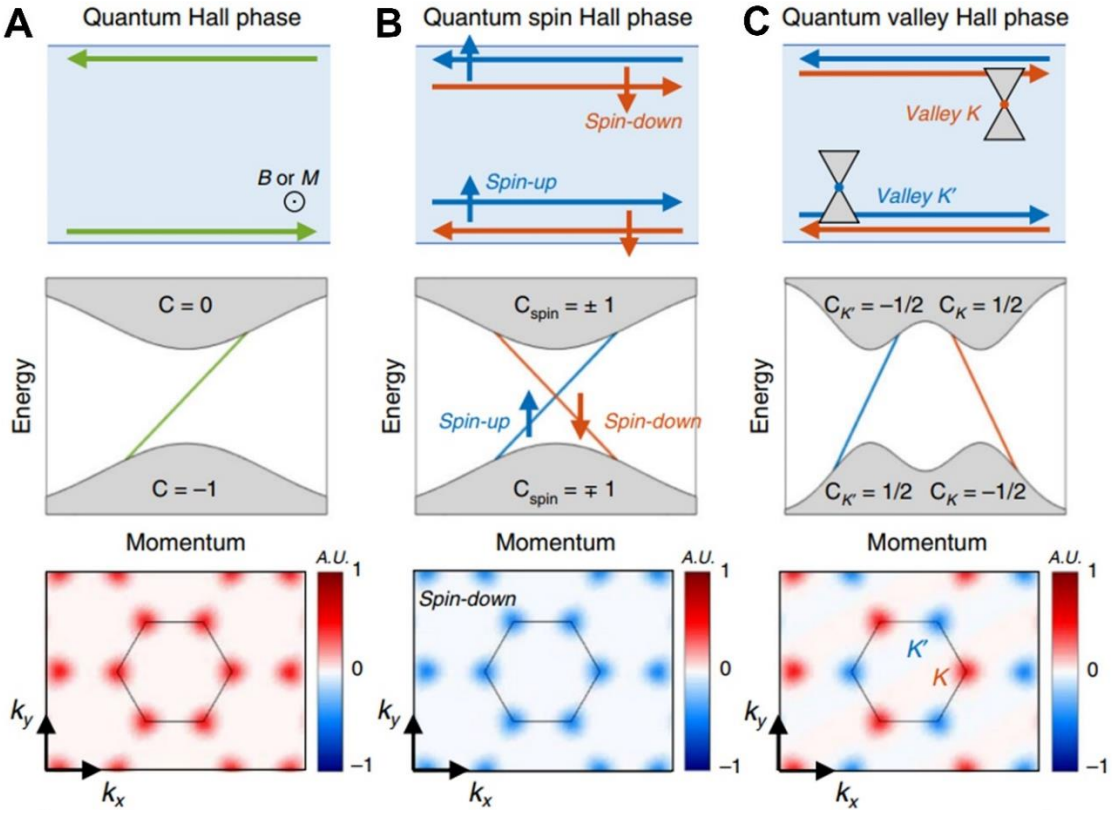

Figure 2.5 Illustration of the edge states and Berry curvature with honeycomb lattice. (A) Unidirectional propagation of edge states along the boundary is observed in the system with the quantum Hall phase. This unidirectional edge state shows a fixed sign of the group velocity in dispersion as shown in the lower row. The Berry curvature is nonzero, and the same for the Chern number. (B) Illustration of two helical unidirectional edge states along the boundary of a system with the QSH phase. The edge state dispersion shows different group velocities for spin-up and spin-down. In addition, the sign of Berry curvature for spin-up and spin-down is opposite, providing a nonzero spin Chern number but zero total Chern number. (C) Unidirectional propagation of edge states along the boundary of the system with the QVH phase. Different from the QSH phase, the edge state here has different group velocities for different valleys. The Berry curvature has a positive and negative value at the valleys, i.e., *K* and *K'*. Nonzero valley Chern number is obtained near *K* or *K'*. Figures are taken from Ref. 33.

Another topological phase that has been widely studied in photonics is the QSH phase, which is constructed by emulating QSH Hamiltonians (Figure 2.5B) with photonic pseudospins. In the electronic case of QSH, these helical edge states are protected by T with $T^2 = -1$. In photonic systems, although T cannot protect a QSH phase anymore (because $T^2 = 1$), one can still take advantage of combined freedom in photons, like a pseudo-time-reversal symmetry that involves spatial symmetries can be applied to realize similar topological protection. Similarly, two helical edge states with counter-propagating pseudospin states at the boundaries are observed, and this extra degree of freedom is important for light control.

3. TPhCs based on the QVH model

The third method to degenerate the Dirac points for the above Hamiltonian from photonic graphene is through the on-site energy detuning (i.e., $M \neq 0$), and the induced topological phase is a valley Hall phase (Figure 2.5C).[16, 34-36] Compared with quantum Hall or QSH phases, QVH phases do not break T or need pseudospins. If two sublattices of this honeycomb lattice are inequivalent, for example, by the reduction of spatial symmetry, the Dirac points will be gap out and result in a degree of freedom. For instance, the Berry curvature has opposite signs at the K and K' valleys, which can be attributed to an effective magnetic field leading to the well-known valley Hall effect, with K and K' each supporting an edge state. Recently, both theoretically and experimentally have demonstrated the existence of robust topologically protected valley Hall edge states on domain walls between two honeycomb lattices with inversion symmetry. And the edge states protected by the valley phase can travel across sharp corners without radiating into the bulk.

Normally, the popular VPC design with Si at optical frequencies is based on SOI material and started from a design with equivalently removed parts (i.e., circle or triangular), then spatial symmetry is broken by tuning some geometrical parameters that are easy to control.[36, 37] As more details about this design will also be introduced in Chapter 4 of this thesis, we would keep this part short here.

2.2.3 Some applications of Si TPhCs

1. Robust light transmission and classical integrated devices

The most well-known application of TPhCs is to achieve robust light transmission with topological protection by creating interfaces between the regions that possess two different topologies. This light-guiding ability is not only demonstrated to occur at sharp corners with minimal scattering but also to show a selective chiral coupling.[3, 36] For example, Parappurath et.al directly excited and observed topologically protected edge states at telecom wavelengths in a Si photonic platform with QSH. They further demonstrate that the pseudospin of the edge state is inherently encoded in the circular polarization of its far-field, and show that this strong spin-orbit coupling can be used to selectively excite topological states with a laser beam.

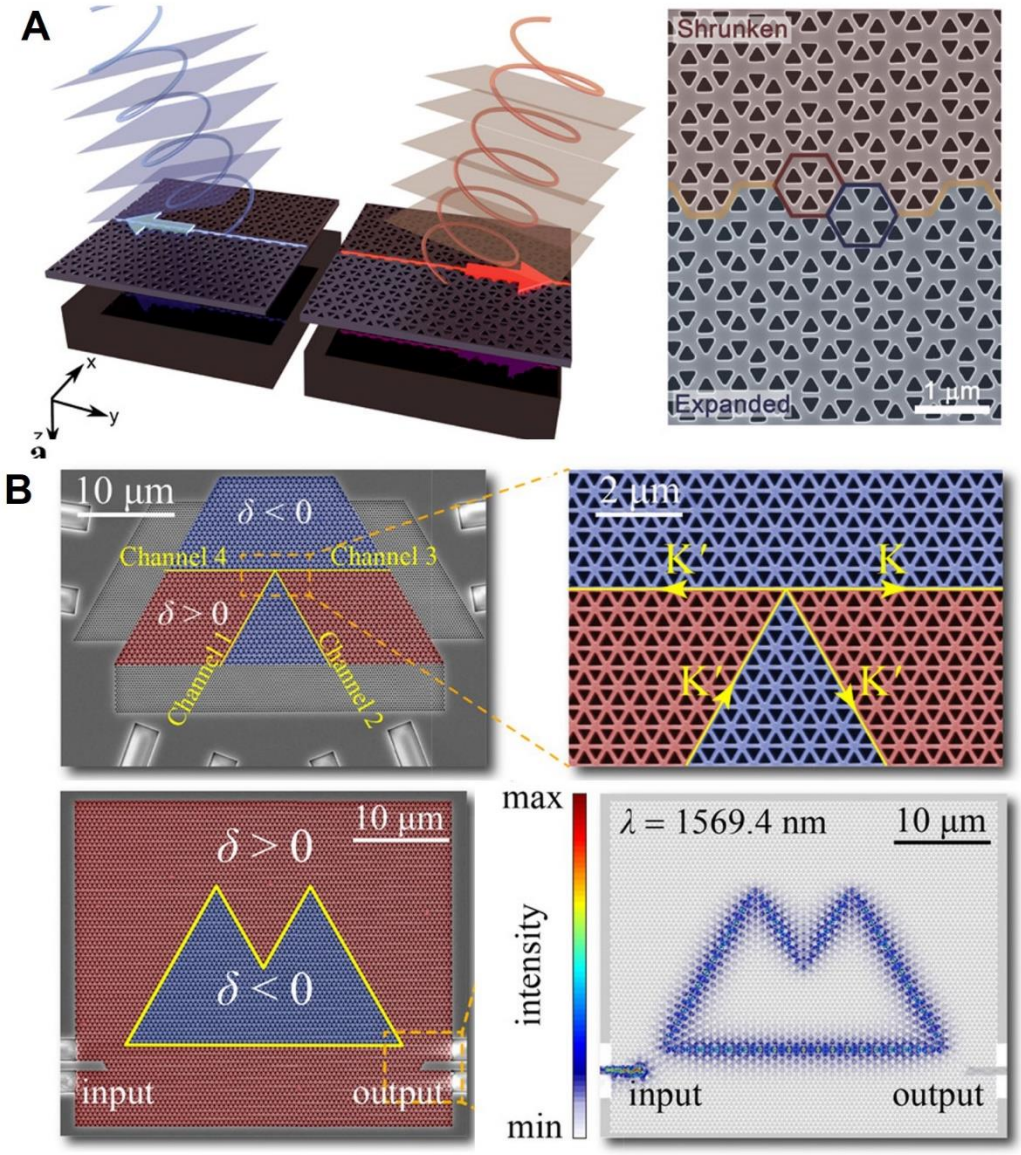

Figure 2.6 Application of TPhCs with QSH model and QVH model. (A) Spin-orbit coupling in topological photonic crystals. Chirality of the radiation field is connected to the propagation direction of topological photonic crystal edge states by QSH design. (B) Examples of QVH for on-chip light control. Demonstration of a topological edge that propagates one way from input to output in the presence of sharp bends (top row, light is transmitted from Channel 1 to Channel 2 and 4 freely) and the cavity design (bottom row) based on QVH design. Figures are taken from Ref. 38 and 36 respectively.

Compared with edge states protected by quantum Hall phases, states designed from QVH are less robust. However, the easy implementation of valley Hall systems compared with other models is an important advantage for real application.[13, 38, 39] On the other hand, compared with QSH, the QVH photonic crystal lattice can be applied to chiral routing of light easier as the edge mode is below the light cone. For example, the valley-locked chiral edge states guarantee the light is transmitted from Channel 1 to Channel 2 and 4 as shown in Figure 2.6 (top row),

with this unidirectional coupling function can be further used to demonstrate topological photonic routing and devices integration.

Furthermore, QVH can also be used for cavity design, allowing relatively high-quality factors with topological protection.[36, 40] As shown in Figure 2.6B (bottom row), a high Q factor resonator is realized by placing the inversed unit cell together, and the cavity shape can also be arranged into a triangle, honeycomb, and rhombus as for the shape of the unit cell in such design. Various resonant modes have been observed within the bandgap, and the topological waveguide also allows for the tuning of the group index, further shedding light on the selection of optical modes supported by the topological photonic cavity. These resonant modes and the possibility for selection are extremely important for optical integrated circuits.

2. Topological lasers

In recent years, topology is also revolutionizing the design strategies for lasers with surprising properties.[10, 13, 41-43] Topological lasers have been demonstrated using zero-dimensional defect states arising from the SSH model or corner states in high-order topological insulators, edge states in quantum Hall or QVH topological insulators. However, Si cannot be used for lasing directly because of the material bandgap. So, most topological lasers are fabricated from other materials, which may limit their potential applications in devices integration.

More recently, Ma at. al experimentally demonstrated a Dirac-vortex topological laser for telecom wavelength at room temperature using InAs/InGaAs grown on a Si substrate.[44] They designed and fabricated the Dirac-vortex photonic crystal lasers by harnessing an additional orbital degree of freedom in topological insulators. Especially, linearly polarized single-mode vertical laser emission from the cavities under continuous-wave optical pumping at room temperature is important for the next-generation Si-based optical integrated circuits due to the robustness of the single-mode laser.

3. Applications in quantum optics

The Si topological nanophotonics also got a lot of attention for the generation of quantum light sources. Among these researches, one of the most important aspects is to realize quantum integrated optics with quantum integrated light sources. To achieve this, spontaneous parametric down-conversion, four-wave mixing, and excitation of quantum dot materials by taking advantage of TPhCs are some popular methods used to generate quantum light sources nowadays.[45]

Topological photonics can also be used to realize quantum emitter. For the applications in integrated quantum optics, it's very useful that quantum emitters are on-chip integrated and the single photons can be transmitted efficiently in a stably emitting process. However, the scattering losses in traditional waveguides during propagation are difficult to avoid. And the loss crossing sharp corners with waveguides is even larger, which limits the possibility for

scalable integration. Just as the robustness and anti-scattering properties we introduced above, these advantages ensure topological photonic structures are a good candidate for on-chip quantum optics. Recently, the application of topological photonic structures in quantum optics can be found in both photon generation and interference. For example, Barik et al. proposed the idea of a topological quantum light source by combining two photonic crystals with different lattice constants (corresponding to the QSH model above) first the first time in 2018.[12] With the topological edge state at the interface between the two regions of the photonic crystals, the authors proposed the chiral nature of single-photon emission. This means the emitted single photons with left-hand and right-hand circular polarizations are transported to opposite directions when exciting the middle region of the photonic crystals with a laser as shown in Figure 2.7A. As the topological waveguide can be designed with arbitrary shapes and low loss single-photon propagation robustly can be realized. Their results provided a good example for combining topological photonics with quantum optics for later research in integrated quantum topological photonics.

Besides the quantum light sources, Si topological nanophotonics can also be used for on-chip quantum circuits. Recently, based on the QVH, nanophotonic topological beam splitters were demonstrated for the first on-chip valley-dependent quantum information process as shown in Figure 2.7B. Two-photon Hong-Ou-Mandel interference with a measured visibility larger than 95% is realized.[46] This result is especially useful for the realization of quantum photonic circuits and the generation of path-entangled states. Because of this, it may be possible to realize more complex quantum circuits with topological nanophotonics, which provides a novel solution for on-chip quantum information processing.[47]

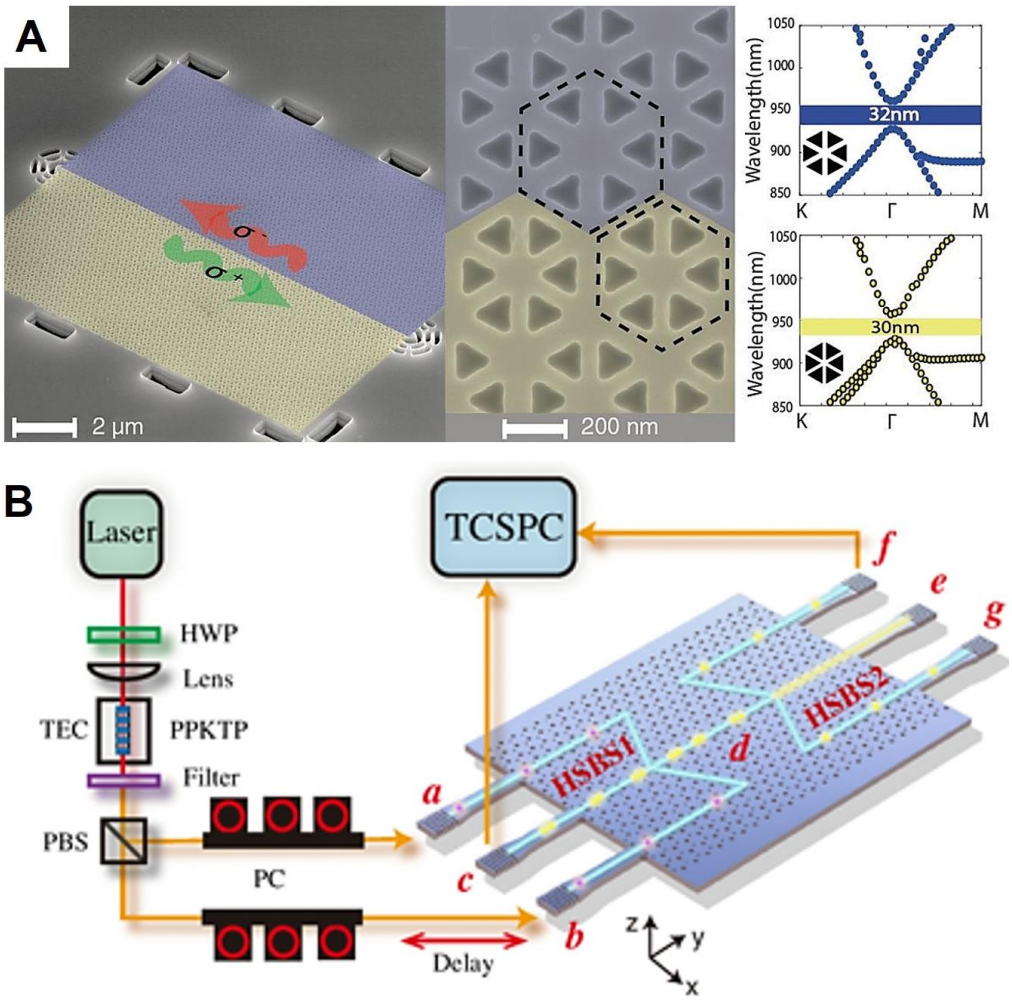

Figure 2.7 The application of TPhCs for quantum optics. (A) Chiral separation of single-photon with a TPhC designed with QSH model. Figures are taken from Ref. 12. (B) Experimental setup for the on-chip HOM interference with a TPhC designed with a QVH model. Abbreviations in the figure, TEC: thermoelectric cooler; PBS: polarization beam splitter; HWP: half-wave plate; PC: polarization controllers; TCSPC: time-correlated single-photon counting. Figures are taken from Ref. 47.

2.3 Introduction to Si metasurfaces

2.3.1 Introduction to metasurfaces and the working principle

Metasurfaces are ultrathin flat electromagnetic components that consist of well-designed subwavelength antennas. Unlike the light control that arises from the global contribution as in TPhCs, metasurfaces focus more on the local contribution from every single antenna. With these subwavelength antennas, it is possible to manipulate electromagnetic waves in a unique way.[48-50] Actually, for all the optical elements, the control of phase and amplitude plays a crucial part to realize the functionality. As metasurfaces can modify the amplitude and impart an abrupt phase shift to the incident wave within the sub-wavelength scale through the light-matter

interaction in an efficient way.[51] Various wave parameters from frequency, amplitude, phase, and polarization can be simultaneously modulated with these subwavelength antennas. With this ability, they are not only used to realize conventional optical components, but also some special functionalities that cannot be achieved by traditional optical components.

The phase modulation that is determined by the physical shape and arrangement of its nanoantennas is the most fundamental function of metasurfaces. Until now, the Huygens metasurface and the geometric phase are two typical strategies designed for phase-controlling.[52] Symmetrically-shaped nanostructures with different sizes (for example, cylindrical nanostructures with different diameters as shown in Figure 2.8) are typical structures in a Huygens' metasurface.[17, 53] As the diameter of the nanocylinder influences the reflection or transmission phase directly, the effective refractive index of the fundamental mode induced in the nanostructure can be modulated. With this working principle, the polarization-insensitive operation becomes the most important characteristic of Huygens' metasurface. However, the operating bandwidth of the Huygens' metasurface is almost limited to a single wavelength, and full-phase modulation can only be realized when the refractive index of materials is large enough.

The geometric phase is linked to the Pancharatnam–Berry phase that appears during a polarization state conversion of the wave. A metasurface that is designed with a geometric phase is typically fabricated by arranging rectangular nanostructures in different orientations as shown in the two examples in Figure 2.9.[49, 50, 54] As reflected or transmitted waves consist of two components (both co-polarized light and cross-polarized light) if a circularly-polarized light is used to interact with such kind of geometric metasurfaces. The phase modulation of the cross-polarized light is twice the rotation angle of the rectangular antenna, this makes it very intuitive to recognize the phase variation for the rotation of antennas. Different from Huygens' metasurface, the geometric phase metasurface works only for circularly-polarized light. However, the geometric phase is not affected by the wavelength, and the operating bandwidth of geometric-phase metasurfaces is always larger compared with Huygens' metasurfaces.

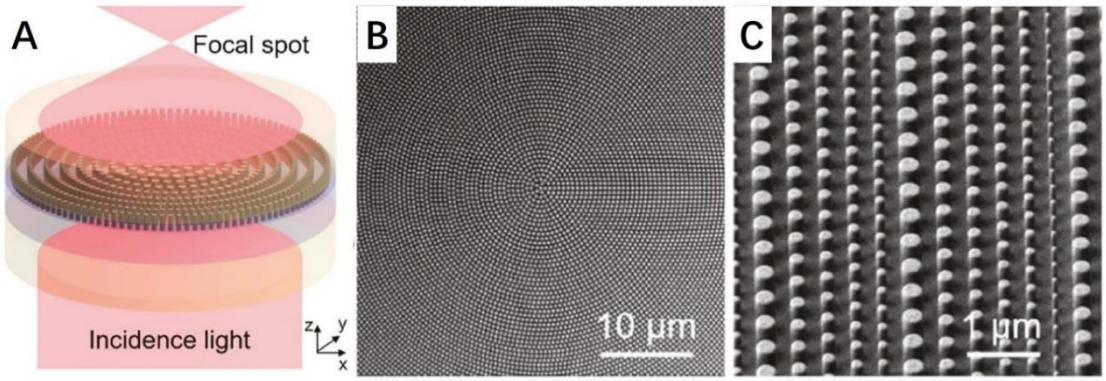

Figure 2.8 Example of a Huygens metalens. (A) Schematic of the metalens. Cylindrical nanostructures with different diameters are used to realize the phase distribution of a lens. (B) SEM image of the metalens at the center. (C) Enlarge SEM of the metalens at the edge. Figures are taken from Ref. 53.

Depending on the function of metasurfaces, we can always find a suitable way to achieve the phase distribution linked with our functionalities. For example, by specially designed antennas shape or distribution, this phase distribution can be realized. Usually, the design of a metasurface follows a flow chart like the one shown below:

(1) A target phase profile is determined based on the functionality of the metasurface. This phase profile can be achieved either by an analytical solution in some relatively simple designs like a lens or a grating or by a numerical simulation in the case of a more complex design like an optical hologram.

(2) The exact geometry of a group of nanostructures is determined by the wavelength range that the metasurface is expected to work in. During this step, a commercial software is frequently used to perform a parameter sweep over different geometries (for example, the diameter of the nanocylinder in Huygens' metasurface) using numerical simulations.

(3) Implementation of the target phase control with the help of different nanostructure properties (for example, by different orientation angles with geometric-phase strategy).

2.3.2 Typical applications of Si metasurfaces

Benefiting from the unprecedented capability of light manipulation, metasurfaces with unusual functionalities have been developed. In this part, we will shortly focus on three of the applications of metasurface: metalenses, holograms, and structural color. Although these applications can also be realized with metasurfaces constructed with other materials, like the plasmonic materials. But plasmonic metasurfaces have the drawback of metallic loss, which limits their optical efficiency. Their dielectric counterparts have proven to be effectively contributed by the low optical losses and compatibility with the state-of-the-art semiconductor fabrication technologies. Among all-dielectric metasurfaces studied so far, Si nanostructures take great advantage of their high refractive index ($n > 3.5$ at visible and infrared wavelengths) for extending optical phase shifts and their compatibility with conventional processes for Si-based electro-optic devices.[55] In addition, due to the efficient fabrication technology for different thicknesses in the lab, amorphous Si metasurfaces are widely adopted for various optical applications of beam deflectors, spectrometers, optical filters, and flat lenses within the low-loss range of extinction coefficient at infrared wavelengths.

1. Metalenses

Conventional optics either based on refractive lenses or Fresnel lenses, are always heavy and bulky, which both show drawbacks in lots of application cases. In addition, the fabrication of traditional lenses to reduce aberration is always time-consuming and requires complicated processes. As for the Fresnel lenses, although they are thin and compact, their efficiency decreases rapidly if the numerical aperture (NA) continuously increases as most of the transmitted light is reflected at the surfaces with saw-tooth structures.[17] Fortunately, metalenses are even thinner and more compact than Fresnel lenses and they are not affected by the

shadowing effect as all the nanostructures in metalenses have the same height. Therefore, both high focusing efficiency and wanted NA (both large and low) can be realized in metalenses simultaneously. For instance, a highly efficient silicon metalens at low NA (based on the Pancharatnam–Berry phase) for optical trapping of particles is demonstrated by applying the optical force produced from metalens as shown in Figure 2.9A.[56]

Except for the high efficiency at wanted NA, directly reducing chromatic aberrations is possible during the design of metalenses.[17, 57, 58] For example, a spherical aberration can be perfectly removed in metalenses because their spatial phase gradients can be precisely defined by nanostructure arrays. By tailoring the dispersion of individual nanostructures, chromatic aberration can be corrected easily in a single layer of metalenses. However, in conventional refractive lenses, the typical correction process uses a series of bulky and heavy refractive lenses. On the other hand, as for the ultrathin structure, dynamically control focusing properties of metalenses can be realized with microelectromechanical systems technologies by applying external voltage stimulation. This provides solutions for the integration of metalenses into integrated electrical devices, with more promising applications that can be realized soon.

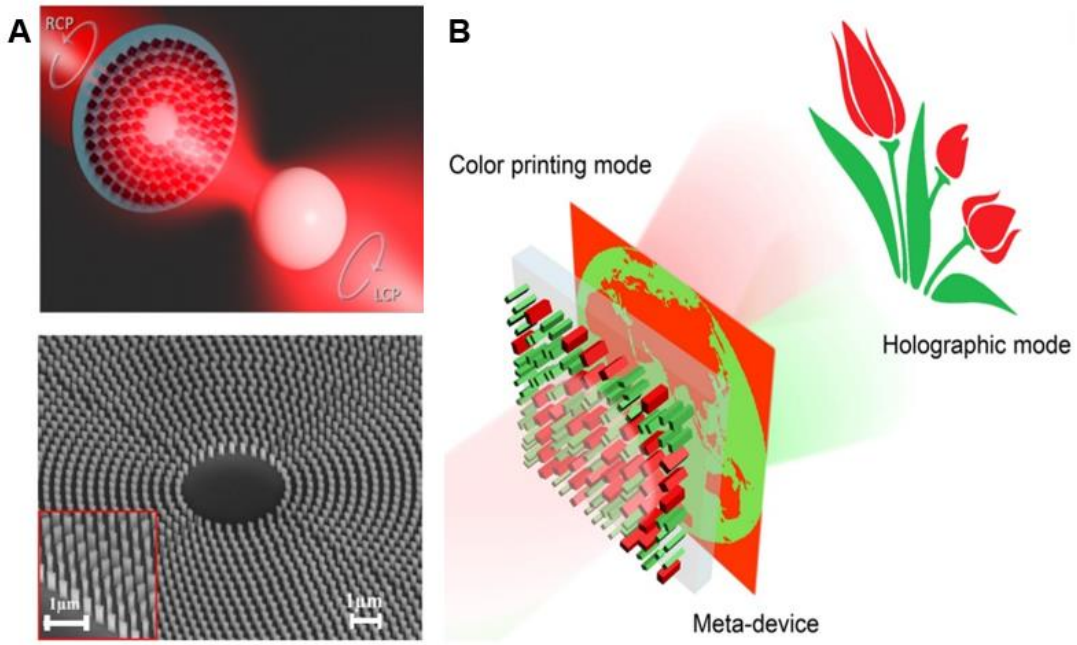

Figure 2.9 Two applications of metasurfaces were published by our group members. (A) The conceptual image illustrates the trapping of a polystyrene particle with the help of an all-dielectric metalens and the SEM image of the fabricated metalens. (B) Schematic illustration of the all-dielectric metasurface with both structural color and holography by modulating spatial and spectral responses simultaneously. The metasurface is composed of a-Si nanofins with optimized spectral responses to obtain the desired structural color. When illuminated with different wavelengths, it can reconstruct different encoded holographic images in the far-field as a multiplexing hologram. Figures are taken from Ref. 57 and 63 respectively.

2. Metaholograms

Holography is an optical technique that consists of the reconstruction of 3D complex optical waves emitted or reflected from a certain object. Traditionally, holograms are made by recording the interference patterns of an object beam with a reference beam on a photographic plate. With the recorded plate, the object beam can be perfectly reconstructed by illuminating it with a reconstruction beam. Unlike traditional holograms, computer-generated holography is a spatially distributed complex amplitude image from a mathematical calculation technique. As the complex amplitude can be realized with the special arrangement of antennas, the resulted metaholograms are much smaller than the visible wavelength, so diffraction does not occur.[59, 60] It can also be used to overcome some limitations of conventional holograms, for example, a large viewing angle is possible with metaholograms. Moreover, the arbitrary control of complex amplitude by carefully designing the nanostructures also means 3D complex optical waves can be perfectly reconstructed with a metahologram.[61] In addition, metasurfaces have also been used to demonstrate color holograms that cannot be observed traditionally as shown in Figure 2.9 B, this means three primary colors (red, green, and blue) can be integrated into one metasurface.[62]

3. Structural color

Nowadays, pigments and dyes are the most frequently used color carriers in our daily life. Such kinds of colors are formed by absorbing a certain range of visible wavelengths. This means the colors produced by them are typically dim and have a small gamut range. In addition, as the sizes of pigments are on the order of 25 μm, this always results in a poor resolution below 1000 dpi. To solve the disadvantages with pigments, the colors from metasurfaces get a lot of attention recently because they can produce vivid colors covering the entire visible range.[63] Despite the already existing successes in this application, structural color also gets practical applications like digital displays, molecules sensing, optical security, and information storage.

Owing to the nanometer scale confinement of the electromagnetic field with subwavelength antennas, plasmonic nanostructures have shown several advantages in printing high resolution, robust, and reliable colors.[64, 65] This nanometer-scale confinement ability means the size of the color pixel can also be reduced to a subwavelength range beyond the diffraction limit of light. Recently, metal masked Mie resonators are developed to avoid unwanted color shifts that come from interactions with neighboring unit structures. Instead of metals, dielectric materials can also be used to realize high-quality structural color with Si, a-Si, or TiO_2.[63, 66] These structural colors from metasurface have been applied for lots of applications like encryption, steganography, and coloration of coins. In addition, by using the resonant interactions between metasurface and molecules, spectroscopy with the unnecessary relative strong background can be efficiently suppressed, which improves the molecular detection sensitivity.

2.3.3 Multifunction metasurfaces to meet more requirements

Despite the variety of functionalities that have been achieved based on the unique advantages of the flat and ultrathin nature of metasurfaces, further development of them entails not only better device performances, but also smart methodologies to enhance the device adaptability for practical applications and future commercialization.[65, 67-70] Recent researches with reusable and dynamic abilities stand out among this field. For example, Li et. al show a reusable metasurface template by the combination of both the geometric and propagation phase controls, where the propagation phase information is erasable and rewritable as shown in Figure 2.10A.[68] The metasurface template can then be used to construct metalenses, computer-generated holograms, and vortex beams, largely reducing the fabrication complexities and extending the function only with one metasurface.

On the other hand, as one of the crucial problems, fragile nanostructures are typically highly sensitive to dust and other contaminants, which ultimately limits their wider application. Until now, there is no solution to efficiently clean or protect-from dust contamination on a metasurface that consists of specifically designed antennas. Hence, finding a feasible strategy to clean the metasurface without affecting its optical performance or damaging the nanostructures is crucial for various practical applications. This means accessible strategies to enhance the device's adaptability and effectiveness in complex application conditions, physical stability, and smarter functionality are important properties that need to be considered when one designs the device.[51, 71-73]

Last but not least, the liquid-background metasurface also got a lot of interest in rent years. This kind of metasurface is designed by immersing in water, liquid crystal, alcohol, or other solutions to achieve the corresponding refractive index tuning and achieve the purpose of optic wave controlling.[74] Between them, cheap and non-toxic water is the most popular used one and can be mixed with other materials to achieve a large number of liquids with different refractive indexes. By adjusting the refractive index of the solution with different concentrations of the solution surrounding the metasurface, the optical response like large reflection angle and the beam diffraction direction can be adjusted switchable as shown in Figure 2.10B.[75] This kind of liquid-background metasurface is useful for achieving tunable performance, but on the other hand, should also consider the perfect matching between the antennas and solution.

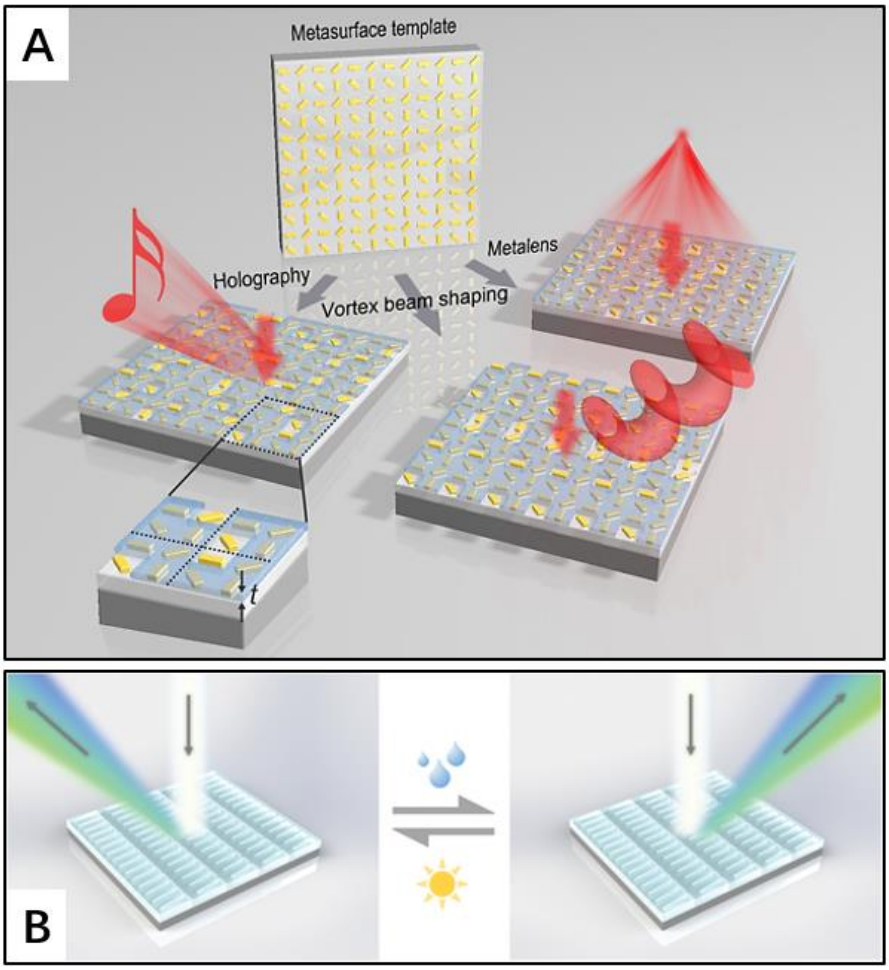

Figure 2.10 Example of metasurfaces with more functionality. (A) Schematic of the reusable metasurface template. Gold nanorods are arranged in a specific geometric phase profile on the metasurface, which works as a template for the incorporation of different propagation phase distributions to achieve diverse optical functions, including metalens, hologram, and vortex beam generation.[68] (B) Actively switchable beam-steering functionality by selective liquid-wetting on metasurfaces.[75] The reflection angle of the beam can be switched to a different angle with or without liquid on the metasurface. Figures are taken from Ref. 69 and 76 respectively.

2.4 Fabrication of Si-TPhCs and Si-metasurfaces

Regarding the nanoscale size of Si nanophotonics, the top-down method based on lithography and plasma etching is the most popular way to fabricate these devices. This section introduces some common procedures, especially the EBL and plasma dry etching for the fabrication of Si nanophotonics. While more details for each specific design will also be introduced in each chapter later in the corresponding experimental part.

2.4.1 EBL introduction

EBL has been the main technique for fabricating nanoscale patterns in research work. As

the resolution in optical lithography is limited by wavelength and NA. Although various techniques have been made to increase the NA, the resolution in optical lithography is still limited as we cannot go below a particular wavelength. For electrons, the wavelength is much shorter as given by the de Broglie equation:

$$\lambda = \frac{h}{p} \tag{2.10}$$

where h is Planck's constant and p is the momentum of the electron. When the electrons are accelerated to a certain velocity $\mathrm{v} = \sqrt{\frac{2eU}{m_0}}$ in an electric potential U, they gain some momentum p. Here, m_0 is the mass of the electron, and e is the elementary charge. The electron wavelength is then given by

$$\lambda = \frac{h}{p} = \frac{h}{m_0 v} = \frac{h}{\sqrt{2m_0 eU}} \tag{2.11}$$

This means that with a higher accelerating voltage of the system is possible to get a higher resolution. In a normal commercial electron microscope, U is usually several thousand volts, which typically provides the wavelength of the electrons at 10^{-12} m when the relativistic effects are taken into consideration. This means EBL can provide a much higher resolution compared with optical lithography for the fabrication of Si nanophotonics, and a variety of other substrates.

A typical EBL process flowchart is shown in Figure 2.11, with a brief description of individual process steps are given below.[76]

(1) Patterning file preparation. Before the EBL process, we should prepare the writing files we need. And the system will do lithography based on our files. In these files, we normally include some masks for later alignment. Besides the masks, the structure we need to write, like metasurfaces or TPhCs should also be included. To get good structures, the proper dose should be decided in these files based on different designs. These files can be prepared by MATLAB if the structures are too complex and many. On the other hand, we can also prepare some simple structures using the software itself.

(2) Substrate Preparation. To prepare the substrate for the photoresist coating at the next step, the sample should be cleaned sufficiently by placing the sample in a mixture of water, acetone, and isopropanol with an ultrasonic bath for at least 10 minutes. After the sonication, the sample is rinsed with acetone, isopropanol, and water, and then dried with nitrogen gas. Sometimes we also need to deposit specific materials on the substrate based on the design, this deposition is performed on the substrate by the same cleaning process.

(3) Resist Preparation. To coat a uniform resist layer on the sample, we should select the suitable ramping, spin speed, and timing based on the spin speed curve from the datasheet provided by the company. The substrate with the resist layer after spinning coating is then baked at the suggested temperature on a hot plate for a short time. Note here, the baking

temperature and time are also different for different resist, this information can also be found in the suggested condition from the company or possible changes should be selected based on the previous testing.

(4) EBL system alignment and patterning. When loading the sample, we should select the suitable accelerating voltage and the appropriate working distance and aperture size. In addition, a stage adjustment is necessary by defining patterning coordinate reference to the sample to fabricate structures on the area we want. Then the most important step is the focus, astigmatism, and aperture alignment. As the electromagnetic lenses used in an SEM are not always perfectly symmetrical. On the other hand, as the dose applied on the resist is extremely important and the real value at every experiment may have some differences, we should measure the current for every patterning and correct it to the wanted value in the writing file by slightly adjusting the exposing time. The current is measured by moving the stage to the location with a Faraday cup exactly below the e-beam and measure automatically. Then we can select the design in the position list and expose what we need.

(5) Structure developing. Based on the selected resist, the developer can be used to remove the patterned structures (positive resist) or unpatented structures (negative resist), and the stopper is used to stop the reaction between them. Both the time in developing and stopping solutions are important to get a good sample as we are working with structures at the nanoscale. After that, the sample is rinsed with a stopper and dried with nitrogen gas. In addition, post-baking at a suitable temperature and time sometimes is necessary to increase the stability of the resist for the following applications.

(6) Structure checking or other flowing steps. After all the processing above, we can check the structure by SEM or continue other flowing steps like either depositing another mask for etching or using the resist as an etching mask directly.

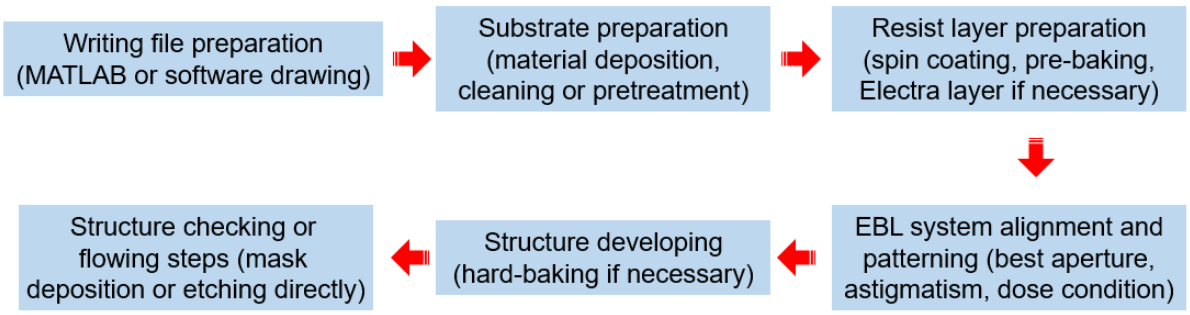

Figure 2.11 A typical EBL process. The process includes 6 major steps as shown here. (1) Patterning file preparation. (2) Substrate Preparation. (3) Resist Preparation. (4) EBL system alignment and patterning. (5) Structure developing. (6) Structure checking or other flowing steps.

2.4.2 Plasma dry etching

Plasma dry etching is an essential step for semiconductor fabrication. It has already been applied for the fabrication of integrated circuits and microelectromechanical systems in the

industry during the past few decades. Furthermore, significant improvements in nanostructures fabrication can be realized by controlling the plasma density and the energy imparted to the ions independently or at the same time. In this thesis, we apply inductively coupled plasma reactive ion etching (ICP-RIE) to fabricate Si nanophotonics with Oxford PlasmaLab System 100 ICP.

The main mechanisms of removing material during the ICP-RIE process include both chemical and physical interactions between the material and plasma.[77] The chemical interaction is based on the reaction of some free radicals with the etched material at the outside surface, while the physical interaction is due to the high energy ion and removing some atoms of the etched material directly. When applying an ICP-RIE process during fabrication, one basic parameter one needs to consider is the selectivity of etching, which is defined as the ratio of the etching rate of different materials in the same process and condition. Normally, metal masks, i.e., Cr, Ni, and Al, show great promise as for the high selectivity and anisotropy of etched profiles. On the other hand, some non-metallic masks, like photoresist or SiO_2 can also be useful in some shallow etching cases. Besides the selectivity of etching, the etching directivity determined by the well-known anisotropy factor should also be considered to get high-quality structures. This anisotropy factor is determined by the etching rate in the perpendicular direction and the etching rate in the direction tangent to the etched surface together. If the etching rates in both directions are comparable, this is the case of isotropic etching. For example, dry plasma etching is a typical isotropic etching process as it is. But in the plasma etching process known as the (pseudo) Bosch process, a polymer on the walls of the pattern protects the chemical removal of material and results in an anisotropic etching. Normally, a Bosch etching process consists of repeated sequences of etching and passivation (protection) steps. And an anisotropic etching with the Bosch process can provide almost vertical etching as the tangential etching rate is almost zero due to the protection process. The possibility to obtain almost vertical structures by the Bosch process makes it indispensable for nanoscale etching for Si nanophotonics.

In this thesis, the Si pseudo-Bosch etch process is based on the SF_6/C_4F_8 gases as illustrated in Figure 2.12.[77] Here, SF_6 is used to provide fluorine ions and radicals to etch Si after injected and ionized in the chamber, and SiF_4 is the etch product in this process. C_4F_8 is applied to create a polymer chain of CF_2 for protection on the surface of the structure after ionizing. But it's important to note that although the polymer create by CF_2 protects the Si from chemical etching, the milling generated by the acceleration of SF_x and F_y ions in the presence of a direct current bias electric field is possible to remove the protective polymer layer on the horizontal direction faster than the polymer redeposition rate. This means a sidewall coated with polymer is free to etch in the horizontal direction. The Sisyphean task of removing the horizontal polymer deposition before etching Si causes the slow etch rate, while the continuous passivation and etching prevent the presence of scalloping shape in the normal Bosch etch process. Overall, the relatively slower etch rate and smoother sidewalls make this etch process ideal for nanoscale structures fabrication. The condition for Si etching in our thesis is: gases flow rate, SF_6 = 18 sccm C_4F_8 = 45 sccm; RF-power 41 W; ICP-power 900 W; pressure and

temperature of the chamber is 10 mTorr and 12 ℃ respectively. The etching condition above provides an etching rate of Si around 350 nm/min.

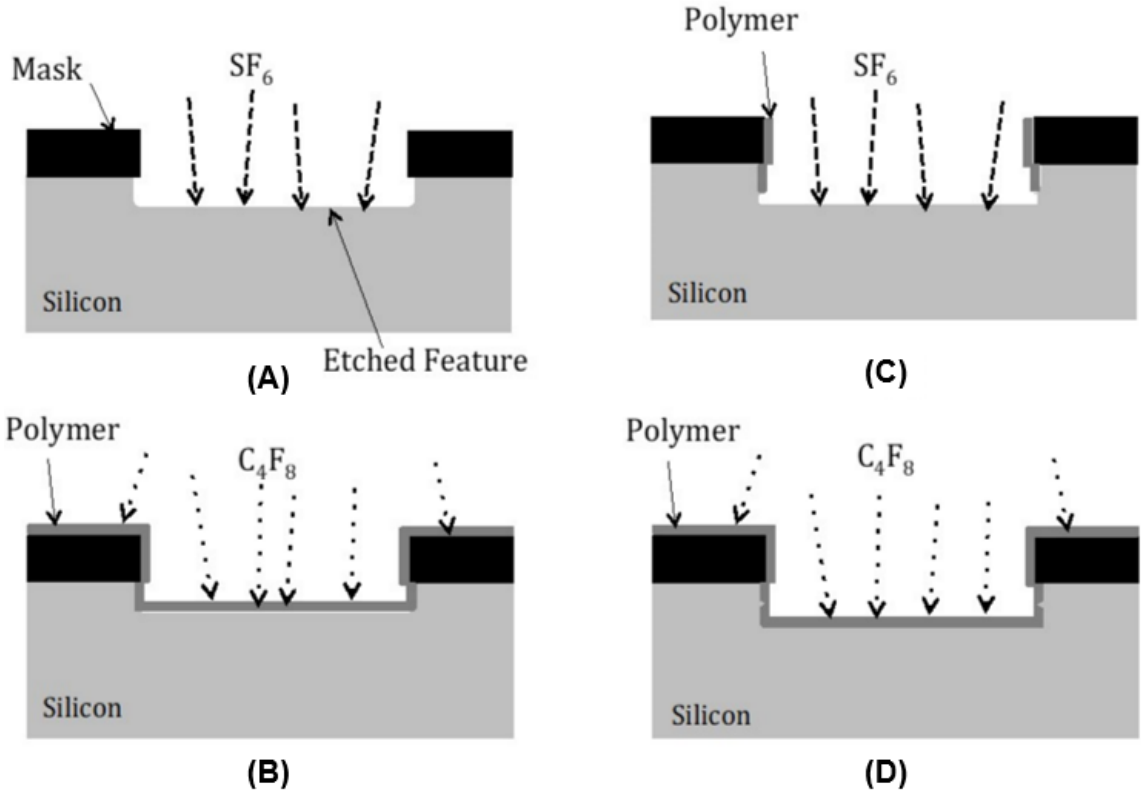

Figure 2.12 An illustration of the pseudo-Bosch process during Si dry-etching. (A) Si etching is realized by the fluorine-based reactive species from SF_6. (B) Then the system turns off the SF_6 gas and turns on the C_4F_8 gas automatically, and a protection polymer is formed on the entire surface. (C) Next, the C_4F_8 gas is turned off, and the etching gas SF_6 is turned on again for the etching process. (D) Then, the SF_6 is turned off and the protection gas C_4F_8 is turned on again. The repeating of etching and protection is a typical pseudo-Bosch process. Figures are taken from Ref. 77.

2.5 Conclusion

Si-based nanophotonics host bright promising opportunities for optical circuits with faster data transmission and processing compared to traditional electronics, which is thought to be realized by replacing the currently widely used electronic connections with photonic integrated circuits. With the rapid development of nanofabrication technology based on EBL and plasma dry etching, shrinking the device size down to the nanoscale is extremely useful for devices integration similar to what we use in integrated electronic circuits that highly increase the convenience of our daily life nowadays.

Based on the ideas that were first developed in solid-state physics, TPhCs provide topological protection to light transport. While in some TPhCs like QSH and QVH, the new degree of freedom for robust light transmission can be used to design topologically protected

components like resonators and beam splitters. Regardless of these recent processes in TPhCs, continuous efforts are still focused in this field to find new topological design strategies to access protected robust states, especially in optical wavelengths for highly promising applications. In addition, although some works have already shown some important fundament components that work as a single part, the combined performance for on-chip photonic integrated circuits is still unclear. This means focusing more on the integrated circuits to realize more functionalities with TPhCs will make the goal of all-optical computing one step closer.

As for the further development of metasurfaces, although various parameters from amplitude, phase, and polarization can be simultaneously modulated, or lots of advantages compared with traditional components have been shown with them, a critical direction would be to seek possible strategies for smart metasurfaces with improved optical performance, versatile functionalities and physical stability close to real situation. These smart functionalities are also important to other nanophotonic platforms if they can be realized.

3. Si TPhCs with 0D light localization protected by weak topology

Optical lower-dimensional localization with strong light-trapping is extremely useful for a variety of applications such as nonlinear enhancement, photonic devices miniaturization, photonic or quantum chip integration, and so on.[78-81] Achieving localization that is robust against structural changes would boost the progress in the development of related applications. Recently, it has been shown that TPhCs may provide robust topological protection to 0D localized modes as proved by recent researches.[6, 82-84] They also verified the promising routes for topological light localizations, e.g., showing several advantages in topological lasing.[10, 42] In this chapter, we focus on the design and verification of 0D localization at optical wavelengths, with the concept of weak topology.

3.1 Recent progress of topologically protected lower-dimensional localization

Optical lower-dimensional localization, especially 0D localized modes with strong light-trapping is extremely useful for a variety of applications. In recent years, state-of-the-art nanophotonics based on these strong light-trapping effects has gotten quite a lot of attention in these fields due to the wondering for high-speed data transmission or all-optical computing by the miniaturization of optical systems down to the nanoscale. Currently, one of the most widely followed strategies to realize 0D optical localization is based on the well-known photonic crystal defect designs, which are conducted by removing part of the structure in the PhC and in this way can achieve light localization around the defected part.[85, 86] However, in most cases, localization achieved with this method is fragile to structural changes, which could lead to significant detuning of either resonance frequency or mode volume. The changing of localization properties makes the device's design and fabrication extremely crucial.

Hence, achievable localization that is robust against structural changes would boost the progress in the development of related applications. Just as mentioned in the introduction to TPhCs in chapter two, they are robust against fabrication disorders when they are applied to light transmission because of the protection by topology, which is a global feature. Similarly, TPhCs may also provide robust topological protection to 0D localized mode as it was proven by recent research and already verified the promising routes for topological light localizations, e.g., showing some advantages in topological lasing.[41, 87]

To achieve topologically protected 0D localization, two concepts with higher-order topological insulators (HOTIs) and the Dirac vortex method have been recently applied. It is known that the bulk-edge correspondence principle has long been used to guide the design and analysis of the edge states.[7] According to this rule: A d dimensional topological insulator with

the same number of insulating bulk states could only support *d*-1 dimensional conducting edge states. HOTIs are beyond this traditional bulk-boundary correspondence as more topologically protected states like *d*-2 dimensional states can be realized. For example, a second-order 2D HOTI not only supports 1D edge states but also 0D corner states.[82, 88, 89] However, performing the design in this way means HOTIs need multiple domains of different unit cell designs (like the presence of edge states needs both trivial and nontrivial unit cells according to the bulk-edge correspondence) to achieve these 0D localized modes at the boundary between the domains as shown below in Figure 3.1. Here, the trivial unit cell is the one shaded with red and the nontrivial unit cell is the other one shaded with sky-blue, which is determined by the 2D Zak phase as we will introduce later.

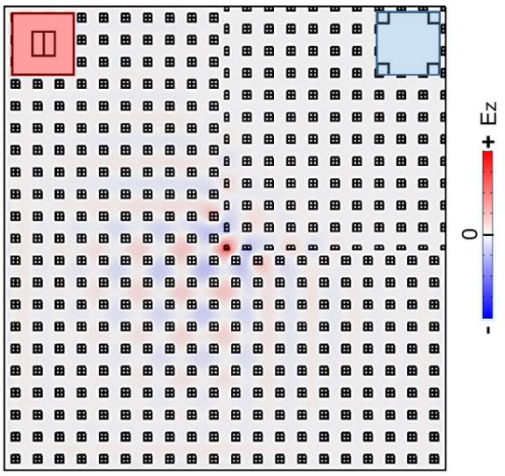

Figure 3.1 A HOTI design constructed by trivial and nontrivial unit cells. A 0D localized state (also known as the corner state) inside the bandgap is observed at the corner of the trivial/nontrivial interface. The two unit cells in this design will be analyzed in the latter part of this chapter.

Another method is based on the Dirac vortex cavity, which is a photonic realization of the zero-mode solutions to the Dirac equations.[83] In this design, the starting structure with a four-by-four double Dirac cone formed by the hexagon supercell consisting of three honeycomb primitive cells is considered (Figure 3.2A). Then a generalized Kekulé modulation by shifting the sublattice (the three grey air holes) from their original positions with the same amplitude m_0 and correlated phase ϕ_0 in the supercell generates the 2π vortex gap of the double Dirac cones (Figure 3.2B-C). This gap opens for all 2π values of ϕ_0 with non-zero m_0, while closes when $m_0 = 0$. As the vortex band gap has an angular periodicity of π/3 due to the lattice symmetry, the minimum gap size is found at $\phi_0 = 0$. A library of supercells with a vortex band gap whose phase continuously varies by 2π is obtained based on this tuning, and the cavity formation is then realized by arranging these supercells angularly around a cavity center, as illustrated in Figure 3.2D. Such Dirac-vortex cavities are proved to possess a larger free spectral range than other optical cavities with a scalable modal volume and can act as an ideal candidate for realizing high-power single-mode surface-emitting lasers.

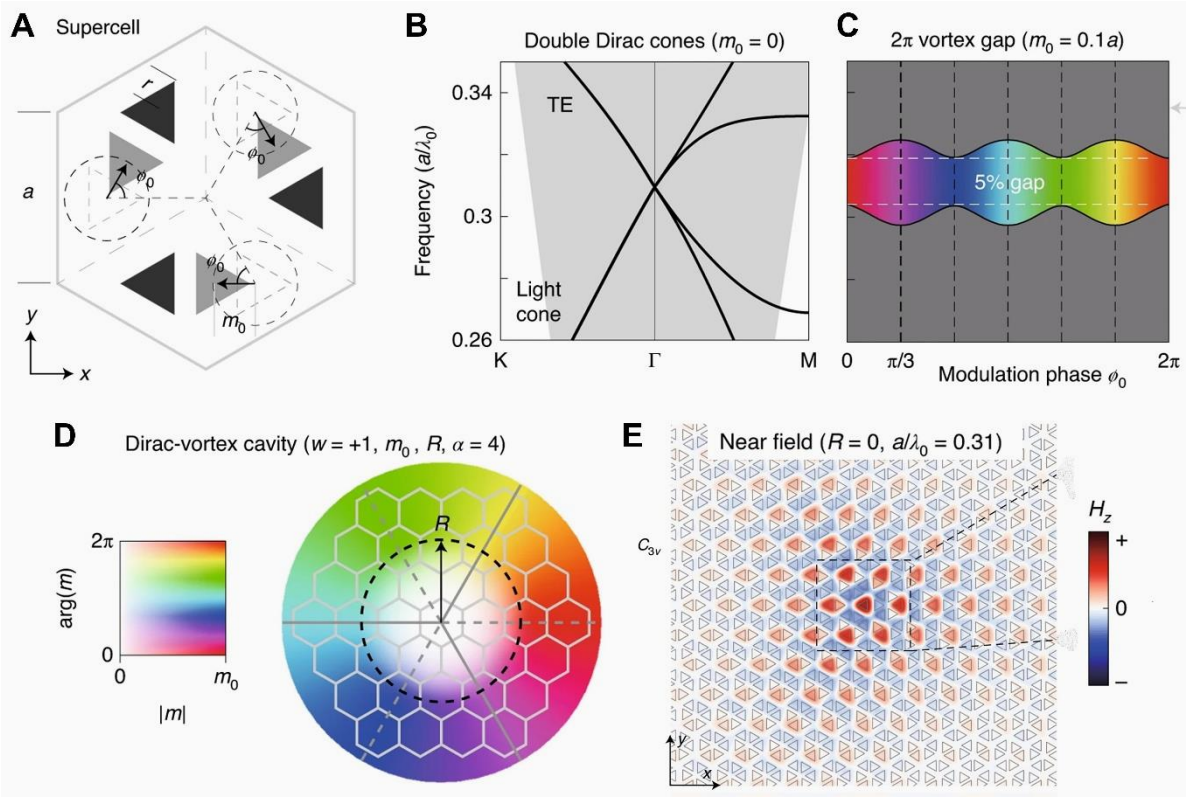

Figure 3.2 Design of the photonic-crystal Dirac-vortex cavity. (A) Illustration of the supercell for realizing the generalized Kekulé modulation. (B) A Double Dirac cone above the light cone is found in the unperturbed initial supercell. (C) Both ϕ_0 and m_0 can be tuned to open the bandgap with phase modulation. (D) Illustration of the Dirac-vortex cavity by arranging different perturbed unit cells together. (E) Near-field distribution of the topological model. Figures are taken from Ref. 83.

3.2 Introduction to the weak topology

Besides the HOTIs and Dirac vortex method that are introduced above, another promising strategy to achieve topologically protected 0D localized modes lies in the design with weak topology.[6, 90-92] Unlike well-known strong topological insulators with the topologically protected states that are decided by a scalar topological invariant, the weak topological invariants are decided by vectors. This means weak topological insulators may also be used to achieve a lower-dimensional localized state by arranging these vectors that form the weak topological invariant. For example, with topologically nontrivial unit cell design in addition to, e.g., an intentionally introduced dislocation, at the dislocation centers, strongly localized modes can be generated and measured as illustrated in Figure 3.2. The additional requirement of the vector topological invariant instead of scale one gives the name 'weak' as the presence of these states needs more requirements.

This design idea has been used to achieve 0D localized modes at micrometer wavelengths with magnetic-optical materials under an external magnetic field.[6] In their work, the topology

in wavevector space is formed by both the nonzero Chern number from the magnetic-optical material under an external magnetic field and the Zak phase with different unit cell designs. By cooperating with a dislocation in real space, the Dirac mass becomes position-depend, since the two physical edges that are separated by the dislocation experience different numbers of lattice translations with such a design. This leads to a sign-change in the Dirac mass, forming a mass domain wall at the dislocation, which means a bound state localized at the dislocation center can be found. Still, the design and the experimental characterization of a weak topology protected localized mode has yet to be demonstrated at optical frequencies with accessible strategies, which could renovate the development of related optical devices or applications.

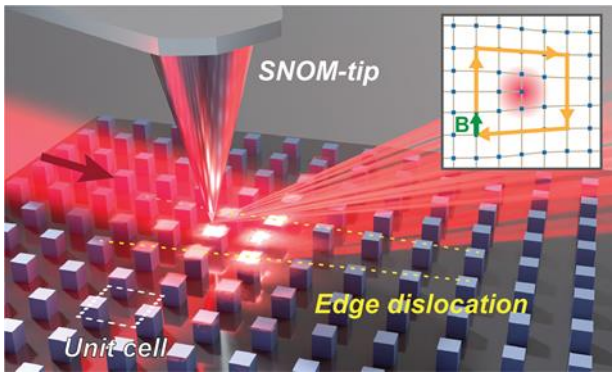

Figure 3.2 Schematic illustration of the s-SNOM measurement on the localized topological state. With the edge dislocation formed by nontrivial unit cells, a strong field localization around the dislocation center is visualized by s-SNOM measuring directly the optical near-fields. Inset: Schematic of the dislocation point with corresponding Burgers vector **B**

3.3 Defect design and localization from weak topology

Based on the introduction of the weak topology above, we get an impression that the weak topology may give rise to a topologically protected localization. To achieve this, we need a unit cell design that is nontrivial for its band structure at the first step. This nontrivial unit cell is the same classification of strong topological insulators, but should possess an anisotropic characteristic; then the spatial arrangement of the nontrivial unit cell with a proper defect design in real space may give rise to the 0D localization we want. In this part, we show our results from the unit cell design, followed by the verification of the anisotropic edge state between the interface of trivial and nontrivial unit cells, to the final achievement of localization protected by weak topology in the TPhC with a dislocation based on nontrivial unit cell.

3.3.1 Band structure topology from different ways of unit cell selection

Just as in the SSH model we introduced in Chapter 2, different ways of unit cell selection can result in different inter/intra coupling, which gives rise to both trivial and nontrivial unit cells although the band structure is the same. In our design, we consider a square-lattice with a unit cell (constant period P = 1334 nm) that consists of two rectangular Si pillars (the size

dimension is shown in the caption of Figure 3.3) with a refractive index of 3.49 placed on a chromium (Cr) film. The refractive index here corresponds to the value of a-Si determined from our ellipsometry measurement by fitting the data with the well-known Drude model. Here, the metal at the bottom acts as a perfect electric conductor and reduces the requirements of fabricating dielectric nanostructures with a high aspect ratio.[82] This is because the perfect electric conductor requires electric fields that are perpendicular to the boundary and thus doubles the effective height of the Si antennas.

The TPhC that is designed here can be regarded as the photonic realization of the 2D SSH model. Similar to the 1D model, the intracell and internal distances between two neighboring pillars are corresponding to the hopping amplitudes. But should consider the interaction or hop in both x and y directions in this 2D model. Then the topologically trivial (d = 0 nm) and nontrivial (d = 870 nm) unit cells here also possess the same band structure with a full bandgap (94.4 THz — 101.6 THz), as they can be used to construct the same infinite PhC (the band structure is shown in Figure 3.3B). However, their topology is distinguished by a 2D Zak phase if we consider the first bulk band. And the 2D Zak phase case here is a generalization of the 1D Zak phase to both directions (k_x and k_y):[11, 82, 84]

$$\theta_i = \int dk_x dk_y \mathrm{Tr}[\boldsymbol{A}_i],\ i = \Gamma X \text{ or } \Gamma Y; \tag{3.1}$$

where $\boldsymbol{A}_i = i\langle u_{\_k}| \partial_{\mathrm{k_i}} |u_{\_k}\rangle$ is the Berry connection, $|u_{\_k}\rangle$ is the periodic Bloch function. The parity-time symmetry of the unit cell requires the Zak phase to be only 0 or π as proved by previous research.[28, 93] Similarly, the electric field profiles' parity at the high symmetry points can indicate the Zak phase, by examining $\widehat{M}_{\_x,y}|u_{\_k}\rangle = m|u_{\_k}\rangle$, in which $\widehat{M}_{\_x,y}$ is the mirror operator, and m is the mirror eigenvalue at mirror-symmetric Bloch moments. Since the fundamental bulk band at the Γ point is mirror-symmetric in the static limit, the Zak phase for $\theta_{\Gamma X}$ (equal to θ_{YM}) is π only when m = -1 at the X point (mirror antisymmetric), and the same for $\theta_{\Gamma Y}$ (equal to θ_{XM}).[82] Hence, the differences in the electric field distribution at the X and Y points (inset image of Figure 3.3B) only provide nonzero $\theta_{\Gamma X}$. The result is the same as our numerical calculations as verified by the Wilson loop approach as shown in Appendix Part B. To better see the topological phase transition, the full bandgap size together with the Zak phase transition through changing d is further illustrated in Figures 3.3C, D, E. According to this, d = 435 nm is the topological transition point, where the band gap closes and reopens. The closing and reopening of the band structure can also be used to easily understand the presence of topology in the band structure, as this gives rise to a twist although the starting and ending unit cells show the same band structure. Note that the parity inversion only occurs at the X point and is not observed at the Y point, which is especially useful for the weak topology design as for the difference in these two directions.

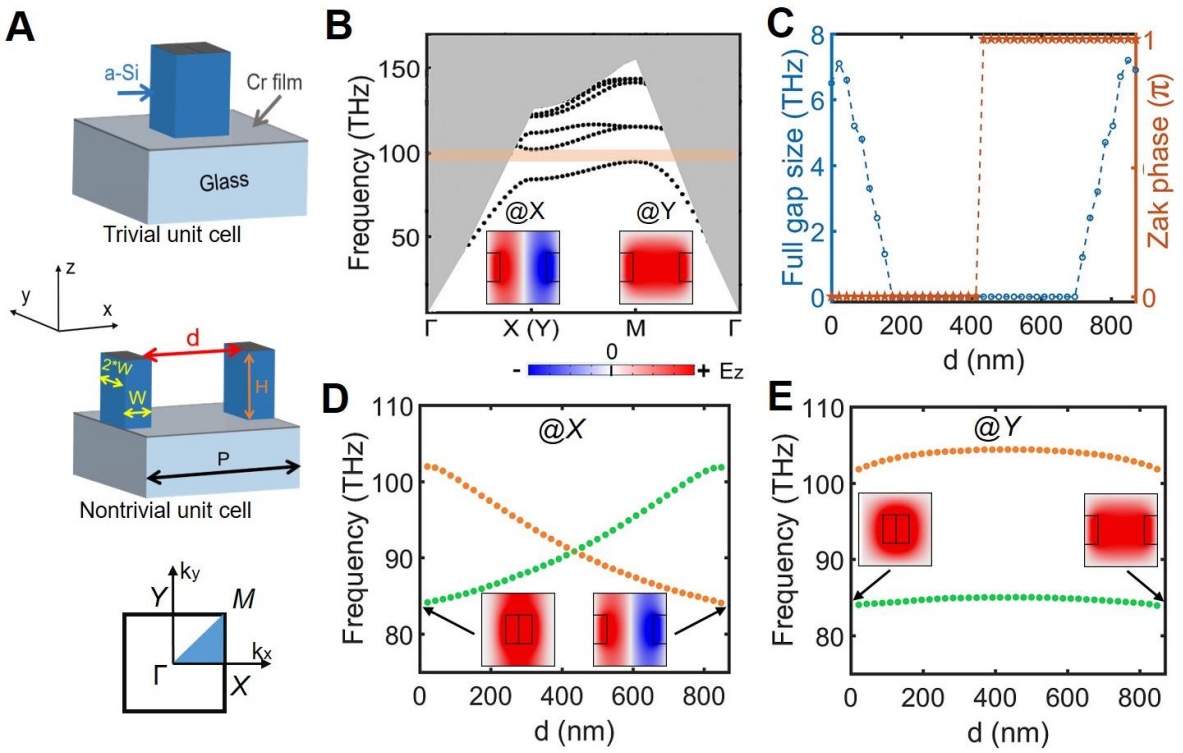

Figure 3.3 Band structure analysis of the TPhC. (A) Schematic illustration of the topologically trivial unit cell (d = 0 nm) and nontrivial unit cell (d = 870 nm) made of a-Si nanopillars on a Cr film. The topology is originated from a different way of unit cell selection. (B) Corresponding band structure of a TPhC with P = 1334 nm, W = 232 nm and H = 673 nm for both trivial/nontrivial unit cells. A full bandgap from 94.4 THz — 101.6 THz is observed as shown in the orange region. The light cone in the band structure is shaded in gray. (C) Evolution of the full bandgap size and Zak phase of the lower band for different d between the nanopillars. (D and E) Evolution of the two lowest bulk states at the X or Y point with different d. Inset images in (B, D, and E) show the z component of electric fields (E_z) for the first band at different k points, which can be used to determine the Zak phase intuitively.

3.3.2 Edge states in the TPhCs based on the SSH model

With the above trivial and nontrivial unit cells, we then check the bulk-edge correspondence, which is used to determine the presence of edge states at an abrupt interface of them like all the other topological insulators. This is also the case of how a normal 'strong topological insulator' works, with robust light transmission known as edge state, which can be found along with the interface between the trivial and nontrivial unit cells. As shown in the inset images in Figure 3.4A-B, by studying a single supercell with periodic boundary conditions only in one direction (here, we define the y-direction as periodic), whether edge states exist or not can be verified. In our simulation, two kinds of supercells are formed by arranging seven (rotated) nontrivial unit cells followed by seven trivial unit cells along the x-direction (the inset images only show the adjoining section of them). In this way, we find a unidirectional edge mode (indicated by the red dots) within the bandgap when the a-Si

nanopillars in the trivial and not-rotated nontrivial unit cells are arranged as shown in the inset in Figure 3.4A. The edge state is a result of the corresponding nontrivial Zak phase $\theta_{\Gamma X} = \pi$ and the periodic direction of the unit cell in the y-direction. The field distribution of the edge state is shown in Figure 3.4C, with the mode that is followed by the physical interface of trivial and nontrivial unit cells. On the other hand, no edge state can be found in the supercell if we replace the left part with rotated nontrivial unit cells as $\theta_{\Gamma Y} = 0$ in such a design (Figure 3.4B).

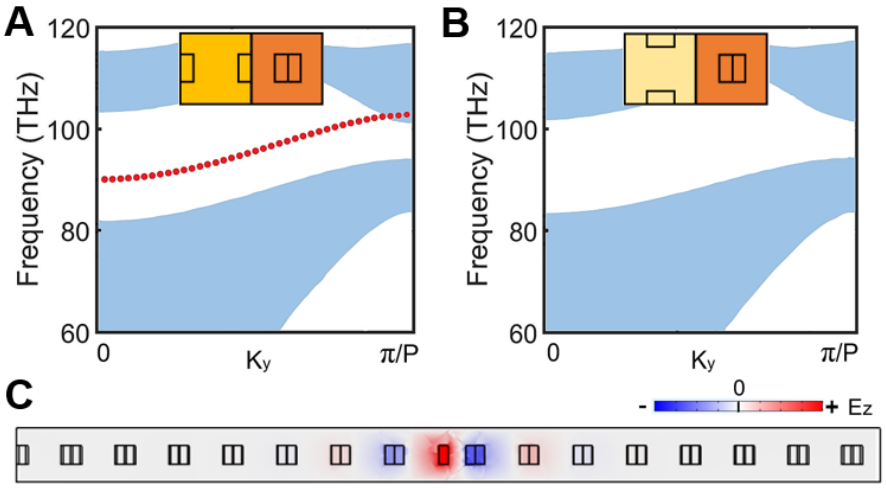

Figure 3.4 Band structure of the supercells to verify the edge state. The inset images show the adjoining part of the supercell. The red dotted line corresponds to the edge mode and the bulk modes are shaded with light blue shaded. The edge state is present only with initial nontrivial/trivial unit cells (A), while no edge state exists if the nontrivial unit cells are rotated (B). (C) The field distribution of the edge state, with the field is centered along with the physical interface of trivial and nontrivial unit cells.

3.3.3 Comparison of nontrivial and trivial designs with a dislocation

Following the idea of the weak topology design, a proper structural defect should be arranged with only one kind of unit cell to achieve the topologically protected state. Here, with the nontrivial unit cells as an example, we introduce a structural defect in a TPhC with uniformly arranged unit cells as shown in Figure 3.5A-B. In the first step, we partly remove the centerline of the unit cells (from the one shadowed in red in all the figures, which sits at the 11^{th} line in the y-direction, and the 10^{th} unit cell in the x-direction) in the uniform TPhC with 26*21 units. Then, all the units above and below the removed section are shifted linearly along the y-direction towards the centerline (see the illustration by red arrows, formed with seven rows, defined by $L = 7$) to compensate for the removal of one line. This procedure creates an edge dislocation with a single pillar in the middle as the dislocation center. A closed-loop, as shown by black arrows in Figure 3.5A, results in a Burgers Vector $\mathbf{B} = (0, P)$ (the light blue arrow) along the y-direction in real space.[94] This Burgers Vector can be used to describe this dislocation we created and is only determined by the way of creation (no relation with the unit cell). Finally, the dislocation center (single-center pillar) is further extended with N more unit cells (here $N = 4$, the number of unit cells from the one shadowed in red) as shown in the

direction of the dashed arrow. The dislocation center extension helps reduce the mode scattering around the pillar.

Here, the weak topological invariant Q (which equals the number of localized modes in such a design) contains both parameters from the band structure topology and crystal dislocation although the design strategy has much difference compared with previous research:[6, 95]

$$Q = \frac{1}{\pi}\boldsymbol{\theta} \cdot \mathbf{B}: \mathrm{mod}\ 2 \tag{3.2}$$

where $\boldsymbol{\theta} = \left(\frac{\theta_{XM}}{P}, \frac{\theta_{YM}}{P}\right)$ represent the Zak phase information of the band below the gap along with the *XM* and *YM* line, respectively; **B** describes the crystal edge dislocation in real space. Q can only be 0 (no localized mode) or 1 (with a localized mode). According to this defined Q, the case when the nonzero Zak phase vector $\boldsymbol{\theta}$ and the Burgers Vector **B** are parallel to each other can result in the topologically protected localized mode. This topological concept was termed "weak" to distinguish it from the well-known strong topological insulators (where "strong" is always omitted) which are solely characterized by a quantized scalar topological invariant.[95]

To verify that the localization only appears in the nontrivial design based on weak topology and the weak topological invariant Q, we study the spectra and electric field profiles of three TPhCs. Please note, that the comparison here only uses the design with $N = 4$, while more other trivial cases will be introduced in the latter part to verify our design. Based on the 2D Zak phase or E_z field distribution in Figure 3.3B, the nontrivial unit cell gives rise to $\theta_{YM} = \pi$, while $\theta_{XM} = 0$ as for the parity inversion difference; and both θ_{YM} and θ_{XM} are equal to 0 for the trivial unit cell. This results in the three TPhCs we want to study here: *Nontrivial* (Figure 3.5A-B), which is constructed by the initial nontrivial unit cell with $\boldsymbol{\theta}$ parallel to **B**, and $\boldsymbol{\theta} = (0, \pi/P)$; *Trivial 1* (Figure 3.5D), constructed by the trivial unit cell with $\boldsymbol{\theta} = (0, 0)$; *Trivial 2* (Figure 3E), constructed by the 90-degree rotated nontrivial unit cell with $\boldsymbol{\theta} = (\pi/P, 0)$ perpendicular to **B**. Note here, the design strategy resulted with the same Burgers Vector for all three cases, as explained above for the dislocation formation. Coinciding with our assumptions and the weak topological invariant Q, only one localized mode (f = 96.7 THz) in the bandgap (94.4 THz — 101.6 THz) around the dislocation center is found for the *Nontrivial* design as shown in Figure 3.5B-C. In contrast, both trivial designs (*Trivial 1* and *Trivial 2,* Figure 3.5D-E) do not show any localized state inside the bandgap. All results here meet our design strategy to realize the in-bandgap localized mode with the nontrivial Zak phase and edge dislocation.

The presence of localization is also similar to the investigation from the well-known cut-and-glue method by assuming that the TPhC is cut into two parts along the y-direction and separated before and after the defect starting position. If we use the nontrivial unit cell in the TPhC, two edge states are found intersecting at $k_y = \pi/\mathrm{P}$ which can be described by a massive

Dirac equation (see the presence of the edge state in Figure 3.4). In particular, the Zak phase (with a different direction) expressed with $\boldsymbol{\theta}$ can introduce a π phase difference for both edge states when its direction is identical with B, which means the mass term for this Dirac cone changes sign before and after the dislocation. This sign difference acts as a mass domain wall of the Dirac equation, and the mass domain wall here can host a weak topologically protected mode around the dislocation center.

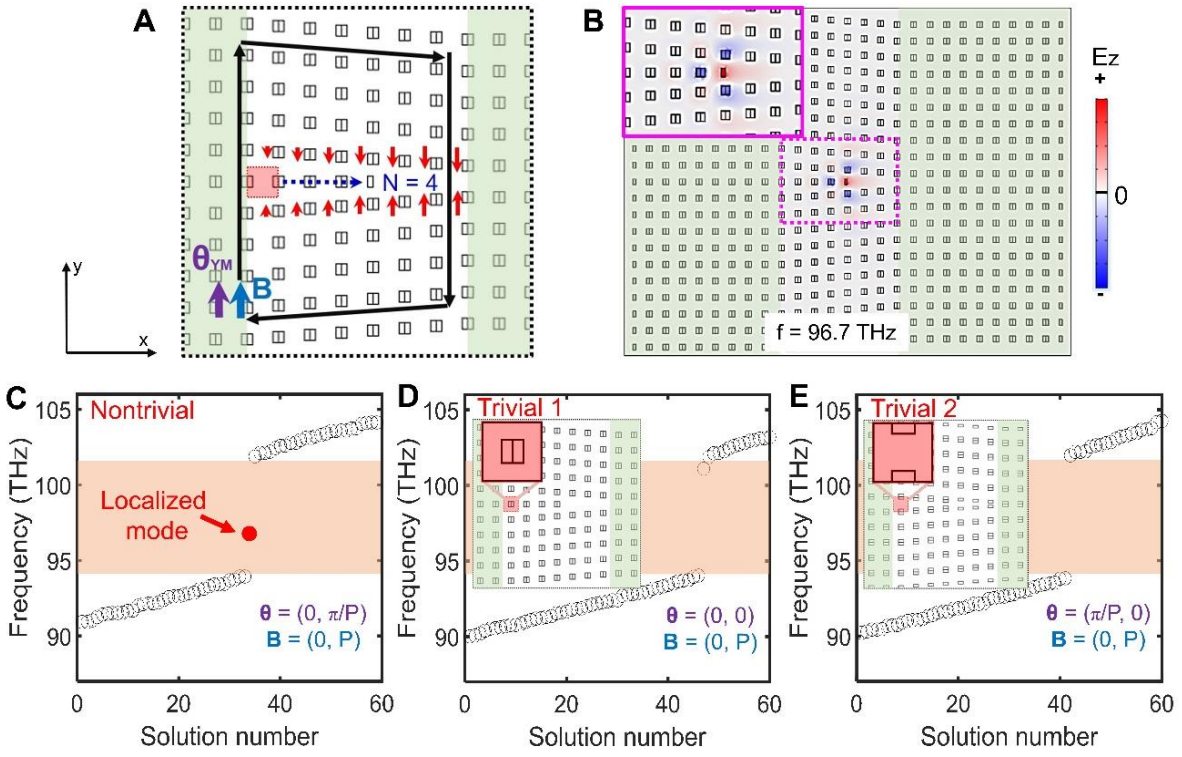

Figure 3.5 Comparison of three kinds of TPhCs. (A) Illustration of the defect formation with the nontrivial design as an example, the two solid arrows with purple and light blue colors indicate $\boldsymbol{\theta} = (0, \pi/P)$ and $\mathbf{B} = (0, P)$. The uniform area (corresponding to the uniformly arranged red shadowed unit cell, same in all the other designs) is shadowed with green. The dark blue dashed arrow indicates the extension of the dislocation center with $N = 4$ more unit cells in this case. (B) E_z field distribution was obtained from the eigenmode of the marked in-gap localized mode in the spectrum from the *Nontrivial* design. The dotted purple line marks the area for the magnified view shown as an inset. (C) The spectrum of the *Nontrivial* design with the localized mode in the bandgap. (D) The layout at the dislocation center and spectrum of *Trivial 1* design with $\boldsymbol{\theta} = (0, 0)$. (E) Layout at the dislocation center and spectrum of *Trivial 2* design with $\boldsymbol{\theta} = (\pi/P, 0)$. The unit cell in the red box (A, D, and E) shows the starting position of the dislocation center extension for each design. The bandgap region (94.4 THz — 101.6 THz) obtained from the band structure of the unit cells is shadowed in orange.

3.3.4 Versatility of localization achievement for different dislocation extensions

As the localization that is realized with a dislocation design should be under topological

protection, this may provide more design layouts that possess similar localization. This versatility of design strategy to achieve the 0D localized state is proved as shown below in Figure 3.6. We consider three design layouts still with the nontrivial unit cell, but with a different number N of unit cells extending the dislocation center (see illustration of N in Figure 3.5A, corresponding to $N = 3, 5, 6$ for the three layouts here) as shown below in Figure 3.6. All the calculated spectra (top row) still show a localized mode inside the bandgap as marked by the red dot. And the few localized frequency shifting can be understood by the structural change of each design. What's more, similar electric field confinement around the dislocation center can also be observed (bottom row) as shown by the E_z field, with tighter localization is observed for larger N.

The presence of localization in these designs is because the unit cell extensions at the dislocation center do not change any parameters in the weak topological invariant, which provides further verification of the design strategy. The change of localization may also be applied for some specific design cases if one wants to turn it under control.

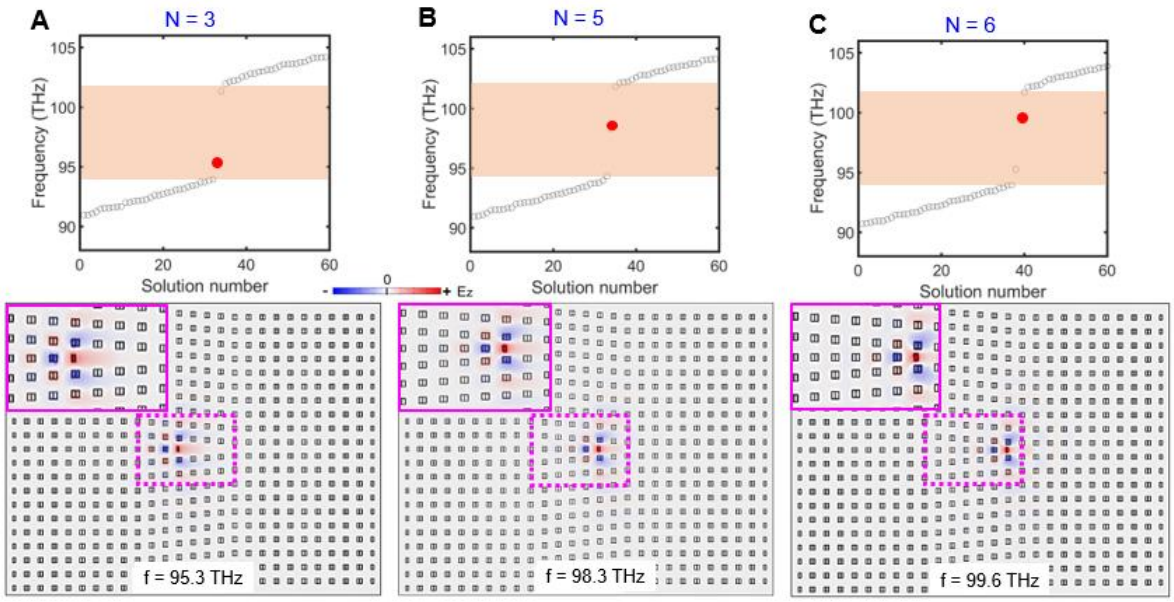

Figure 3.6 Versatility of the weak topological design. The versatility of the weak topology design to achieve the 0D localized mode with three different unit cell extensions at the dislocation center for (A) $N = 3$, (B) $N = 5$, and (C) $N = 6$, respectively. The top row shows the spectra; the bottom row shows the simulated field distribution from the eigenmode solver. The dotted lines mark the area of the magnified inset in the simulation images.

In stark contrast to these nontrivial designs above, no topologically localized mode can be found in all the corresponding trivial TPhCs as shown in the comparison between the nontrivial and trivial TPhCs for different N in Figure 3.7. And N in both nontrivial and trivial TPhCs are based on the number of unit cells from the No. 10^{th} one (see the column in the green dotted box in Figure 3.7B) at the centerline. The corresponding trivial TPhC ($\theta = (0, 0)$) we choose here

is because no dramatical change of the unit cell the at centerline for larger N. See Figure 3.5E above, the two pillars at the centerline are moved closely in the other trivial case ($\boldsymbol{\theta} = (\pi/P, 0)$) even when $N = 4$, this could make the determination of mode a challenge.

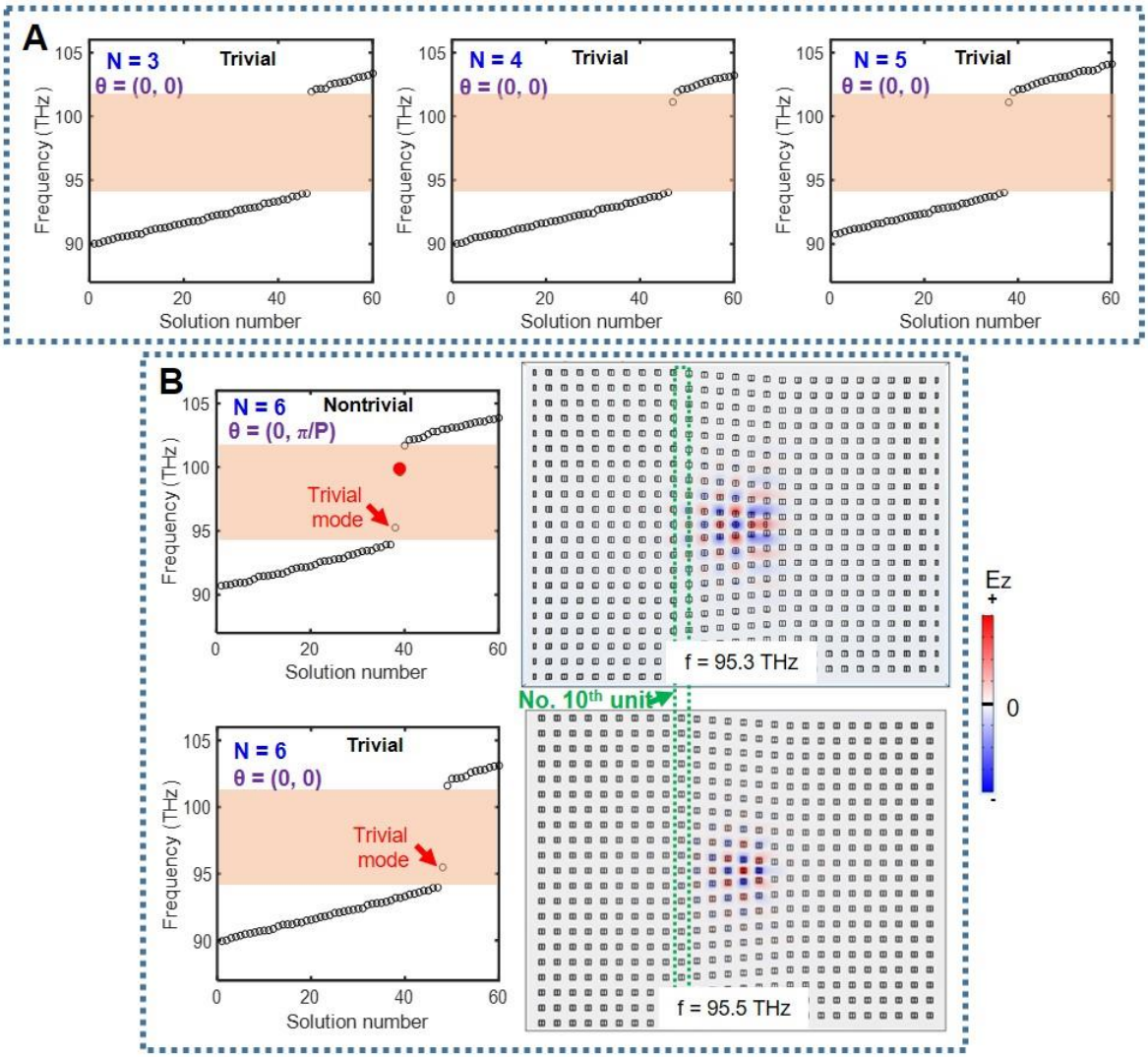

Figure 3.7 Corresponding trivial TPhCs with different *N*. (A) No in-bandgap trivial mode exists in the three corresponding trivial TPhCs for $N = 3, 4, 5$. (B) In-bandgap trivial modes for $N = 6$ from both trivial and nontrivial TPhCs are indicated by red arrows. The E_z field with a similar distribution of these two trivial modes in (B) is shown on the right. The results show that these modes (we marked with red dots in Figure 3.6) only exist in nontrivial TPhCs and N are shown in each case, and Burgers vectors for all the TPhCs are still $(0, P)$.

According to principles of topology, only topological nontrivial modes can appear during the topological phase transition. The continuous wave nature of our system inevitably introduces further complexities and allows the appearance of excessive trivial modes. However, we find that the topological mode's appearance follows the topological phase transition, while the trivial modes (if there are any) only experience minor frequency shifts. This means all the

in-gap modes marked with red dots (N = 3, 4, 5, 6) are nontrivial modes as they only exist in the nontrivial TPhCs. While the modes (marked out with red arrows in Figure 3.7B) near the band edge in both spectra are trivial, as they exhibit similar frequency and field distribution for both trivial and nontrivial TPhCs.

3.3.5 Characterization of the localization from simulation

With the nontrivial design for N = 4, we investigate more characteristics of the localization from the simulation. First, the mode area and robustness of the localization are characterized. Furthermore, we also provide spectral information and near-field distribution near the localization, which supports the possibility to detect the mode by near-field measurement later.

The electric field profile of the designed localized mode in Figure 3.5B suggests a mode area of ~ 0.25 λ^2 (λ is the wavelength in vacuum) around the dislocation, which indicates a more strongly confined mode compared to other topological designs like HOTIs and the Dirac vortex method. Here, the mode area of the localization is calculated with the following formula:

$$A_{eff} = \frac{\left(\int |E_z(\boldsymbol{r})|^2 d^2\boldsymbol{r}\right)^2}{\int |E_z(\boldsymbol{r})|^4 d^2\boldsymbol{r}}, \tag{3.3}$$

where $|E_z(\mathbf{r})|$ is the z component of the electric field, and the integration is performed on top of the structure (in the plane at z = 680 nm). With this mode area definition, it's also significant to note that the smallest mode area of ~ 0.17 λ^2 is achieved for the design with N = 6 due to the scattering suppression with a smaller vacant area in the array (largest mode area ~ 0.36 λ^2 for N = 3). The possibility to tune the mode area also shows the advantage of weak topology design from another aspect.

Furthermore, a well-known quality of TPhCs is the robustness of modes, i.e., localization and light transmission to fabrication tolerances and disorder. To investigate the robustness of the topological mode, we add random position perturbations to the pillars in both x and y directions and numerically simulate the nontrivial TPhC for N = 4. With standard deviations of 50 nm (Figure 3.8A), 100 nm (Figure 3.8B), and 130 nm (Figure 3.8C) for the random position perturbations, it is found that the topologically protected localized mode remains with minor frequency shifts. In addition, other characteristics of the localization (like localization position, area, and phase profile) remain similar. The simulation results here verify that the localization based on weak topology still possesses a robust nature like strong topological insulators.

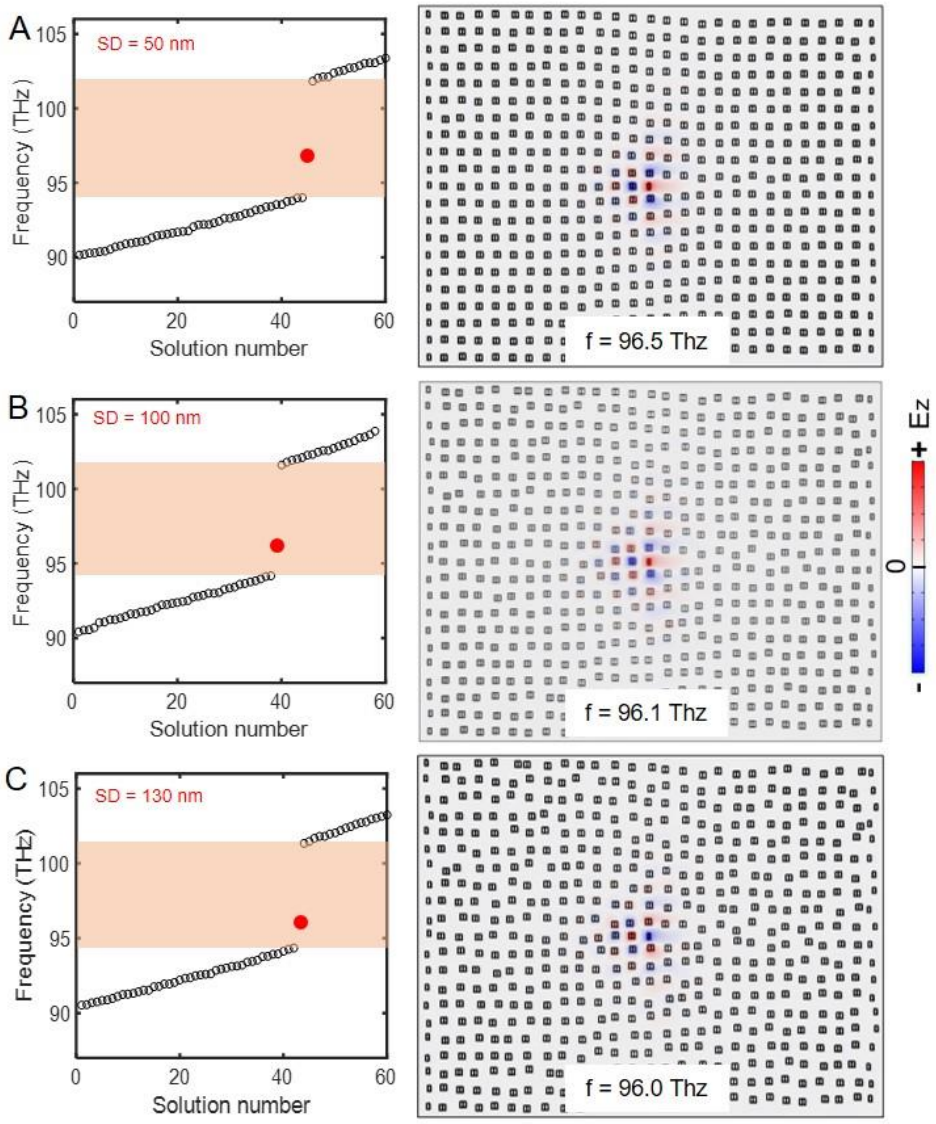

Figure 3.8 Robustness of the mode by weak topology. Spectra of the nontrivial TPhC (N = 4) with the localized mode (red dot) in the bandgap after random position perturbations with different standard deviations. (A) 50 nm, (B) 100 nm, (C) 130 nm. E_z field distributions corresponding to each in-gap localized mode in the spectrum are shown on the right.

Then, we show the absolute value of E_z field distributions around the dislocation center for the localized mode (f = 96.7 THz), which are plotted with different planes at z-direction (for heights from 650 nm to 800 nm) as shown in Figure 3.9A. As the height of the pillars is 673 nm, and the brightest position corresponds to the center single pillar is always found as shown in the corresponding area in Figure 3.9B. These results prove the strongly confined localization within a small volume around the center pillar as all the planes show a strong field enhancement around the single pillar. Even if the s-SNOM tip is not too close to the pillar, the field distribution also provides the possibility to detect the localized mode by a near-field scanning technique, like s-SNOM, as field distribution difference can still be recognized easily

even for the height of 800 nm.

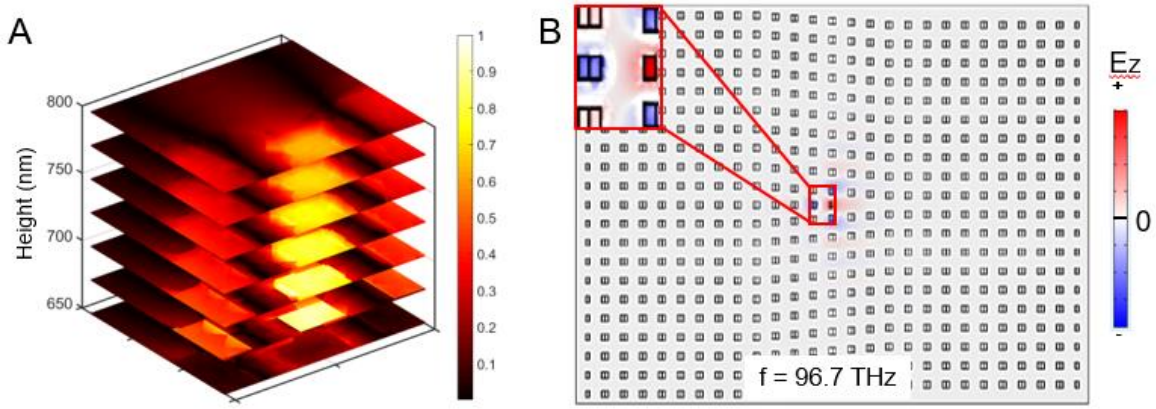

Figure 3.9 Field distributions around the dislocation center for the localized mode. (A) Normalized $|E_z|$ field distributions around the dislocation center (with the brightest position corresponding to the contribution from the single pillar at the center for f = 96.7 THz) plotted with different planes at z-direction (from 650 nm to 800 nm). (B) Simulated field distribution with the corresponding area plotted in (A) is marked with a red box. All planes show a strong field enhancement around the dislocation center, which proves the possibility to detect the localized mode by scanning the s-SNOM tip around the pillars.

On the other hand, the near-field enhancement can be estimated from simulation with COMSOL under certain excitation conditions by a background wave we use here. During the simulation, the background electric field direction and polarization were set according to the possible measurement condition (55° concerning surface normal) with a linear polarized plane wave. We use a hemispheric perfectly matched layer as the boundary of the simulation domain. A perfect magnetic conductor was used for the x-z plane (perpendicular to the bottom) due to the mirror symmetry of the layout, which can increase the simulation efficiency. From the electric field above the pillars (z = 680 nm) at the localized frequency of f = 96.7 THz, a field enhancement larger than 30 times can be found around the pillar at the dislocation center as shown in the top image of Figure 3.10A. The field pattern around the pillar at the dislocation center looks similar to the results from the eigenmode solver, which further supports our design strategy. For comparison, we also checked the E_z field distribution for the other frequency at f = 93.9 THz without tight localization: A rather weak field distribution over a broad area is observed, corresponding to the bulk modes based on the simulation.

Under background field excitation, the z-component of the normalized near-field (*Ez*) against the incident plane wave at the defect center (with the data from the top corner of the pillar) is also plotted for different frequencies in Figure 3.10B. A narrow resonant peak can be found whose frequency corresponds to the localized mode. The spectral information confirms the topologically localized mode as an optical resonator, which is important to increase light-matter interaction.

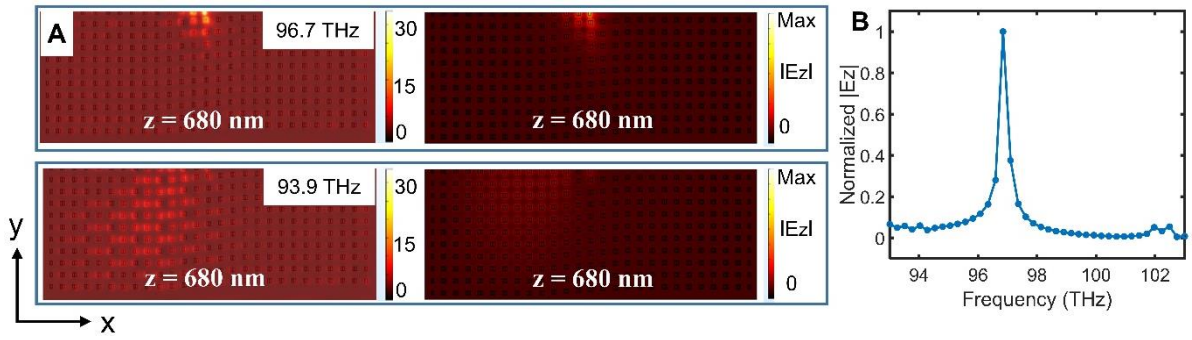

Figure 3.10 Near-**field for the nontrivial TPhC under plane wave excitation.** (A) Extracted electric field distribution from the simulation at z = 680 nm with background excitation (left column) and results from the eigenmode solver (right column). Both simulated results show similar electric field distributions, verifying the field enhancement around the localized center. (B) A narrow resonant peak can be recognized for the in-bandgap localization based on the results from plane wave excitation.

3.3.6 Simulation results for more trivial and versatile cases

Besides the $\boldsymbol{\theta}$ and **B** we use in the previous part, there are also other cases with a different unit cell or another way of dislocation arrangement. In this part, we will provide more trivial cases to prove that the presence of localized modes is still determined by the same weak topological invariant in Equation 3.2.

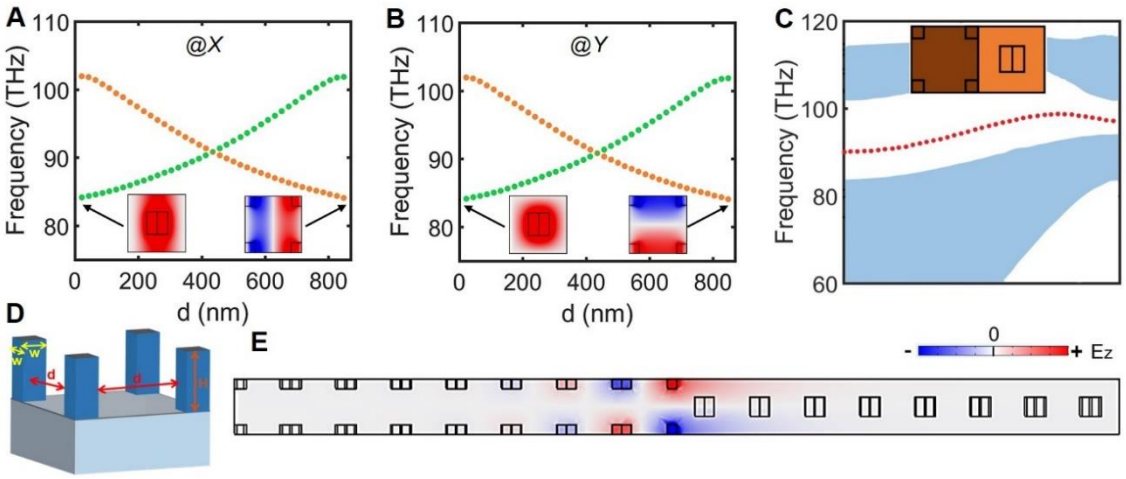

Figure 3.11 Band structure analysis of the TPhC with θ = (π/P, π/P). (A and B) Evolution of the two lowest bulk states at the X or Y point with different *d*. Inset images show the *z* component of electric fields (E_z) for the first band at different *k* points, which can be used to determine the Zak phase intuitively. (C) Band structure of the supercells to verify the edge state. The inset images show the adjoining part of the supercell. The red dotted line corresponds to the edge mode and the light blue shaded area are the bulk modes. (E) The field distribution of the edge state. (D) Schematic illustration of the with θ = (π/P, π/P) made of a-Si nanopillars on a Cr film. The unit cell is designed by uniformly splitting the Si antennas in the previous trivial unit cell and putting them at each corner.

These designs are based on the unit cell with $\boldsymbol{\theta}$ = (π/P, π/P) or dislocation with **B** = (*P*, *P*).[82, 94] The unit cell is shown below in Figure 3.11, with four pillars possess the same size sitting at each corner of the unit cell. As discussed in the previous part, the electric field distribution at the *X* and *Y* points shows that the nontrivial π Zak phase emerges for both $\theta_{\Gamma X}$ and $\theta_{\Gamma Y}$ (inset image of Figure 3.11A-B). The edge state is calculated in a similar way here (with the field distribution is shown below) and also verified that the unit cell is a nontrivial one.

To investigate the design for **B** = (*P*, *P*), the Burgers vector is formed by removing half row in the x-direction and half-column in the y-direction as shown in Figure 3.12A when $\boldsymbol{\theta}$ = (π/P, π/P) and Figure 3.12B when $\boldsymbol{\theta}$ = (0, 0) based on the reference. Because the case $\boldsymbol{\theta}$ = (π/P, π/P) needs a unit cell with four pillars, the reshaping of unit cells to form the edge dislocation makes the design and mode analysis more complex. For convenience, only two columns (defined by *L*, *L* = 2 here) or rows of unit cells are used to form the defect, which results in fewer unit cells reshaping to form the defect (otherwise the pillars at the defect area could touch with each other). Note here, reducing the column and row number around the defect center (two columns and two rows) will still give a topological mode in the nontrivial design for **B** = (0, *P*) as we investigated later. Here, no topological mode inside the bandgap can be found for both designs with **B** = (*P*, *P*), consisting of our assumption.

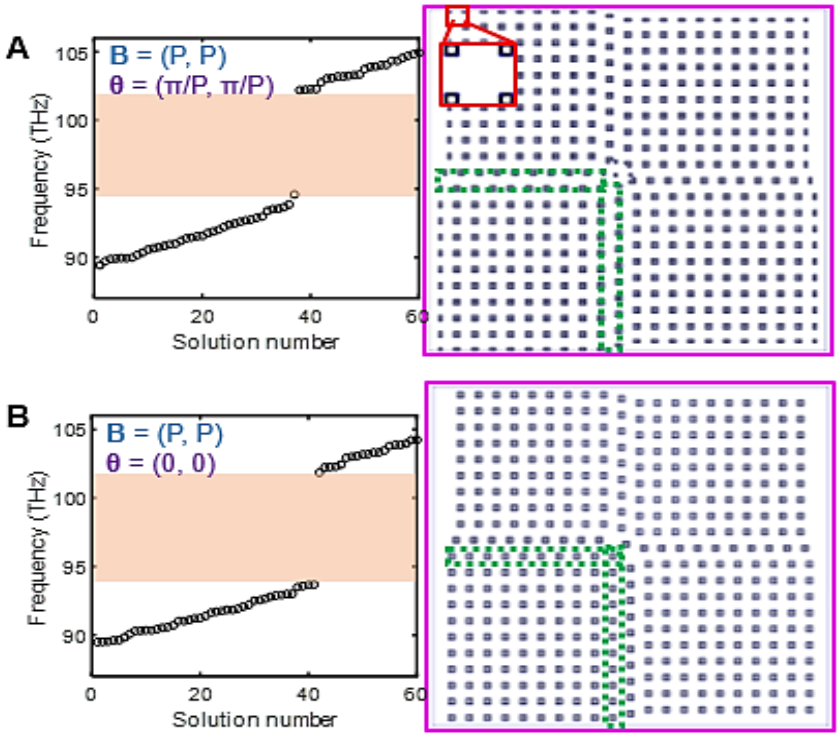

Figure 3.12 Comparison of trivial TPhCs with B = (*P*, *P*). (A) Spectrum and design layout for **B** = (*P*, *P*) when $\boldsymbol{\theta}$ = (π/P, π/P), (B) results for **B** = (*P*, *P*) when $\boldsymbol{\theta}$ = (*0*, *0*), no topological mode inside the bandgap can be found for both designs. The red box in (a) shows the unit cell for $\boldsymbol{\theta}$ = (π/P, π/P), which is formed by splitting the pillars in the trivial design ($\boldsymbol{\theta}$ = (0, 0)) into four equal parts and putting them at each corner. The two green boxes in (A) and (B) show the remaining part of the unit cells to form the defect.

On the other hand, to further demonstrate the versatility of weak topology design, we consider several design layouts based on the nontrivial unit cell as shown below. They are designed to meet the nontrivial weak topological invariant in Equation (3.2), but with a different column (L) of unit cells to form the dislocation, or a different unit cell extension (defined by N same as the previous part). The calculated spectra (top row) still show a localized mode inside the bandgap as marked by the red dot, and similar field confinement around the dislocation center can be observed (bottom row).

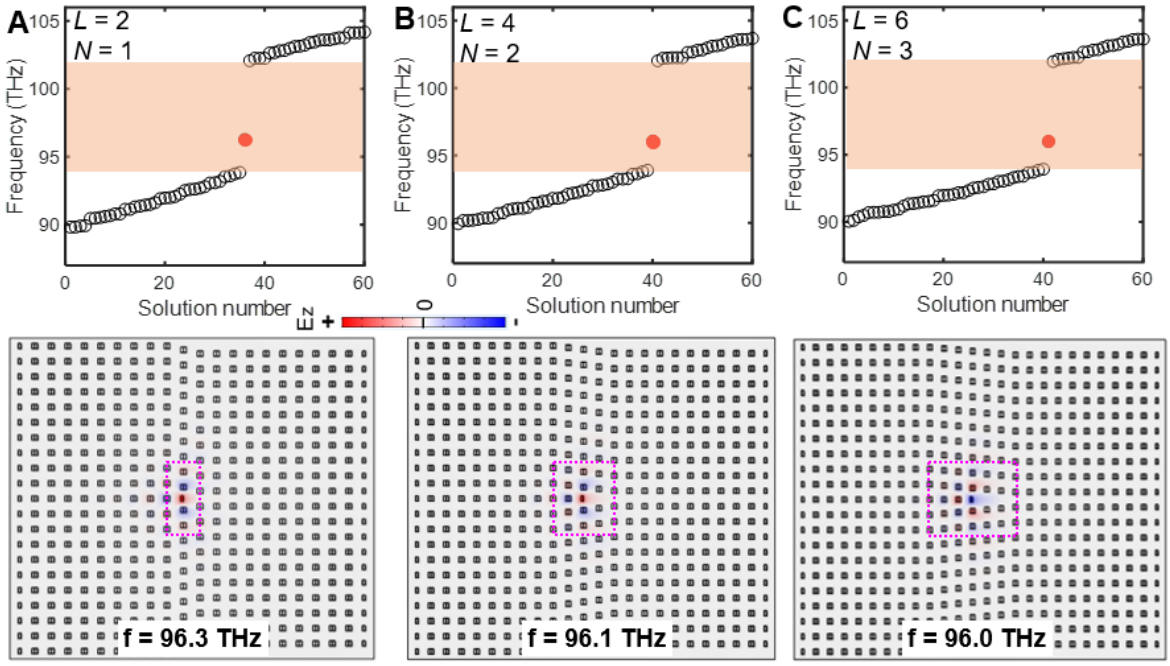

Figure 3.13 Versatility of the weak topological design to achieve the topologically protected mode. Three nontrivial TPhCs with different columns or unit cell extensions are used to form the defect. (A) L = 2, N = 1; (B) L = 4, N = 2; (C) L = 6, N = 3. A topological mode can still be found in the nontrivial design (as marked with the red circle, with the field distribution is shown at the bottom row). The purple dotted lines illustrate five rows of unit cells to construct the dislocation, while the length of these dotted lines corresponds to different column numbers (L).

3.3 TPhC fabrication and optical near-field measurements

Recently, characterizations of TPhCs with an s-SNOM have been reported for corner states in HOTIs and edge states in a valley photonic crystal for the first time, while aperture-based near-field optical microscopy has also been used to map edge modes.[96-98] All these researches showed some advantages of measuring topological mode by SNOM, like subwavelength resolution and the possibility for direct quantitative evaluation of the measured states. However, a spectroscopic study by s-SNOM of the evolution of the eigenmodes within a TPhC over a relatively wide spectral range including the bandgap as well as bulk modes has yet to be demonstrated. This means that although the advantages of applying s-SNOM to

TPhCs have been verified, more applied situations remain unclear, especially at the nanoscale. Here, we use s-SNOM to spectroscopically characterize the designed subwavelength optical localization with the fabricated samples.

3.3.1 TPhC fabrication

The TPhC is fabricated with a normal EBL process similar to the introduction in Chapter 2. But there are also some differences in the substrate preparation case to case. Here, the detailed information to fabricate this sample is shown below in Figure 3.14. First, a thin Cr film with a thickness of 100 nm was deposited on a cleaned glass substrate by electron beam evaporation. An a-Si layer of thickness 673 nm was deposited by plasma-enhanced chemical vapor deposition (PECVD), immediately on top of the Cr film. The sample with deposited a-Si on top of the Cr film was then used to perform the subsequent processes to transfer the desired patterns onto a-Si as follows. A poly-methyl-methacrylate (PMMA 950K, AR-P 679.03) resist layer was spin-coated onto the a-Si film and baked on a hot plate at 170 °C for 2 mins to remove the solvent. The desired structures were patterned by using a standard EBL process and developed in AR 600-56. Next, another 20 nm thick Cr mask was deposited by electron beam evaporation. After a lift-off process in AR 300-76 (Remover, AllResist GmbH), the patterns were transferred from PMMA to Cr. Finally, the structures were transferred onto a-Si using an ICP-RIE process and the following removal of the Cr mask is conducted by a commercially purchased Cr-etch solution (TechniEtch Cr01).

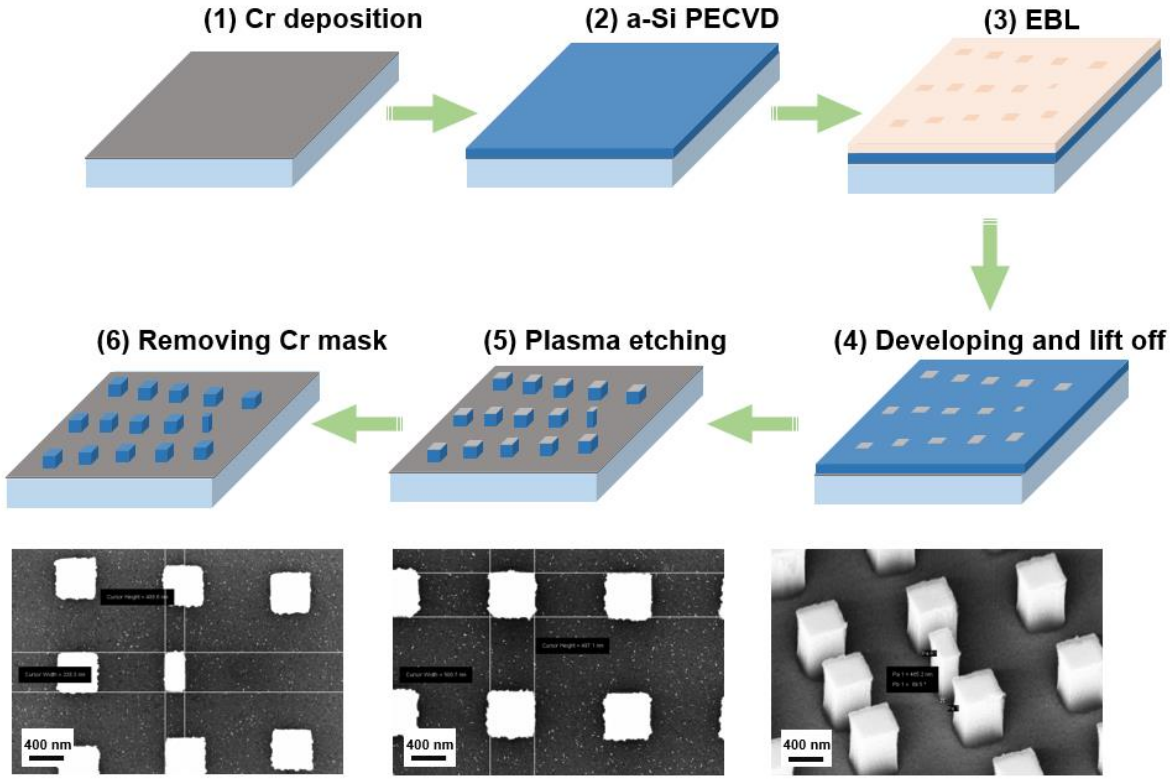

Figure 3.14 Illustration of TPhCs fabrication. The sample fabrication process mainly includes 6 steps. (1) Cr deposition, (2) a-Si deposition by PECVD, (3) EBL patterning, (4) Developing the patterned resist layer and lift off, (5) Plasma etching of a-Si with the Cr mask, (6) Removing the Cr mask. The antenna dimension after fabrication based on our measurement is around 238 nm*488 nm*660 nm.

As shown in the SEM images in the last row of Figure 3.14, the Si nanopillars after fabrication present good shape, with size dimensions similar to the simulated definition. To achieve such a good quality fabrication, the two most critical steps are the EBL and ICP-RIE as we introduced in Chapter 2.

3.3.2 Near-field measurement and data processing

Here, we use s-SNOM to conduct spectroscopic studies on the evolution of the eigenmodes within the TPhC over a wide spectral range. An s-SNOM set up by Neaspec GmbH in pseudo-heterodyne detection mode in combination with an LN_2 cooled InSb detector optimized for the wavelength range up to 5.4 μm is applied to record amplitude and phase data simultaneously.[99, 100] The s-SNOM is operated in tapping mode at oscillation frequencies between 220 and 270 kHz, with commercially available metal-coated atomic force microscope (AFM) probes. The tapping amplitude is 40-60 nm. The laser source is a commercially available optical parametric oscillators/amplifier pulsed laser (Alpha Module by SI-Instruments) tunable between 65 to 217 THz, with a repetition rate of 42 MHz and a pulse duration of up to 1 ps. This provides a spectral resolution of 1.5 THz and allows for recording images in s-SNOM in pseudo-heterodyne detection mode around 100 THz (~ 3 μm). We

extracted the signal from the second demodulation order amplitude. The spectral resolution of the laser leads to a smearing of the states compared to the simulations which work at a single frequency. Thus, not every eigenstate is perfectly localized as expected from simulations.

In real operation, s-SNOM records the scattering amplitude and phase of the optical near-fields at the AFM tip at a certain laser frequency by lock-in detection. The signal is then demodulated at higher harmonics of the tip's oscillation frequency. Between the pillars, as the AFM probe picks up the strong background signal of the Cr substrate, the substrate area is not used for evaluation and is set to zero in our results. Instead, the second-order normalized amplitude (S_2) images in all the results were obtained by evaluating the amplitude signal on top of the pillars. The top pillar position was determined by setting a threshold value in AFM images and overlaying with the corresponding optical images, setting the surroundings to zero. Afterward, the signal was averaged over two neighboring pixels with a Gaussian filter to smooth the pixels and normalized to the signal on top of the middle pillar (dislocation center with a single pillar) to highlight the field distribution.

The step-by-step data analysis is shown in Figure 3.15 with the measured result performed at 96.7 THz as an example. First, the AFM signal is used to determine the top of the pillars by discriminating below a certain height. Then, the optical amplitude signal is obtained at a position where the height is above this threshold, and the amplitude value is set to zero at lateral positions below this threshold. This yields the amplitude signal on top of the pillars (Figure 3.15C). To make the amplitude signals comparable between different frequencies the signal needs to be normalized. Thus, the signal on top of the middle pillar at the defect center (the green rectangle) is used for normalization and obtaining the normalized optical amplitude image (Figure 3.16E). Finally, a Gaussian filter is applied to the image to reduce the noise and the color bar is scaled from 0 to 1. The same procedure was applied to all the amplitude images in this chapter. Most of the background signal from the bottom is removed with this procedure.

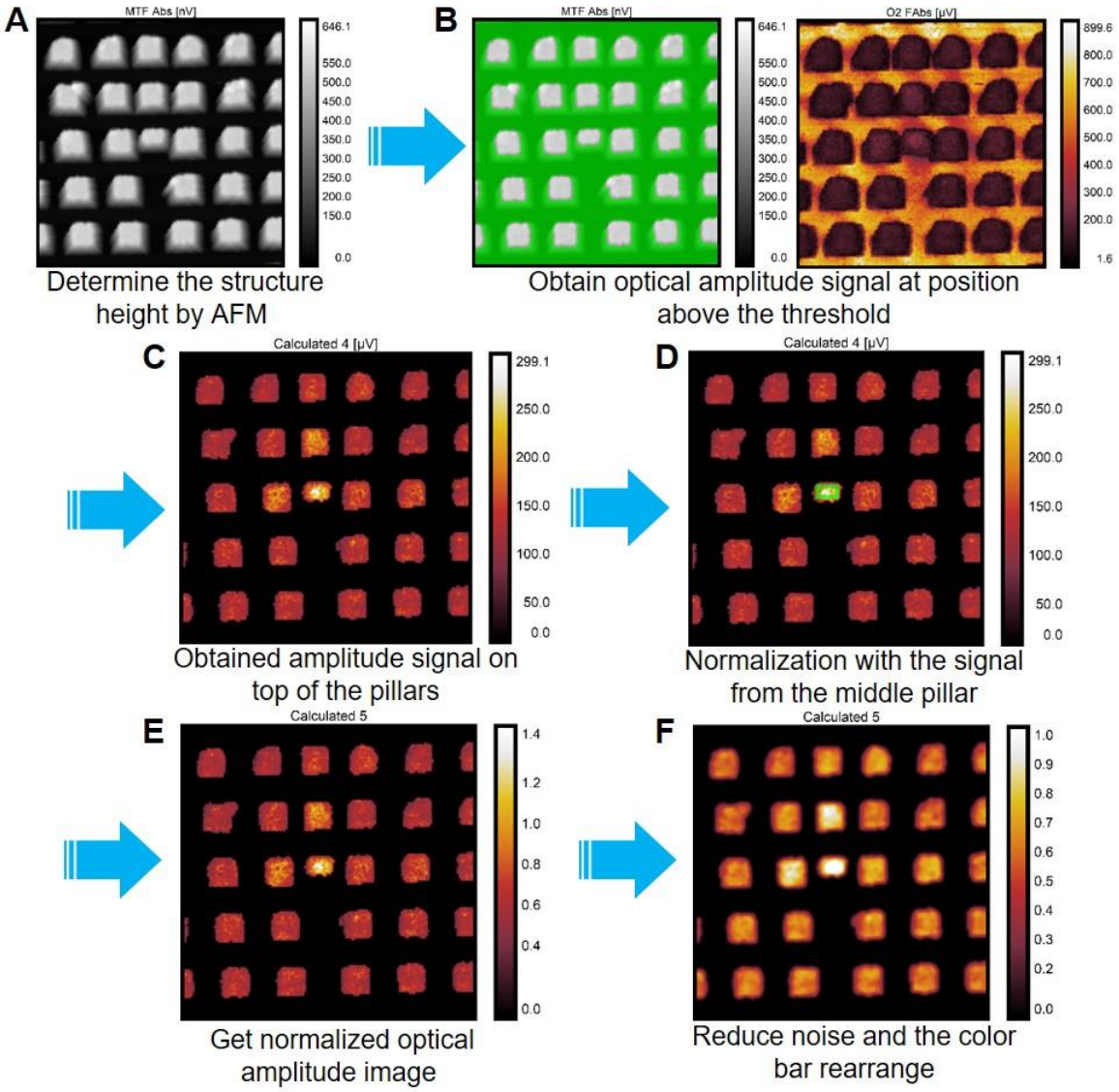

Figure 3.15 Flow chart for the processing of the raw data from s-SNOM amplitude measurements. (A) The raw data of the s-SNOM's AFM. (B) Left: AFM image with a threshold mask to determine the top of the pillars. Right: S_2 optical amplitude image, where the very high optical signal between the pillars is because of the interaction between the s-SNOM's tip and the Cr at the bottom. (C) The obtained amplitude signal is on top of the pillars. (D) The referencing region is indicated by the green box. (E) The normalized optical amplitude image. (F) Final normalized optical amplitude image with a Gaussian filter applied to reduce noise. The signal on the middle pillar in all images is around 1 after processing. Thus, the contrast from the pillar at the defect center to the surrounding pillars indicates the relative field strength on top of the pillars.

3.3.3 Spectral comparison between simulation and experiment

As supported by the simulation in the previous part, the spatial localization of the mid-bandgap eigenmode is possible to be visualized by measuring the near-field distribution of the TPhC with excitation by an obliquely incident beam. In Figure 3.16B of the related spectrum

from the nontrivial design with $N = 4$, we measured the four investigated frequencies that are indicated by the red markers. E_z fields (in the plane at z = 680 nm) from the Eigenmode solver corresponding to the near-field distribution at each frequency are shown below the experimental s-SNOM results in Figure 3.16C. A strongly confined field localized around the single pillar at the dislocation center is measured for the frequency of the state in the bandgap (f = 96.7 THz), whereas the other frequencies show weaker localization and broader field distributions. Interestingly, we also observe the two Eigenmodes at the band edge (f = 93.9 THz and f = 102.0 THz), where a slight localization around the center pillar can be seen. At 100 THz, where no eigenstate is expected within the bandgap, the measured signal on the pillars is comparable to the center pillar. The light is scattered non-resonantly by the array. That the pillars at the center appear slightly uniformly brighter can be explained by the spectral resolution of ~ 1.5 THz of the tunable laser source. Therefore, the eigenstates within this spectral range around 100 THz, especially at the band edge (f = 102.0 THz) and in the bandgap (f = 96.7 THz) can also be slightly excited. This overlap is reflected in the measured signals, like the middle pillar in Figure 3.18C, giving rise to bright regions in the measurements even though the actual field values might be relatively small (see simulations).

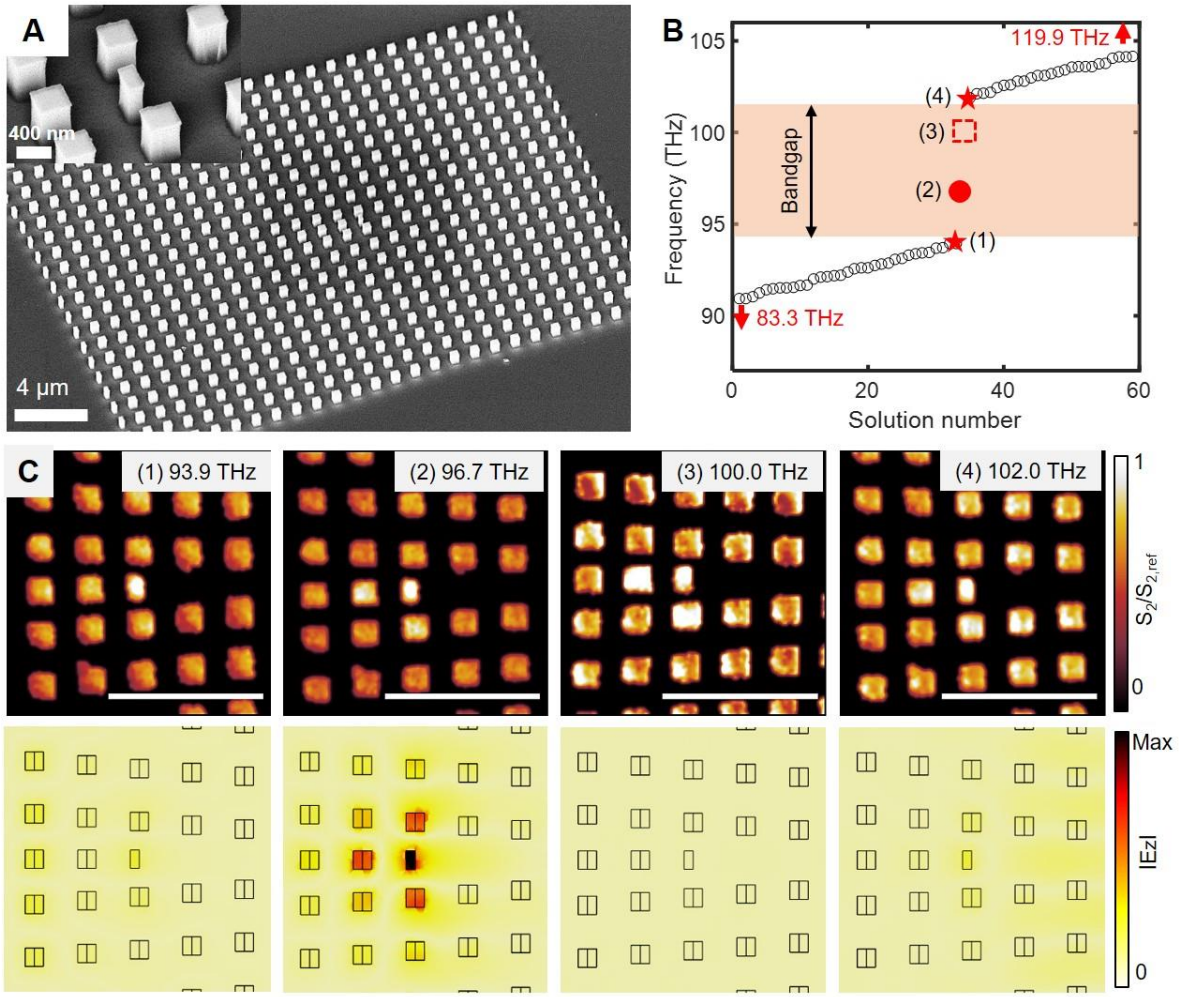

Figure 3.16 Frequency-dependent near-field results. (A) SEM image of the nontrivial TPhC with $N = 4$ (inset: magnified view of the dislocation center). (B) Corresponding spectrum with the measured frequencies marked with red markers. (C) Normalized s-SNOM amplitude images to show the measured electric field distribution (top) and the simulated E_z fields (absolute value) obtained from the eigenmode solver (bottom) for each frequency. The subwavelength localization with strong fields around the single pillar at the dislocation center is observed in the bandgap at $f = 96.7$ THz, while the fields for other frequencies show weaker localization and broader distributions. Scale bars are 4 µm.

In Figure 3.17, normalized S_2 amplitude images for more measured frequencies and an additional position without localization are shown to support the measured results. $f = 83.3$ THz and 119.9 THz correspond to frequencies far away from the bandgap (see the corresponding position in Figure 3.16B). The results around the dislocation center show almost the same field distributions over the whole area and indicate bulk modes. The image for $f = 96.7$ THz (localized mode) shows a region far off the dislocation (outside the area measured in Figure 3.16), also showing homogenous field distribution on the pillars, indicating the absence of enhanced fields at these positions away from the dislocation center like the simulation.

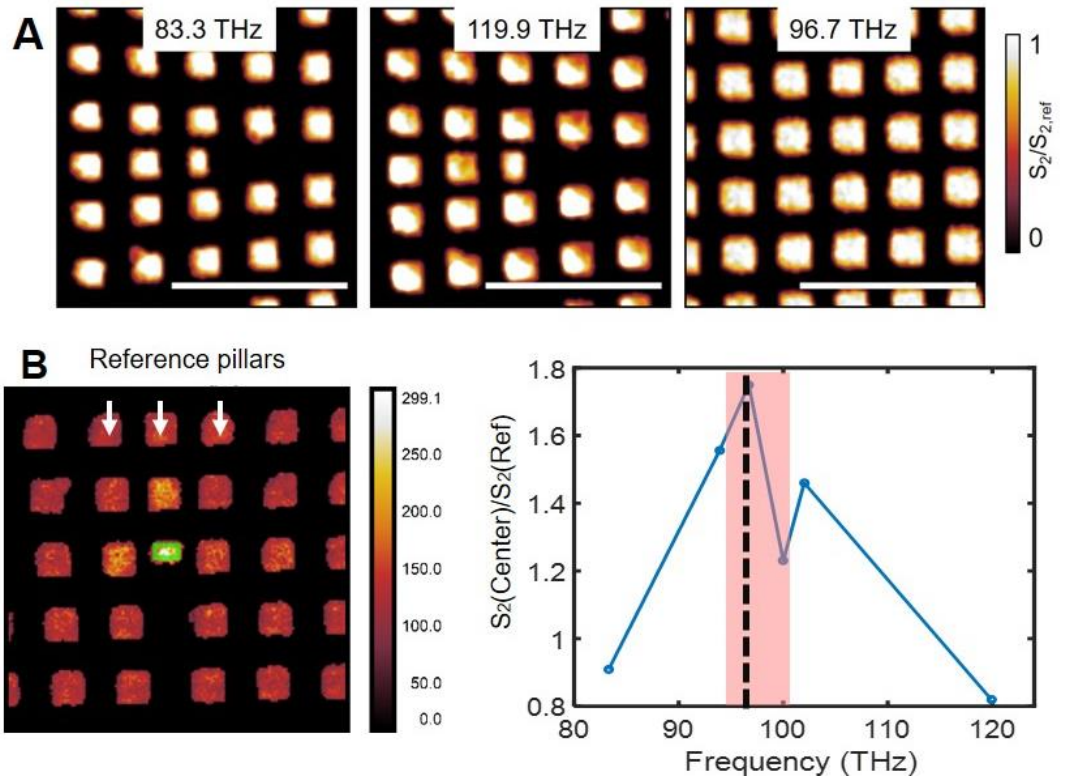

Figure 3.17 Several measurements from nonlocalized frequencies or positions, and the comparison of normalized S_2 signal. (A) Normalized S_2 amplitude images from measured results for nonlocalized frequencies or positions ($N = 4$). Right and left: Illustration of bulk modes for the two frequencies far away from the bandgap. Middle: The measured result off the dislocation center for the localized frequency at $f =$ 96.7 THz. The fields on the pillars are homogenous for all three images, indicating the absence of enhanced fields. (B) Normalized S_2 ratio between the pillar at the defect center and the reference region for different measurements. Left: A S_2 s-SNOM amplitude image shows the data normalization areas. The average s-SNOM amplitude signal on top of the pillar at the defect center (the green rectangle) is normalized to the data from the reference (as indicated by the white arrows). Right: Normalized amplitudes are plotted against different measured frequencies. Scale bars are 4 μm.

With the average S_2 s-SNOM amplitude signal on top of the pillar at the defect center (the green rectangle in Figure 3.17B), we further normalize the data of each measured frequency use the value from the three pillars as indicated by white arrows (the three pillars two rows above the green rectangle). The highest observed amplitude corresponds to the localized frequency can be found as marked out with the black dotted line in the right image of Figure 3.17B. While the normalized amplitudes at 100 THz (inside the bandgap without localization) and other frequencies are much lower compared to the localized frequency.

Further measuring of the light localization for different N is conducted in the same way, with the measured frequencies are determined by the simulation. All the results also provide similar results to the simulation, where a tight localization is observed on top of the single pillar at the dislocation center. In addition, the result shows a signal increment with an increase in

defect center extension (N), which is also consistent with the prediction from the simulation. Based on these results, the designed mid-bandgap localization and bulk states at optical frequencies could be demonstrated and verified by s-SNOM measurements, making it a promising tool to characterize TPhCs at optical frequencies even for structures at the nanoscale.

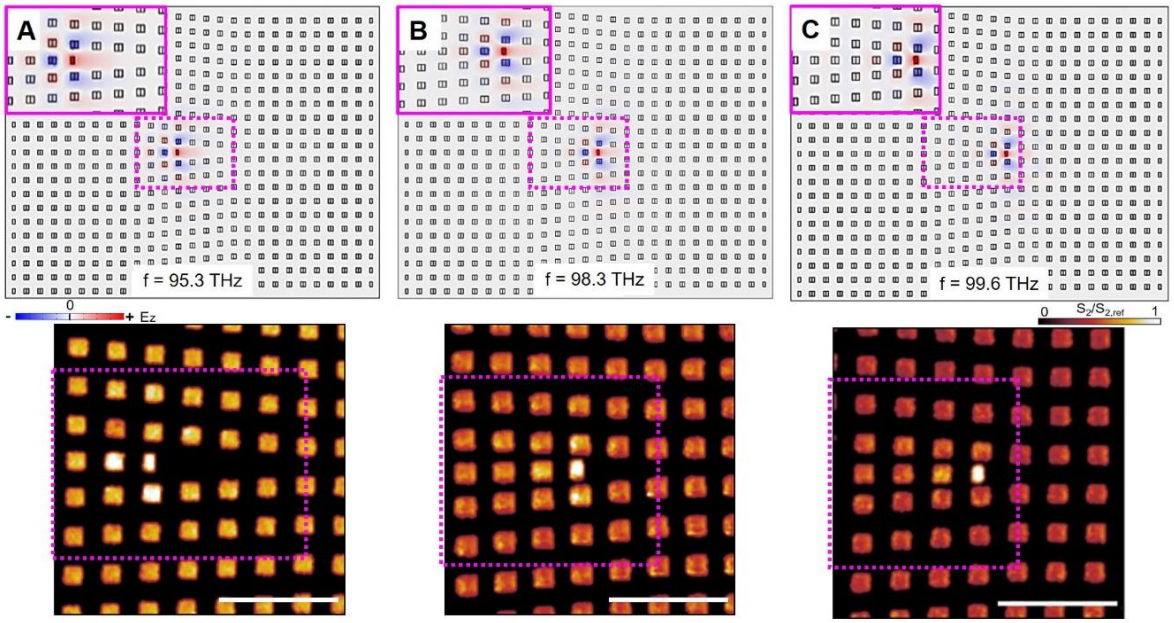

Figure 3.18 Versatility of the weak topological design. Demonstration of the versatility of the design to achieve the 0D localized mode with three different unit cell extensions at the dislocation center for (A) N = 3, (B) N = 5, and (C) N = 6, respectively. The left column shows the spectra, the middle column shows the simulated field distribution from the eigenmode solver, and the right column shows the normalized s-SNOM field distribution. Simulated and experimental field distributions show similar localization at the mid-bandgap (red dot in each spectrum) around the dislocation center. The localization becomes stronger with larger N. The dotted lines mark the area of the magnified inset in the simulation images, corresponding to the section shown in the measurements. Scale bars are 4 µm.

3.4 Conclusion and outlook

Confining light at optical frequencies to a point (0D) is promising for applications in nonlinear optics, quantum optics, and miniature active photonic device integration. Our study demonstrates a feasible strategy for accessing and tuning a topologically protected 0D localized state at infrared frequencies. The weak topology applied in our work enables a mid-bandgap 0D localized mode, which is present when the vector describing the nontrivial Zak phase is parallel to the Burgers vector of the edge dislocation according to the defined weak topological invariant. Furthermore, the designed optical localization with a subwavelength confined area is experimentally verified by s-SNOM measurements of a TPhC made of a-Si nanopillars placed on a layer of Cr. We also show that s-SNOM is a valuable tool for characterizing TPhCs with nanoscale resolution at optical frequencies. Based on the versatility of the weak topology,

similar in-bandgap 0D localizations with a confined field at the intentionally induced structural dislocation center, when designed with different dislocation extensions or columns to form the dislocation. Our study demonstrates a feasible strategy for accessing and tuning a topologically protected 0D localized state at infrared frequencies. With tighter nanopillars at the dislocation center, a reduced mode area is observed both in simulation and measurement.

Going further, as the TPhC is made of a-Si nanopillars placed on a layer of Cr, replacing the Cr with a phase-changing material (PCM) layer can be used to design active devices, as the switch on and off of the device designed with the localization can be realized easily as for the open and close of bandgap that is induced by PCM layer. Or the programmable PCM with a tunable refractive index could be included in the antennas of TPhCs to realize robust and active topological nanophotonics.[53, 101-103] Furthermore, the rapid progress of nanotechnology makes it possible to equip the defect center with quantum emitters, nanocrystals or molecules, which is highly promising for novel hybrid nanophotonic devices for single-photon generation in integrated optical circuits.[78, 104, 105]

4. TPhCs with QVH phase for integrated optical circuits

On-chip integrated photonic circuits are promising for realizing the final goal of all-optical information processing and computing. Recently, topologically protected light control in VPCs is verified to be useful for several complex functionalities, like topologically protected resonators and beam splitters. These important components realized by QVH phase would find more applications for photonic integrated circuits. In this chapter, we experimentally demonstrate topological light control at the nanoscale on an SOI platform. With the verified results obtained by classical light measurement, we seek to extend our design to quantum optical circuits, which is highly promising to obtain robust quantum integrated optical circuits, with photon generation, transfer, and interference in a single chip.

4.1 Prospects and recent progress of TPhCs in integrated quantum optical circuits

Communications based on quantum optics are presumed to transmit data faster and further, with the encoded information also being processed secretly, accurately, and quickly. Following this, quantum optics are gaining significant attention, especially for the realization of on-chip integrated photonic circuits for complex applications like all-optical information processing and computing. Normally, these complex optical circuits unavoidable need to transmit light signals between different functional components, which are mostly realized by waveguides or traditional photonic crystals. However, back reflection, especially in conventional photonic circuits with sharp bending corners remains an outstanding problem during light transmission. In addition, the designed modes for most functional parts are usually sensitive to defects or fabrication perturbations, which both limit further increment of the density of photonic circuits. In contrast to conventional photonic crystals, modes that are protected by topology are robust to these defects or disorders.[9, 24] For example, it has long been verified and observed that edge states from two topologically distinct regions in TPhCs are robust against local perturbations and immune to backscattering, which could lead to unexpected integrated photonic devices with robust light transport or interaction.[3, 16]

Recently, the QVH effect, which is a topological phase based on the development of valleytronics in condensed matter, is proved to provide a new degree of freedom similar to the QSH effect for realizing topologically protected transport in VPCs.[15, 36] It has been experimentally observed that topologically protected edge states can be conducted at the interface in a robust way between regions with different valley topologies. With these topological modes, robust light transmission at the nanoscale and high-quality (Q) factor resonators can be realized, which are highly promising for complex optical circuits with different functionalities. Furthermore, in contrast to most on-chip quantum interference with

relatively long traditional waveguides, the valley phase provides the possibility to obtain small area topological protected beam splitters, which are one of the most important fundamental components to realize on-chip photonic integrated circuits.[37, 46] Taking these advantages, the combination of topological edge states with QVH and quantum optics has given rise to potential applications for quantum communication, such as a topological quantum source, topological single quantum emitters, topological biphoton quantum states, and even topologically protected quantum interference.[4, 39, 106] However, although these topological quantum photonic devices may provide a manipulated platform for on-chip quantum information processing, barely any research has focused on either photon generation or interference with exotic photon sources, which are still far away from the real concept of integrated photonic circuits, especially the on-chip designs.[5, 39, 46, 106] The realization of both photon generation and transmission with topological photonics on a single chip, once is achieved, could bring rapid growth to the crossover between quantum optics and topological photonics.[47]

In this chapter, we exploit the valley phase to experimentally demonstrate topological light control at the nanoscale on an SOI platform. Based on the QVH phase, the VPCs designed by breaking the spatial symmetry of two holes in the rhombic unit cell are accessible for top-down fabrication by EBL. In this way, the opposite sign of the Berry curvature at the *K* and *K'* points are found, which gives rise to the nontrivial valley Chern numbers and leads to the confinement of counter-propagating edge states with opposing helicity at the interface. Taking advantage of these edge states with a valley degree of freedom, we designed and characterized a high *Q* factor resonator and beam splitter, to realize on-chip topologically protected integrated optical devices in a small area. The high *Q* factor resonator presented in this thesis is useful for photon generation and mode selection, while the beam splitter can separate photon pairs efficiently in a small area. These functional components designed with VPCs are further verified by characterizing the classical light behavior in them, which paves the way for our future work in integrated on-chip quantum circuits.

4.2 Design of the VPCs

4.2.1 Band structure analysis and valley Chern number

Our VPC is based on Si, with the rhombic unit cell including two air holes as shown in Figure 4.1A. For convenience, the band structure is calculated from COMSOL in the 2D model (the same for other simulations) with the Eigenmode solver. The effective refractive index of Si is set to $n_{eff} = 3.062$ based on previous research and our comparison with the 3D model. First, considering the case with equivalent diameter hole size, the band structure of the VPC for TE polarization is shown as the blue dots in Figure 4.1B, providing a Dirac cone at the *K* point (and equivalently at the *K'* for such unit cell) in the first BZ at the frequency of 197.6 THz due to the C_6 symmetry of the unit cell. Next, if we shrink the size of one hole and at the same time expand the other to break the spatial symmetry of the unit cell, results in the VPC with a bandgap as shown by the red dots. The presence of the bandgap is because the symmetry of the

photonic crystal is reduced to C_3. Here, to optimize the working wavelength around 1550 nm in our design, the lattice constant a = 385 nm, air hole sizes of 190 nm, and 100 nm are used, which resulted in a bandgap from 189.5 THz to 206.8 THz (shaded with orange) as shown in Figure 4.1B.

In this design, the VPC can be approximatively described by an effective tight-binding Hamiltonian. Considering only the nearest-neighbor hopping, this Hamiltonian is written as

$$H = -t\sum_{i\in A}\sum_{\delta}\left(a_i^{\dagger}b_{i+\delta} + b_{i+\delta}^{\dagger}a_i\right) + \Delta\sum_i\left(a_i^{\dagger}a_i + b_i^{\dagger}b\right) \tag{4.1}$$

where $a^{\dagger}$(a) is the creation (annihilation) operator on the corresponding sublattice.[15, 32] The first term in it describes the nearest-neighbor hopping, where the summation i runs over all the sublattices and the sum over δ is carried out over the nearest-neighbor vectors. The second term is the energy difference 2Δ between sublattices (the two different holes in our unit cell), which is determined by the spatial-inversion symmetry breaking. If we further diagonalize the above Hamiltonian and make an expansion of it near the *K/K'* points, it is reduced to the two-dimensional Dirac equation, and thus the band structure topology around *K/K'* can be understood by an effective massive Dirac Hamiltonian.

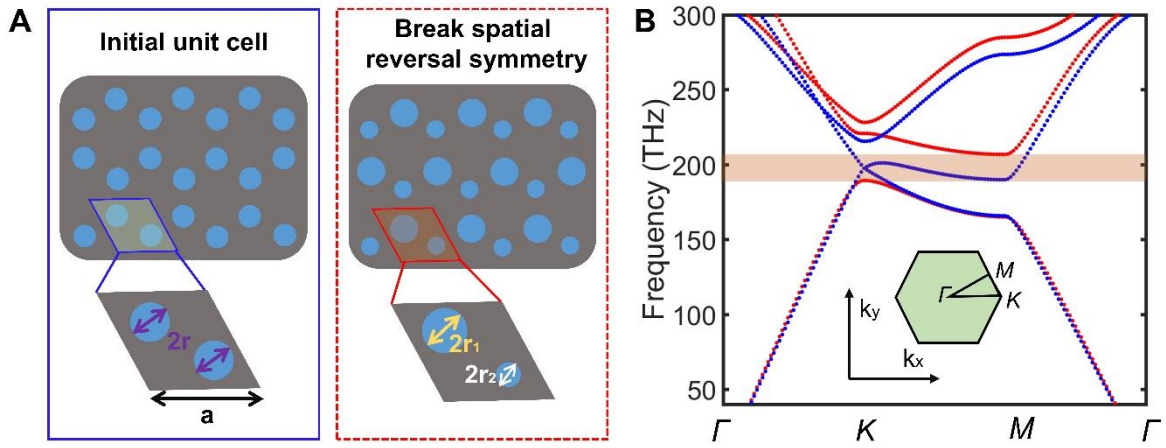

Figure 4.1 Unit cell illustration and band structure. (A) Schematic of the initial unit cell and perturbed rhombic lattice by breaking spatial reversal symmetry. The rhombic unit cell with Si comprises two circular holes with air. (B) Band structure for the initial unit cell (blue dots) and after breaking spatial reversal symmetry (red dots) unit. The effective refractive index for Si in our 2D simulation is 3.062. The inset shows the first Brillouin zone of the PhC. Dimensions information of the unit cell: a = 385 nm, $2r_1$ = 190 nm, and $2r_2$ = 100 nm. A bandgap from 189.5 THz to 206.8 THz is shaded with orange after breaking the spatial symmetry.

By dealing with Equation 4.1, the Hamiltonian for the *K* valley is

$$H_k = v\left(q_x\sigma_x + q_y\sigma_y\right) + \Delta\sigma_z \tag{4.2}$$

where $\sigma_z = \pm 1$ represent φ^+ and φ^- states, respectively. And the sign differences are a result of two opposite valley states as shown in the phase profile of VPC at the *K* point (the two images on the left of Figure 4.2).[15] $\vec{q} = (q_x, q_y)$ is the wavevector derivation from the *K* point, and Δ is an effective mass term determined by the bandgap size.[16, 32, 34] Correspondingly, around *K′* we have a different Hamiltonian with $H_{K'} = -H_K$, as guaranteed by the time-reversal symmetry in such a system. By calculating the integration of the Berry curvatures over the BZ, we can find that the Berry curvature at the *K* and *K'* points possess opposite signs, which gives rise to the valley Chern numbers of VPCs for $C_{K/K'} = \pm 1/2$. Therefore, the valley Chern number of the system composed of VPC1 and VPC2 (see the illustration in Figure 4.2) is $|C_{K/K'}| = 1$, resulting in two protected helical states in VPCs similar to the QSH phase.

To quantitatively analyze the topological transition of VPCs, we further simulate the evolution of the bandgap (at the *K* point as an example) of the VPC with the function of Δr ($\Delta r = r_1 - r_2$) as shown in Figure 4.2. It's easy to note that the sizes of the bandgaps grow with increasing Δr (the degree of spatial symmetry breaking) and the phase profiles for VPC1 and VPC2 are inversed, but with the same bandgap.

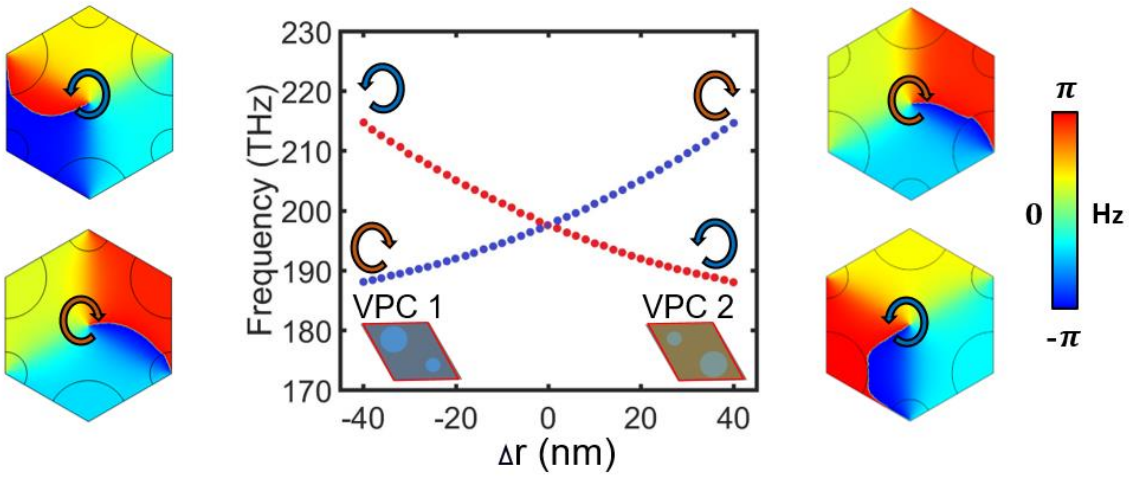

Figure 4.2 The evolution of bandgap for different hole sizes. The red (blue) dots represent anticlockwise and clockwise vortex, indicated by the arrows. H_z phase profile of VPCs with inverse symmetry at *K* point in the upper and lower bands. A bandgap closing and reopening are observed through the turning of hole sizes.

4.2.2 Kink states and robust light transmission

The nontrivial valley Chern number that we analyzed above can lead to a pair of counter-propagating edge states (or more exactly kink states) with opposing helicity at the interface with opposite inversion of the rhombic unit cells on each side of the VPC. Here, by putting the two kinds of unit cells (with opposite inversion) in a different way, we can realize several topological waveguides, providing a flexible design for light control. Two types of interfaces are numerically calculated as shown below. The first type is the zigzag interface (see Figure 4.3A), consisting of two large or small holes facing one another, with the band structure corresponding to the supercell along k_x obtained by COMSOL is shown in the center. The band

structure indicates that the propagating directions of the two topological kink states bounded to different valleys are exactly the opposite, exhibiting "valley-locked" chirality. The second type is a bearded interface (Figure 4.3B). The pair of kink states are also bounded to different valleys and propagate in opposite directions along with the interface as for the opposite sign of valley Chern number. However, in the two bearded interfaces, we can also find two trivial waveguide modes (as marked by green dots) corresponding to each design. As either gradually changes the size of the holes on one side of the interface can transform the bearded interfaces into zigzag interfaces, and the vanishing of them proves the trivial character of these green dotted modes.[39]

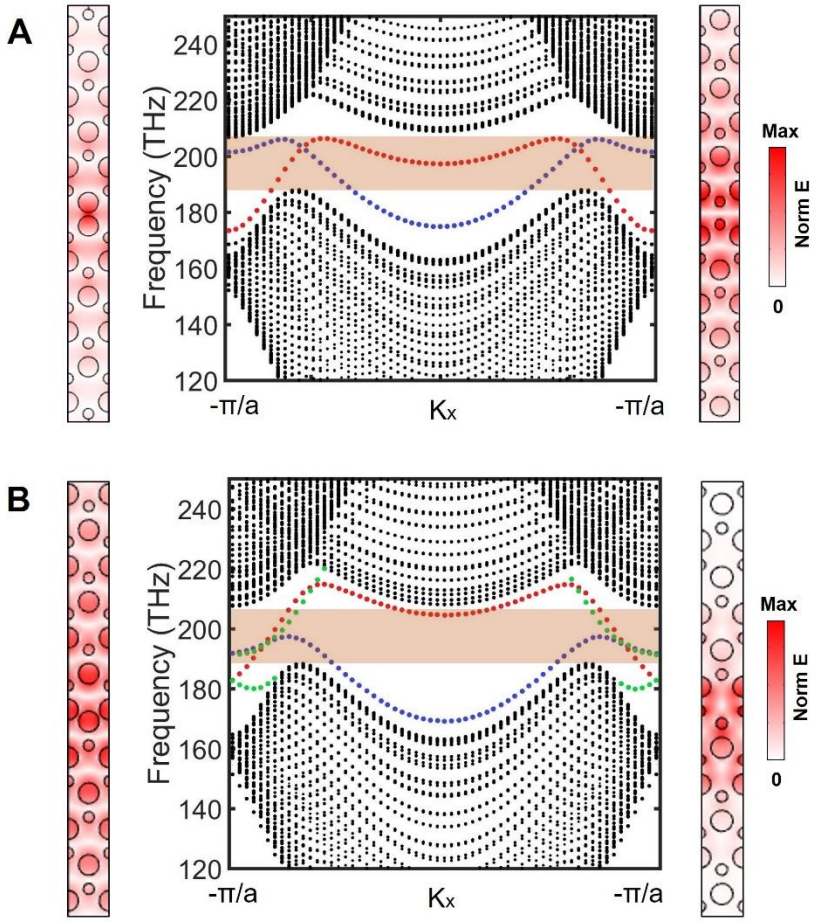

Figure 4.3 Two kinds of interfaces and valley-polarized topological kink states. (A) Zigzag interfaces are formed by VPCs with opposite hole sizes. (B) Bearded interfaces are formed by VPCs. Here, regions with lots of black dots are bulk bands, whereas red (blue) curves represent kink states. Parts of the supercell (including the electrical field distribution) for calculating these kink states are shown on each side.

Furthermore, it is well-known that conventional photonic crystal waveguides suffer from considerable reflection loss when electromagnetic waves propagate through sharp bending corners. However, the design with VPCs can solve this problem and reduce the energy loss within the devices due to the so-called topological protection. By simulating and comparing

the normalized transmission for two topological waveguides around 11 μm long with and without bending, unity transmission across some frequencies inside the bandgap is observed from both waveguides as shown in Figure 4.4. This provides direct evidence of the topological protection engaged to the modes within the bandgap. Furthermore, the low loss taken by transmitting light through sharp bends can also provide more flexibility to the design of different kinds of compact photonic integrated circuits.

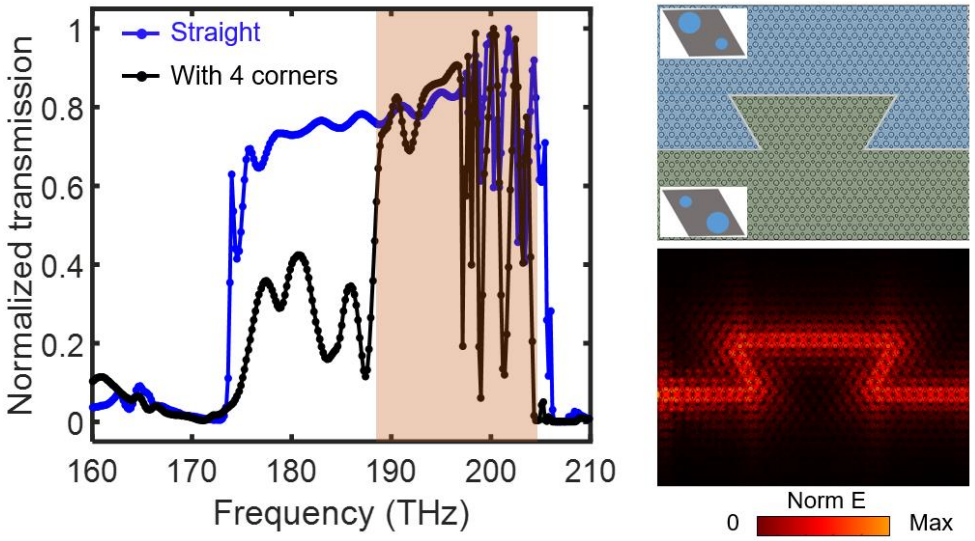

Figure 4.4 Demonstration of robust transportation of valley kink states through sharp bending paths. Top right: Schematic of a waveguide containing four sharp bends. Regions of opposite unit cell orientation are shaded with a different color. Bottom right: Simulated electric field intensity for the topological waveguide with bending (1550 nm), when light is injected from the left. Left: Normalized transmission through the waveguide with four sharp bends and comparison with the same type of straight topological of the same length. The transmission for both waveguides is similar at a certain range inside the bandgap as shaded by orange.

4.2.3 Resonator and beam splitter design based on VPCs

Taking advantage of the valley degree of freedom and the robust protection to light transmission, the unit cells analyzed above can further be used to construct more complex on-chip optical circuits, i.e., the drop-off resonator and beam splitter in this part. The resonator can provide an enhanced light-matter interaction, which is useful for possible applications like mode selection and active devices. Here, our resonator takes the form of a triangle by embedding a triangular array of unit cells inside with inverted hole sizes as shown in Figure 4.5. For the resonator side width with 15 unit cells, the mode spectrum of the resonator calculated from the simulation is shown and reveals a transmission maximum at Port 3 (or a minimum at Port 2) corresponding to the resonating wavelength at ~1510 nm. The simulated resonator mode inside the bandgap also shows a Q factor larger than 9000 obtained from the intensity dropping from Port 3 in this case. In addition, the VPCs can also provide more design layouts (like rhombic and honeycomb shapes) based on the calculated edge states (4 types)

from the previous part, which are especially useful for the design of more complex optical circuits.

With this design, a mode selection of the resonator can be easily realized by editing the edge state for Port 3 to generate relative pure photons. On the other hand, a higher *Q* factor is also possible by further tuning the design layout.

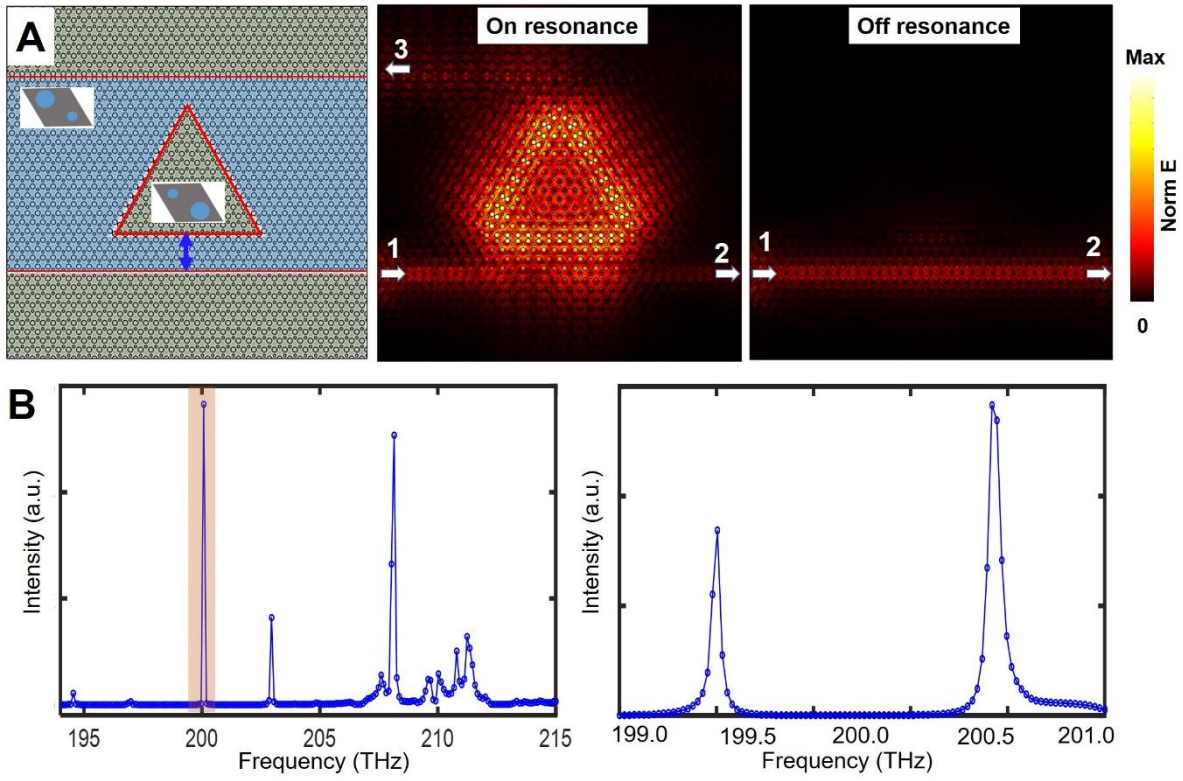

Figure 4.5 Cavity design and characterization. (A) Design layout of the resonator, the two unit cells are covered with different false colors. The electric field distribution of the resonator for on and off-resonance are shown on the right. The side length of the resonator includes 15 unit cells. (B) Spectra of the resonator integrated from Port 3 by excitation from Port 1. A Q factor large than 9000 is obtained by comparing the half-intensity dropping from the maximum.

Further, based on the valley kink states with different combinations, we can also realize topologically protected beam splitters, where light transport paths are determined by the geometries of the intersections. The most promising one is based on the channel intersection that consists of zigzag interfaces (Figure 4.6A), with the light flow is marked by red and blue arrows for different valleys. In these channels, light travel only along the paths of the same valley degree of freedom, for example, emission from Port 1 (Port 2) can only transport to Port 3 and Port 4 and are forbidden to travel to Port 2 (Port 1). This is determined by the kink states bounded to valleys that cannot couple to the states that have different valley pseudo-spins. On the other hand, the transmission for Port 3 and 4 is almost the same either by sending photons from Port 1 or 2 as shown in Figure 4.6B.

As one of the most important fundamental components for integrated optical circuits, a beam splitter that can protect at the photon level is important for quantum information processing. Here, COMSOL provides an easy way through boundary mode analysis to get the S-parameter for different input/output ports by adding waveguides (we use single-mode as shown in Appendix Part C) together, we can evaluate the Hong-Ou-Mandel interference efficiency with the S-parameter from simulation as analyzed below.

Based on the designed topological beam splitter, we can express the creation operators of the four channels in such a design (two input states and two output states) with the creation operators of the four different S-parameters for the incoming quantum state.

$$\hat{a}_1^\dagger = \hat{a}_{1,in}^\dagger$$

$$\hat{a}_2^\dagger = \hat{a}_{2,in}^\dagger$$

$$\hat{a}_3^\dagger = \hat{a}_{3,out}^\dagger = \mathrm{S}_{23}\hat{a}_{2,in}^\dagger + \mathrm{S}_{13}\hat{a}_{1,in}^\dagger$$

$$\hat{a}_4^\dagger = \hat{a}_{4,out}^\dagger = \mathrm{S}_{24}\hat{a}_{2,in}^\dagger + \mathrm{S}_{14}\hat{a}_{1,in}^\dagger \tag{4.3}$$

Here, the indices of the creation operators correspond to the port numbers. When two photons enter the beam splitter, one on each side, we can derive an expression for the quantum state after the beam splitter.

$$|1,1\rangle_{in} = \hat{a}_1^\dagger\hat{a}_2^\dagger|0,0\rangle = \left(\mathrm{S}_{13}\hat{a}_{1,in}^\dagger + \mathrm{S}_{14}\hat{a}_{1,in}^\dagger\right)\left(\mathrm{S}_{23}\hat{a}_{2,in}^\dagger + \mathrm{S}_{24}\hat{a}_{2,in}^\dagger\right)|0,0\rangle \tag{4.4}$$

As the S-parameters in such design always guarantee $S_{23} = S_{43}$ and $S_{21} = -S_{41}$ (or $S_{23} = -S_{43}$ and $S_{21} = S_{41}$) by such valley design, ideal quantum interference can always be observed inside the bandgap. In a recent publication, a measured quantum interference efficiency of more than 0.95 is realized with similar VPCs.[46] This means the VPCs are highly promising for quantum information processing due to the predominant interference efficiency on a small scale. In addition, it is also possible to realize beam splitters with other design layouts and more complex quantum circuits are available for such freedom provided by the valley phase.

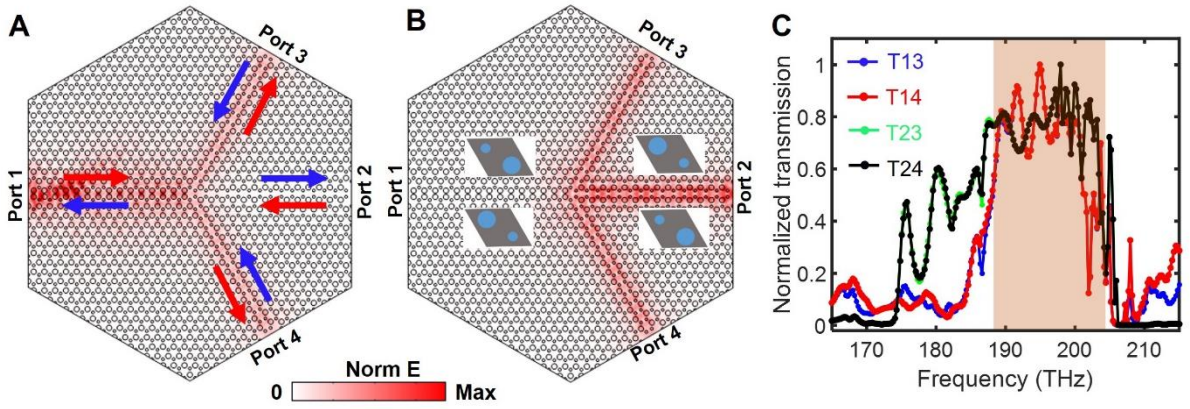

Figure 4.6 Layout of the beam splitter and normalized light separating efficiency and electric field distribution for different ports. (A) Valley-dependent topological beam splitter. Photons are coupled into the right (Port 1) or left (Port 2) port at the *K* valley, then the propagating photons at the junction will couple into Port 3 and 4, while the coupling to Port 2 or 1 is suppressed. (C) The transmission spectral from different ports are plotted. The red or blue arrows in (A) illustrate either *K* or *K'* coupling channels. T13 is the transmission from Port 1 to Port 3, the same for other labels in (C).

4.3 Characterization of the on-chip light control with VPCs.

To verify the design and characterize the performance of the VPCs above, the topological beam splitter in Figure 4.6 is fabricated together with single-mode waveguides and gratings on an SOI substrate. As shown in Figure 4.7, the joint structure includes gratings for coupling in and out by connecting each port of topological structures with single-mode waveguides. We select partly gratings through a two-step fabrication processing to get a relatively higher coupling efficiency. This part will focus on the fabrication and characterization of the topological beam splitter designed by VPCs.

4.3.1 Sample fabrication

Besides the general introduction for the fabrication of Si nanophotonics in Chapter 2. We also provide in this section the specific steps and challenges in the fabrication of this sample. The sample fabrication includes a two-layer EBL process, with one layer for the VPCs and waveguides, and the other corresponding to the partly etched grating for higher coupling efficiency.

For the multilayer fabrication process, precise overlay lithography processes are extremely important. Because the used lithography system divides the pattern into several writing fields (for example, the topological structures with grating here are divided into three writing fields), the writing fields' alignment with the local markers from the system is firstly performed in this case. In addition, we also need to place several layers of nanostructures we want to fabricate at desired positions with high accuracy in overlay lithography. Typically, we can use the local markers sitting at the corners of the whole writing field from a patterning list

as illustrated in Figure 4.7. Then, realignment of the lithography coordinate based on the four global markers is performed in overlay lithography. The perfect alignment should find the exact position of all the global markers during the patterning of every layer. Here, layer 1 contains a patterning area for the local markers, VPCs, and waveguides, which are fabricated in the first fabrication step. After finishing the lithography and other processes depending on the structural design. The four global markers can then be scanned to align layer 2 on top of layer 1 with SEM images, as the gratings have to be fabricated on top of the taper. Typically, alignment accuracies of about ±20 nm can be realized. The mismatches are neglectable due to their small influence on the coupling efficiency

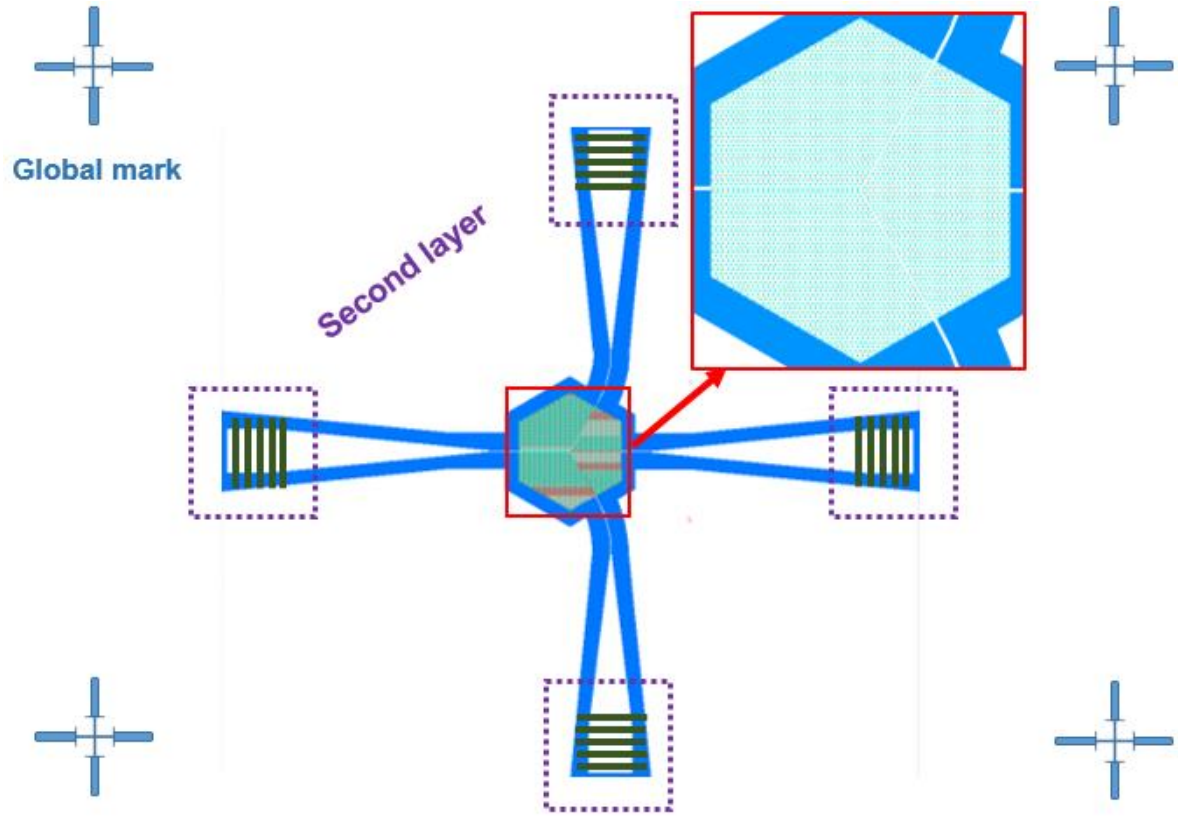

Figure 4.7 Illustration of the layout for patterning. In the first layer, the global mark, VPCs, and waveguides are fabricated. Different colors in the figure show the different doses for exposure (white are corresponding to the blank area). In the second layer, the gratings on the taper are fabricated after a precise write field alignment with the four global marks (after etching and Cr removing as explained later).

For the VPCs and waveguides fabrication, the EBL process is based on a layer of negative resist. First, the SOI sample was cleaned by ultrasonic in acetone, deionized water, and isopropanol mixed solution and heated in an oven at 190 °C for 30 mins to remove the desorption of water molecules adsorbed on surfaces exposed to air humidity and the -OH bonds present on oxidized Si surfaces. This step is important for the adhesion between the resist and SOI substrate in our fabrication as for the small size of the design. A negative resist (ma-N2403, Micro Resist Technology) layer with a thickness of around 200 nm was spin-coated onto the SOI sample and baked on a hot plate at 90 °C for 60 s to remove the solvent. The desired

structures were then patterned by using a standard EBL and developed in ma-D525 solution (Micro Resist Technology) for 43 s. The developing process was then stopped in deionized water for 60 s and dried with N_2 gas carefully. Next, a 20 nm thick Cr mask was deposited by electron beam evaporation. After a lift-off process in hot acetone, the patterns were transferred from the resist mask to Cr. Finally, the VPCs and waveguides were transferred onto Si using an ICP-RIE process.

For the grating fabrication, the EBL process is based on a layer of PMMA after a precise writing-field alignment introduced above. After ICP-RIE etching from the previous step, the complete removal of the Cr mask by a commercially purchased Cr-etch solution was conducted. Then, a PMMA resist layer (around 600 nm by two steps spin coating) was spin-coated onto the sample and baked on a hot plate at 170 °C for 2 mins at each step to remove the solvent. This 600 nm resist layer can provide enough protection to other structures except grating as tested in Appendix Part D. The grating was then patterned by EBL at the exact positions with the above writing-field alignment and developed in AR 600-56 (Allresist GmbH). Finally, the grating was then obtained by ICP-RIE for 35 s and cleaning the remaining resist in acetone.

The whole fabrication process is also illustrated with SEM images and explanation as shown in Figure 4.8 below.

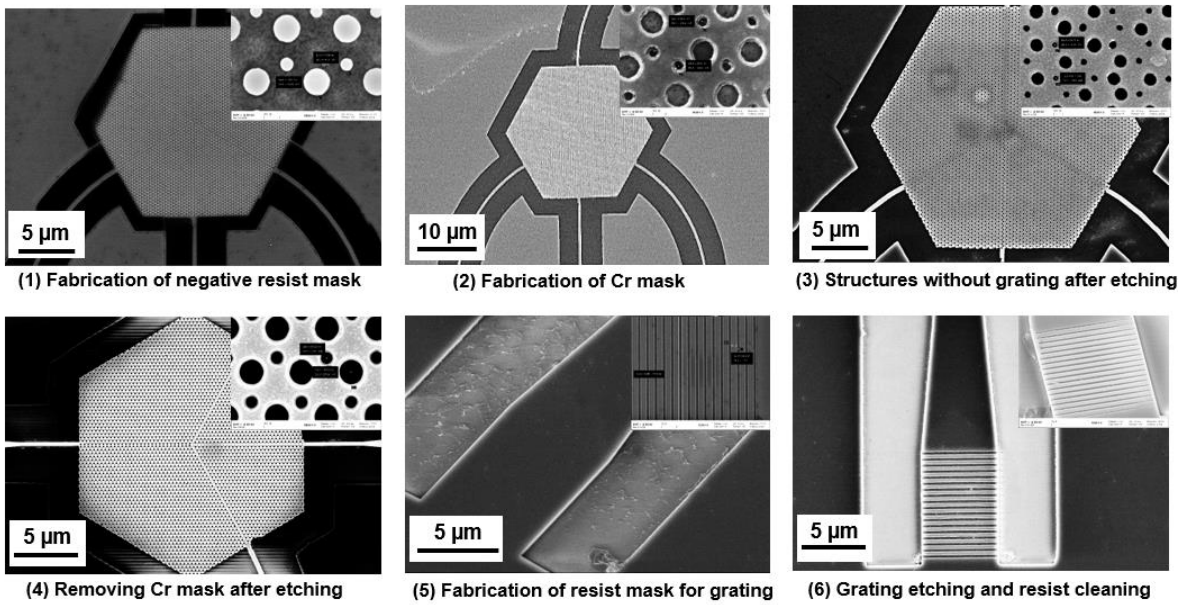

Figure 4.8 Understanding the sample fabrication with SEM images. The sample fabrication includes the following steps: (1) EBL with negative resist. Resist structures include VPCs, waveguides, and taper without grating are fabricated. (2) Getting Cr mask for etching. The Cr mask is fabricated by developing the patterned sample, deposition of Cr mask, and lifting-off. (3) Plasmon etching with Cr mask. (4) Cr mask removed. The Cr mask on the taper should be removed completely to ensure the successful fabrication of the grating mask in the following step. (5) EBL with positive resist. A good writing-field alignment of the system is conducted to fabricate the resist mask of the grating on the taper. (6) Grating etching with the resist as an etching mask and removing the remaining resist on the sample.

On the other hand, we should note here that due to memory requirements and time-consuming, the beam splitter and resonator above are calculated by 2D simulation. To go close to the real situation, the band structure determined from the 3D simulation is used to analyze the fabricated VPCs. The band structure from the 3D simulation uses the model corresponding to our material is shown in Figure 4.9A (where the thickness of the Si layer is 340 nm with a refractive index of 3.48), which results in a bandgap smaller than the 2D case. The hole size of 190 nm and 100 nm in such design resulted in a bandgap from 190.3 THz to 197.5 THz (vs 189.5 THz to 206.8 THz obtained from 2D simulation). However, this design still includes the 1550 nm wavelength at 192.9 THz that we are interested in. To reduce the influence of the fabrication process, which may change the bandgap size and relative frequencies, we perform a parameter sweep and plot the full band gap size as shown in Figure 4.9B. In the figure, the values of the parameters that either do not have a full band gap or the 192.9 THz frequency (the size change will influence the bandgap position) is not included inside the bandgap are plotted with black color (corresponding to zero full bandgaps in the figure). Compared with the measured size of the two holes after fabrication, the hole size of 190 nm and 100 nm in our design could guarantee relatively large fabrication tolerance, as the device will still work either in case of an increase or reduction of the hole sizes.

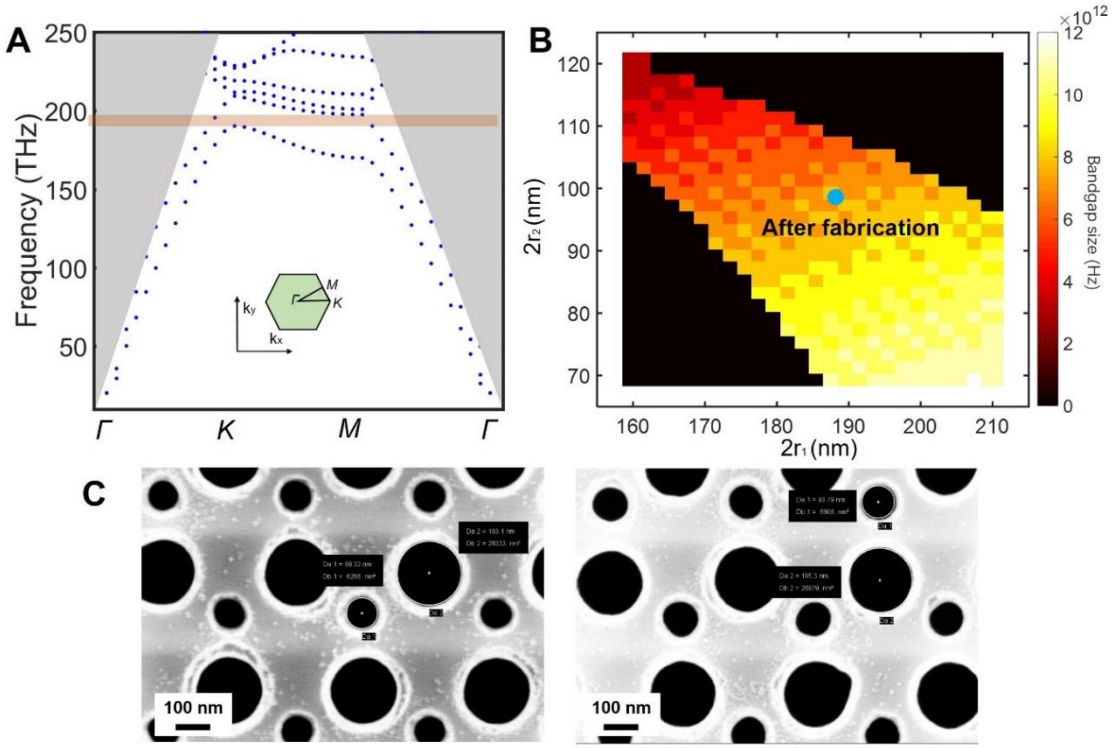

Figure 4.9 The corresponding band structure from 3D simulation and the full band gap for different hole sizes. (A) Band structure based on our SOI material with 340 nm Si layer. The corresponding band structure shows a full bandgap from 190.3 THz to 197.5 THz as shaded by orange color. (B) The full band gap size (with 1550 nm wavelength inside) for different hole sizes under the same lattice constant. According to the measured size after fabrication, the size tolerance should not influence the working mechanism of our devices. (C) SEM images of the VPCs were fabricated at different times. The size deviation is minimal.

4.3.2 Characterization of classical light transmission with VPCs

According to the VPCs simulated above, once a full bandgap is open, kink states can be observed as guaranteed by $|C_{K/K'}| = 1$ explained above. As the calculated kink states are below the light cone, which guarantees broadband topologically protected light propagation with out-of-plane confinement. With the fabrication from SOI material, we first measured the structure only with TE single-mode waveguide and gratings on the sample based on the setup shown in Figure 4.10. The measured light transmission efficiency for the layout without topological structures from both simulation and experiment can be found in Appendix Part D, which is further used to normalize the efficiency of the topological structures. Then, the light transmission inside the topological beam splitter is measured at several frequencies with a full structure including grating coupler, taper, and normal TE single-mode rectangle waveguides. As the efficiency from the single-mode waveguide and gratings is almost constant due to the same design and fabrication process, the highest efficiency of the topological beam splitter together with waveguides joint obtained by normalizing data to the normal TE single waveguides is 1% at 1520 nm (Port 1 in) and 5% at 1570 nm (Port 2 in) respectively. In the 3D simulation, the value is ~14% at 1520 nm (Port 1 in) and ~30% at 1570 nm (Port 2 in), which is consistent here as the loss at the waveguide joint area and inside the structures are relatively higher in the real case. Similar to the simulation performed in the previous part, the transmission efficiency for the three measured frequencies in the bandgap is almost the same as observed from the three measured frequencies in Figure 4.10B (input from either Port 1 or Port 2). While the transmission outside the bandgap is suppressed as there are no kink states for such wavelengths and in this case, most of the light is either absorbed or radiated by the structures.

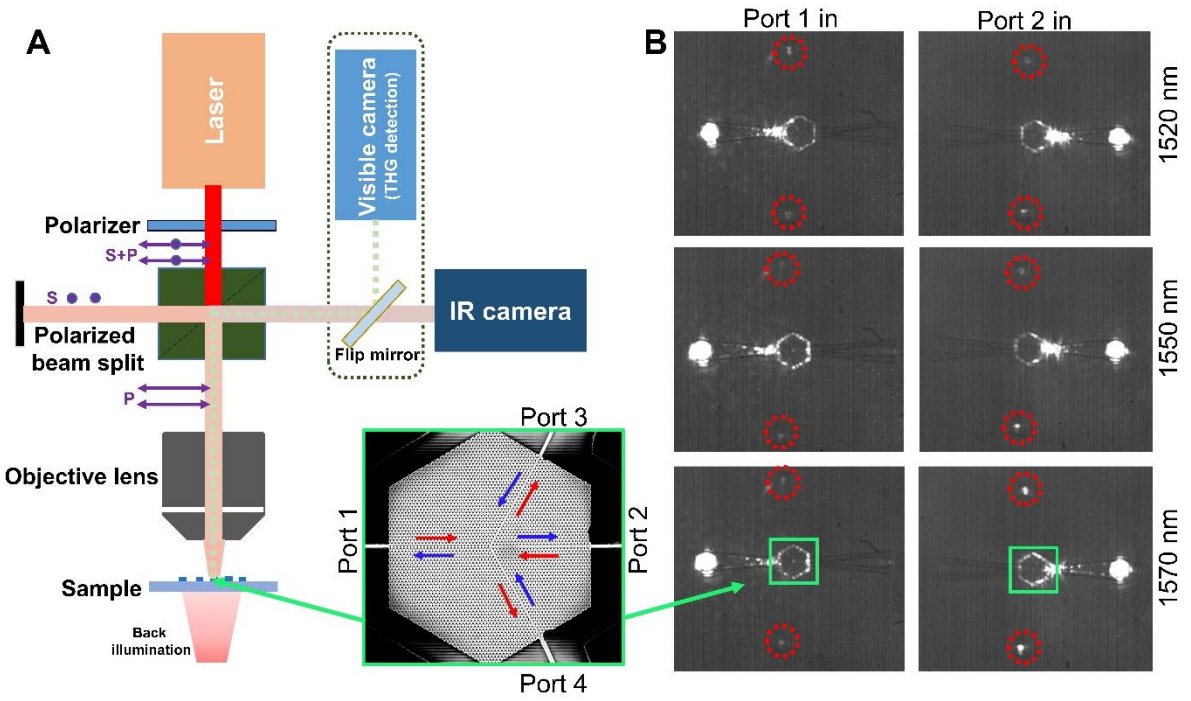

Figure 4.10 Setup for the measurement and light transmission with the topological beam splitter from two ports. (A) Setup for the measurement. With the polarized beam splitter, the output light can be measured from the output grating corresponding to Ports 3 and 4. While the back illumination of the sample with a white light source provides the possibility to locate the fabricated structures with an objective lens and IR camera. The flip mirror and the camera for visible wavelengths are used to further determine the light transmission inside the structure. (B) Measured transmission for the beam splitters at three wavelengths (1520 nm, 1550 nm, and 1570 nm) inside the bandgap. Light coupling-out from output grating corresponding to Port 3 and 4 was observed by input on either Port 1 or 2 as marked by the red dotted circles in the images. The efficiency is much lower when the input was done from Port 1, which is similar to our simulation. SEM images of the beam splitter and the corresponding position at the measured images are illustrated by green boxes.

4.3.3 Observing the kink states by THG

As Si's intrinsic three-order nonlinearity, it can provide a relatively efficient third-harmonic generation (THG) signal. For example, if one illuminates a Si sample with a short-pulse laser beam at a fundamental wavelength of 1590 nm, the third harmonic at 530 nm can be detected from the sample. This nonlinear imaging method has been proved to provide several advantages to characterize these topologically protected states as shown in one of the publications from our group.[88] Firstly, as the THG signal cannot be confined within the structure, it radiates freely to the far-field and can be detected easily. In addition, the THG signal in the far-field still follows the same near-field distribution from these topologically protected states, due to the dependence of the THG intensity on its linear counterpart. Secondly, due to the spectral separation of THG signal and fundamental wavelength, this method provides background-free information within the structures by filtering the fundamental pumped signal.

Lastly, a shorter wavelength always corresponds to a higher resolution.

To better see the light interaction inside the topological structures, the kink states are further characterized by THG measurement with ultra-short laser pulses. In our experiment, the sample was illuminated by the beam from an optical parametric oscillator (OPO) with a typical pulse length of 200 fs and a repetition rate of 80 MHz synchronously pumped by a TiSa femtosecond laser. In the same way, with the setup above, the THG signal of the structure was collected by flipping the mirror and reflecting the signal to the visible camera. In the recorded images in Figure 4.11, we marked out the beam splitter areas with blue dotted lines based on the different contrast provided by a weak illumination light. In addition, the THG signal generated from the relatively blighted white area can be recorded. These areas that can provide THG signal are either strong scattering happens (joint area between the waveguide and the topological structures in the top row) or topological edge states areas (the straight edge connected to the input port in the bottom row) due to the light-matter interaction. The observed THG signal distribution is similar to the field simulation as shown in the top row of Figure 4.11. As the waveguide and VPCs joint area show the strongest field distribution due to the mode mismatch between the waveguide mode and topological waveguide mode like the simulation. A strong THG signal from this area can be detected when the beam is inputted from Port 1. While the kink state in the VPCs when inputting from Port 1 cannot be observed by the THG signal, which may be caused by the relatively lower energy flow inside the structures and broader field distribution. On the other hand, When the beam is inputted from Port 2, the kink state from THG inside the topological beam splitter along this port similar to the simulation with a tight field distribution is observed. The THG signal here also verifies that the bandgap is around the wavelength of 1570 nm, as the signal becomes relatively weak due to the scattering into the bulk outside the bandgap. But after separating the two kink states connects to Port 3 and 4, no similar signal can be detected anymore, which is a high possibility for the power separation that makes it difficult to observe signals (as 2 times fundamental intensity corresponding to 8 times of THG signal). Overall, the THG measurement provides more details inside the topological structures as expected and the results correspond to our simulation to some extent.

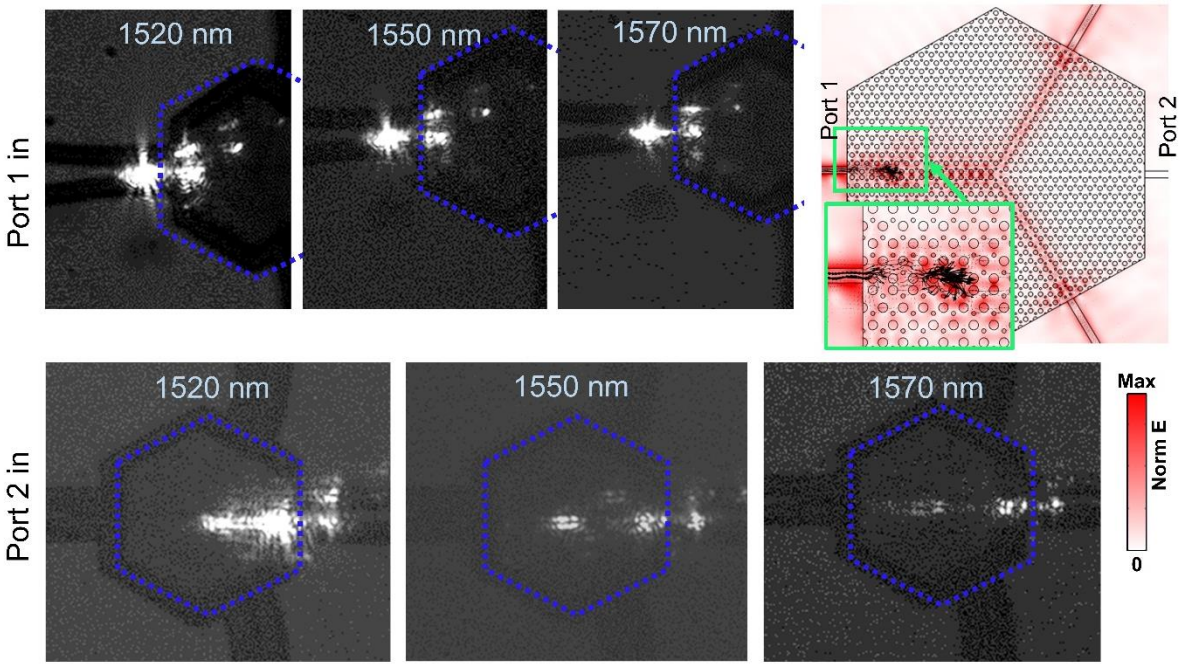

Figure 4.11 THG measurement with the designed beam splitter. Kink states similar to the ones obtained in the simulation are observed when the beam is inputted from Port 2. The kink states in the VPCs after separating the two channels are not observed, which is highly possible to be explained due to the lower power. Most of the THG signal comes from the waveguide and the VPCs joint area when the beam is inputted from Port 1. This is because of the mode mismatch between the waveguide mode and topological waveguide mode. This behavior is also similar to our simulation, where field intensity is stronger in the joint area (the black arrows show the Poynting vectors, which illustrate the flow of energy). The kink state in the VPCs when inputting from this port cannot be observed with the THG signal, which may be caused by the lower intensity from the waveguide and relative broader field distribution. The blue dotted line marks the beam splitter area in the images.

4.4 Conclusion and outlook

Based on the topological valley kink states, we investigate the application for on-chip optical light control by simulation and experiment. Such valley kink states are robust against sharp bends, as guaranteed by the valley Chern number. In addition, VPCs can also be used to design resonators, which provide an enhanced light-matter interaction and may be useful for applications like mode selection and active devices. Furthermore, based on the valley kink states at generic interfaces, we can realize topological beam splitter intersections where the photonic transport paths are related to the geometries of the intersections.

All the necessary parts of integrated optical circuits from photon generation, low loss transmission, and interference are possible to realize with VPCs, as we verified and also based on recent research. The present design provides a possibility for a complete topological waveguide circuit, including photon source, transmission, and interference part, to be fabricated and integrated on the same substrate using the standard EBL process, which is

promising for all-optical signal processing in the future.

Our next goal of this project is to selectively generate photon pairs by a down-conversion process through the topological resonator and the photons are then used for on-chip quantum interference with topological waveguides directly. To realize this, the photon generation process with a topological resonator should be investigated more if one wants to efficiently get high-quality photons. In addition, the transmit efficiency between the normal waveguides and topological structures should be improved, or more creative designs should be considered to transport photons with topological waveguides barely. However, due to the limited time and equipment problems during my PhD study, not all of my designs are verified, and these remaining parts will be further extended by the following students.

5. A Si metasurface enabling both self-cleaning and dynamic color response

Another form of Si nanophotonics that is important for the minimization of optical systems is based on the well-known metasurfaces, which are artificial planar interfaces that consist of some nanostructured periodic or aperiodic arrays with carefully designed metallic or dielectric building blocks.[48, 57] Recently, the development of metasurfaces not only requires much more optical functionalities to replace some bulk components but also to seek more other abilities that are useful for real applications.[58, 60, 62, 65, 69, 71] In this chapter, we will investigate a Si metasurface, and show how its wettability design on it can be used to achieve self-cleaning ability and better optical performance with a dynamic color response.

5.1 Some recent achievements of metasurfaces with wettability design

Just like our introduction in Chapter 2, metasurfaces employ especially distributed nanoantennas to tailor light with desired amplitude, phase, and polarization. Their working principle is different from conventional optical components based on light propagation and refraction in bulk materials. Despite the broad range of functionality already achieved such as structural color, metaholograms, and metalenses we introduced, there are still some challenges, i.e., structure protection from dust contamination (or physical stability) and application in liquid environments, which may limit their real application.[67, 71, 72] It's easy to understand that dust on the metasurface always influences the optical performance directly, and cleaning them is a challenge due to the fragile of nanoantennas. For example, normal cleaning with ultrasonic could destroy the nanostructures, or cleaning with gases or water barely is not thoroughly. Fortunately, the self-cleaning process that is inspired by superhydrophobic plant leaves in nature may provide solutions to clean the dust on metasurfaces, as dust on such surfaces can be washed away easily only with water. On the other hand, the application of metasurfaces in liquid environments needs to consider the perfect matching between the nanoantennas and solution.

Similar to metasurfaces in some aspects, surfaces with superwettability comprising micro/nanosized structures usually show better physical stability compared to their optical counterpart due to the complex environments used with superwettability surfaces.[107, 108] Normally, superwettability refers to a superhydrophilic surface determined by a water droplet contact angle (CA) < 10° or a superhydrophobic surface with CA > 150°. Realizing a superhydrophilic surface is helpful to spread a liquid droplet uniformly and match with the structures on the surface perfectly. While a superhydrophobic surface is always robust and keeps its physical stability in a variety of harsh environments. Lots of applications like surface

self-cleaning only by rinsing with water, anti-fog/corrosion can be realized.[73, 107-109]

Although the superwettability and optical metasurfaces seem to be two research fields that are quite far away from each other, there is still some connection between them as both require well-designed surface micro/nanosized structures. Recently, some published seminal works also show several advantages to combining the devices' optical performance with the wettability design.[110-113] Standing out among them, ultrafast humidity-responsive structural color was realized by taking advantage of hydrophilic nanoporous TiO_2 as shown in Figure 5.1A. A self-cleaning antireflective surface was shown with random nanopillars resulting in the superhydrophobic state, which is based on the well-known lotus leaf effect to effectively roll off the water droplet and contamination as shown in Figure 5.1B.[114] A water-selective metasurface with hydrophilic/hydrophobic parts is used to actively modulate and steer the reflected light between the two states of wetting and drying, which shows the possibility to enrich the functionality. Insights of successfully including wettability designs in optical devices could improve the optical performance of metasurfaces (although most of them are based on randomly distributed structures), and at the same time equip them with smart self-cleaning or more functionalities. However, the wettability of a surface is typically expressed along with a large area of rougher micro/nanostructures, with structural requirements that are in stark contrast to the design of optical metasurfaces.[115] This makes the achievement of superwettability on the intentionally arranged nanoantennas challenging and raises the question: Is it possible to realize desired wettability on optical metasurfaces regardless of the small area and specific antenna distribution? Will it provide us with another strategy to achieve better optical performance or more functionalities for metasurfaces?

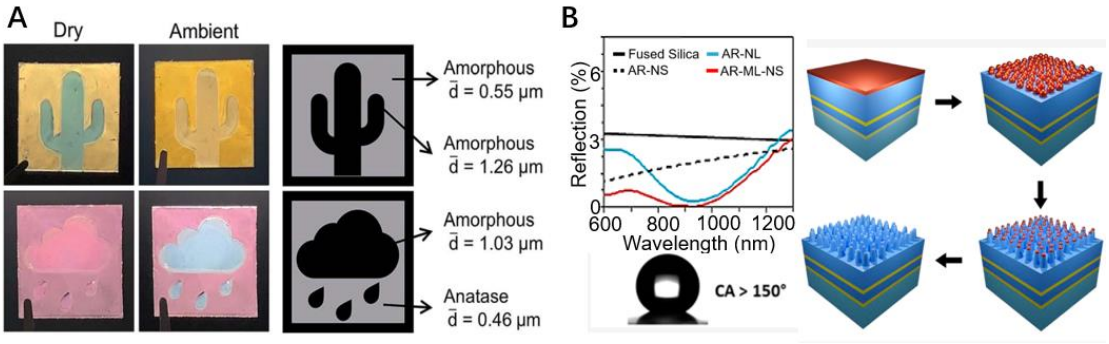

Figure 5.1 Metasurfaces with wettability design are applied to improve the optical performance or equip them with more functionalities. (A) The surface with structural color is designed to achieve ultrafast humidity-responsive. Based on the change of refractive index of background, the designed supperhydropilic surface show ultrafast response to humidity as the small water droplet can spread extremely fast on it. (B) A self-cleaning antireflective surface was shown with random nanopillars resulting superhydrophobic state. The surface shows both low antireflective (red curve) and good superhydrophobic (CA > 150°) performance. The self-cleaning process can be achieved as water droplets easily roll off from the surface and can take away the dust contamination, similar to the process on a lotus leaf. Figures are taken from Ref. 111 and 114 respectively.

5.2 Design of metasurfaces with superwettability and obvious optical response

For structural color applications, metasurfaces with a dynamic optical response or color change can be efficiently achieved by changing the refractive index that surrounds the antennas.[66, 74] These properties make them suitable candidates to directly investigate the optical and self-cleaning performance of the metasurfaces as both cleaning and optical response can be easily observed by checking the structural color of the metasurface under a microscope. In our work, we design a structural color metasurface to achieve two superwettability states by proper treatments and supporting structures design surrounding the metasurface area. These wettability states with an efficient color response or self-cleaning ability can be easily switched between each other, and no obvious degradation of the optical performance is observed during several repeatability tests, providing an efficient way to equip metasurfaces with more functionalities and better optical performance.

The designed metasurface is based on a-Si antennas with superhydrophilic and quasi-superhydrophobic states, which can be easily switched between each other by the introduced hydrophilic or hydrophobic treatment. Each wettability state is linked with a unique functionality as shown in Figure 5.2. The quasi-superhydrophobic state (CA > 130°): The large CA causes the droplets on the surface to easily slide off, which can be used to efficiently self-clean the tiny particles on the metasurface without destroying the nanoantennas. The superhydrophilic state (CA < 10°): A water droplet on the surface spreads very fast and efficiently forms a flat-water film that perfectly immerses the antennas inside.[111, 116, 117] This superhydrophilic state provides the possibility to design a metasurface with a dynamic color response (due to the change of surrounding environment), which is further improved due to the spreading behavior of water. More importantly, since the wettability of a surface is determined by the surface roughness and free energy together, it is possible to achieve a wettability transition between different states, just by modifying the surface free energy while keeping the surface structures unchanged.[118, 119] We should note here, that the possibility to achieve a wettability transition on the metasurface is important here, which would guarantee the realization of more functionalities.

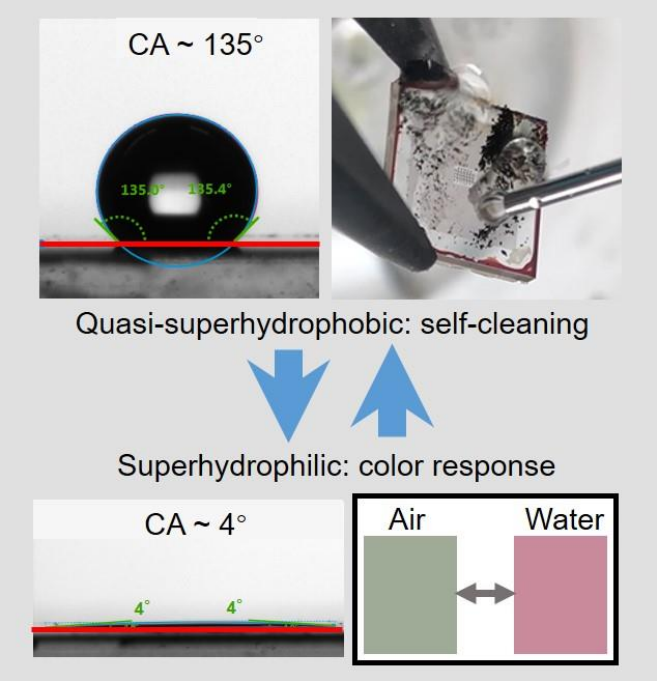

Figure 5.2 Illustration of functionality and wettability transition. Two superwettability states can be switched to each other repeatably with proper wettability treatment, each state is linked with a unique performance of the metasurface. The quasi-superhydrophobic state (CA ~ 135°) can be used to self-clean the dust contamination on the metasurface, the superhydrophilic state (CA ~ 4°) can be used to show the color change efficiently with water due to the fast spread of water droplet on the surface.

5.2.1 Selection of antennas for the metasurface and design criteria for supporting structures

To show our design strategy better, the rigorous coupled-wave analysis (RCWA, more details can be found in Appendix Part E) is used to optimize three unit cells for the metasurface with a large size difference, which perform notable color changes after changing the environment from air to water. The large size differences are used to mimic most metasurfaces designs, as different unit cells are frequently combined into one single design. The height of the a-Si antenna is H = 700 nm, which can be used to design metasurfaces with other optical functionalities, like metalenses and holograms above. Square unit cells with a constant period of P = 800 nm and square antennas with sizes of 260 nm, 410 nm and 560 nm on an Indium tin oxide (ITO) coated substrate are chosen based on the simulation. The ITO substrate here provides better conditions to check the structures on the sample in an SEM.

Here, the simulated spectra are calculated at normal incidence, as this case includes most of the reflected energy that is responsible for the observed color. Then the color determined by each reflective spectrum is used to plot the data. It's important to note that, the reflection spectrum of the 260 nm antenna (Figure 5.3A) is quite weak compared to the other two sizes we selected here (especially in the range of 450 - 600 nm which is responsible for the visible color reception), we use two colors that are close to the measured results to show the data. For

the 410 nm size antennas (Figure 5.3B), two obvious peaks around 500 - 550 nm and 650 - 700 nm are present in the air, resulting in the observed green color; while the relative peak intensity around 500 - 550 nm drops a lot in the water, with the other peak at long wavelength range shifts to around 650 nm. The spectral difference in air and water causes the observed green-red color change. For the 560 nm size antennas (Figure 5.3C), two peaks around 650 nm and 700 nm are present both in air and water, and an intensity drop for both of them is observed in water. The slight peak shift does not change the color in air and water, while the larger color difference observed in experiments could be linked with the drop of the intensity in water.

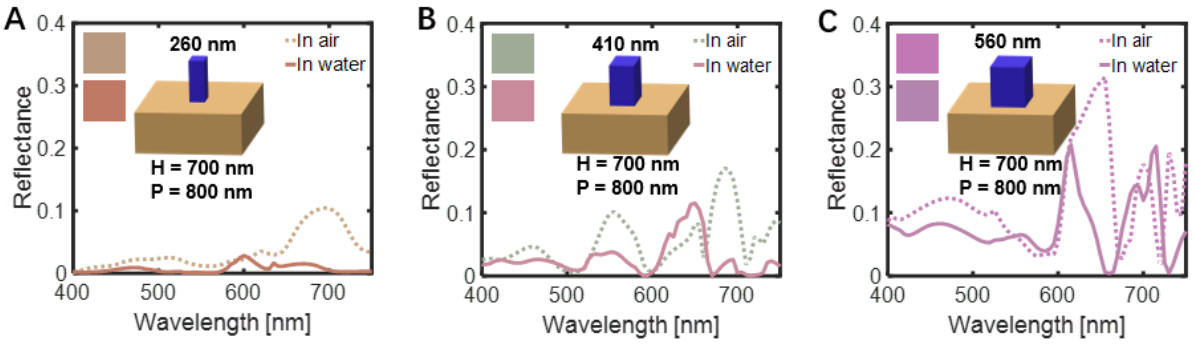

Figure 5.3 Reflective spectra from simulations for uniform arrays with three antenna sizes in air or water. (A) 260 nm, (B) 410 nm, (**C**) 560 nm. The corresponding RGB color (except result in A) of each spectrum is used to plot the data. The obvious color change from air to water provides the possibility to observe the optical response of the metasurface directly.

The color of the spectra is determined in the following way: according to the CIE color-matching functions, $\bar{x}(\lambda)$, $\bar{y}(\lambda)$ and $\bar{z}(\lambda)$, the chromatic response of an observer from a power spectrum of wavelengths, R(λ), can be mapped by a set of tristimulus values, x, y, and z. This set of tristimulus values is analog to the actual response of the three types of cone cells in the human eye.

$$\begin{aligned} X &= \int R(\lambda)\bar{x}(\lambda)d\lambda, \\ Y &= \int R(\lambda)\bar{y}(\lambda)d\lambda, \\ Z &= \int R(\lambda)\bar{z}(\lambda)d\lambda \end{aligned} \tag{5.1}$$

Then, the normalized chromaticity coordinates below can be used to determine the color in XYZ space according to the CIE standard chromaticity diagram.

$$\begin{aligned} x &= X / (X+Y+Z), \\ y &= Y / (X+Y+Z), \\ z &= Z / (X+Y+Z) \end{aligned} \tag{5.2}$$

With these x, y, and z values, the color in XYZ space can further be converted to an RGB

color for output by a display device, which requires transformation by the appropriate chromaticity matrix. To fit the experimental condition better, the spectrum of the light source can also be added to each part in Equation 5.1.

On the other hand, it's important to note that the color sensitively depends on several conditions. This is possibly caused by a combination of multiple influences including incident angle, and higher-order diffraction due to a large period. The influence of these conditions could cause the observed color from fabrication in the later part to have some differences from the simulation.

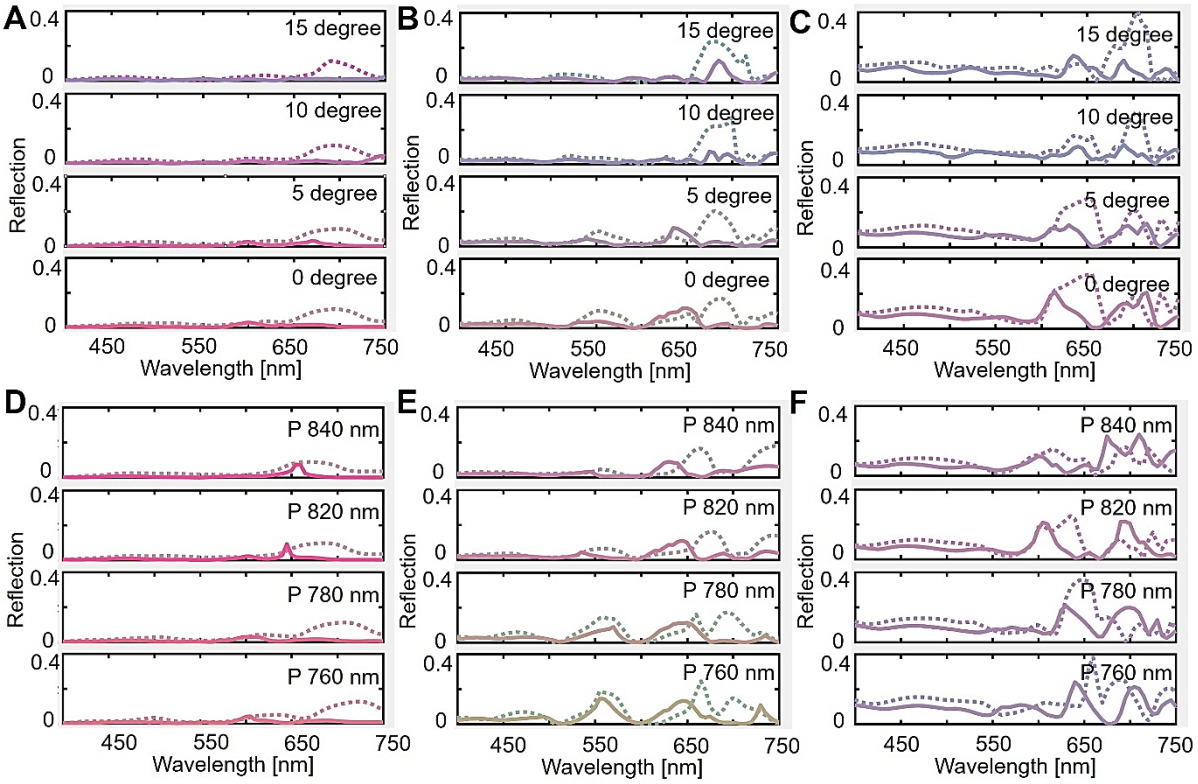

Figure 5.4 Simulated results for different incident angles and periods for the three antenna sizes. 260 nm (A, D), 410 nm (B, E), 560 nm (C, F), resonant peaks are sensitive to these parameters and may cause the colors from the experiment to be different with simulation (the RGB color is used to plot each spectrum, dash line in air, solid line in the water).

To get a supperwettability state through the selection of surface structures, a properly designed size should be considered.[115, 120] As proved by previous research, the droplet on a surface with larger CA especially at Cassie state is advantageous for self-cleaning performance, with water droplet partly in contact with the structure at this state and roll off and take away the contamination from the surface easily. In this Cassie state, the apparent CA (θ_m) can be calculated from the equilibrium CA of the flat surface (θ) and $\emptyset_S$ the solid fraction (the area fraction of the liquid-solid contact):[118]

$$\cos\theta_m = -1 + \emptyset_S\,(cos\theta + 1) \tag{5.3}$$

A drop on a substrate can also occupy a second equilibrium state as the Wenzel state. The droplet wets all the structure in this case. The apparent CA is then a function of the surface roughness (the ratio of the actual to the apparent surface area of the substrate) and the equilibrium CA of the flat surface:[118]

$$\cos\theta_m = r\cos\theta \tag{5.4}$$

Structures that could support relatively larger CA in both models would be beneficial for the experimentally measured CA and self-cleaning property as proved in previous research.[115] As solid fraction and surface roughness are the two critical parameters that need to be considered, these two models also mean that metasurfaces constructed by specially designed antennas for unique optical performance are not the best structural design for wettability control.

Considering the fixed design of nanostructures and the relatively small area of most metasurfaces, supporting structures with better wettability performance are designed at a large area to compensate for the influence of metasurfaces. This strategy provides more freedom to tune the wettability performance and structures in a large area are always useful as the contact area between a surface and droplet is on a millimeter scale. Here, supporting structures with pillar size around 1 μm and a period of 3 μm, which is within our fast fabrication limit by UV laser lithography and also presents better wettability performance at the same time.

5.2.3 Fabrication strategy toward the real situation

Based on the superwettability design criteria, a metasurface with specifically distributed nanoantennas cannot meet be the suitable design to achieve the desired wettability. On the other hand, in almost all cases, it's unnecessary and too time-consuming to fabricate an optical metasurface with a large area. So, the well-designed supporting structures that can be fabricated efficiently are designed to compensate for the relatively poor wettability of the metasurface area. Here, the problem of both large area and high precision fabrication requirements is solved by the following multi-step fabrication strategy, which provides both required wettability and optical functionality at the same time as shown in Figure 5.5.

First, the nanosized metasurface mask is fabricated by a standard EBL process (Step 1); then, a following UV laser lithography is conducted to fabricate the resist mask of the structure in a large area, that is used to support the wettability (Step 2); further, the sample is etched with both masks together and followed by removing the residues (Step 3); finally, the corresponding wettability treatment is used to induce the superwettability state (Step 4). In detail: the wettability supporting structures are constructed by uniform arrays (a square pillar size around 1 μm, the distance between adjoin pillars is 2 μm) that can improve the wettability performance according to available published results, which we confirmed in tests without the metasurface area. The etching step uses resist and Cr masks together, which provides protection against etching for both metasurface and wettability supporting structures at the same time. Wettability

treatment by Octadecylphosphonic acid (ODP) modification results in a surface with a quasi-superhydrophobic state, while a fast O_2 plasma treatment can change the surface back to the superhydrophilic state. The O_2 plasma treatment induces more polar bonds on the antenna surface, which makes it hydrophilic; while the ODP modification coats a low-surface-energy molecule on the surface and results in a non-polar and hydrophobic state.

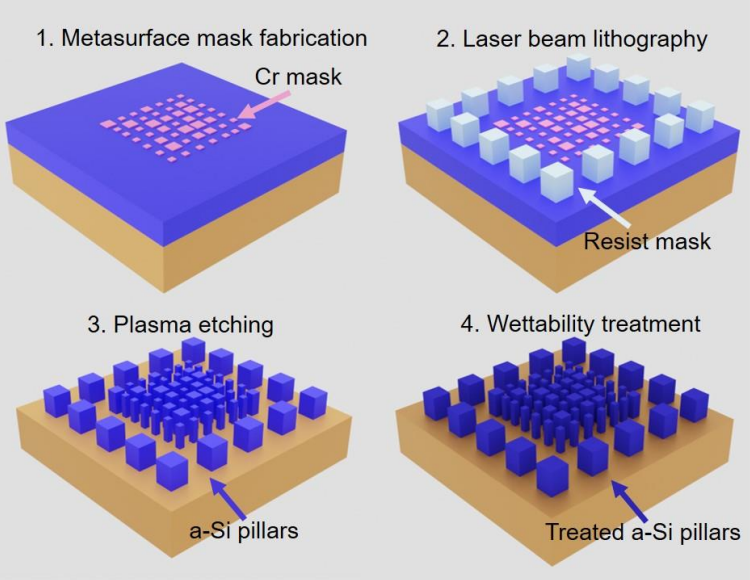

Figure 5.5 Illustration of sample fabrication strategy. The sample is fabricated in four main steps: (Step 1) fabricating the Cr mask of optical metasurface by standard electronic beam lithography (EBL), (Step 2) fabricating the resist mask of wettability supporting structures by laser beam lithography, (Step 3) plasma etching and removing of masks, (Step 4) corresponding treatment to achieve the desired wettability state.

5.3 Experiment characterization of the multifunction metasurface

5.3.1 Sample fabrication

Here, we introduce the sample fabrication procedure in our experiments step by step. First, a Cr mask corresponding to the designed QR code image is fabricated on an ITO substrate with 700 nm a-Si by standard EBL process consisting of electron beam resist spin coating, structure patterning, development of the exposed resist, Cr mask (20 nm) deposition and lift off. Then, by using the Cr mask on the sample, we spin coat another layer of UV sensitive negative resist and perform UV laser lithography with high throughput (around 10 mins to pattern the 10 x 10 mm^2 area). Developing the resist after UV laser lithography results in two masks (Cr and resist mask). Further, the etching step provides both nano-sized metasurface and wettability supporting structures together. Finally, the sample after etching is cleaned in acetone and Cr etching solution separately to remove the remaining resist and Cr mask.

For the hydrophobic treatment, isopropanol is used as a solvent to produce the ODP (Sigma-Aldrich) solution directly. Before modifying the sample with ODP, the sample is

treated with O_2 plasma for 5 mins to increase the polarity of the structure, then it is immersed in the ODP solution for 1 h. The sample is then rinsed with isopropanol and blown with nitrogen gas. To achieve the superhydrophilic sate, the same sample is treated with O_2 plasma for 5 mins, and all the measurements are finished within 2 hours.

It's important to note that modification of low-surface-energy ODP molecule only forms a very thin layer on the sample, this process almost does not influence the optical performance of the metasurface as shown in the structural color image and SEM image in Figure 5.6. The QR images before and after ODP modification do not show any difference.

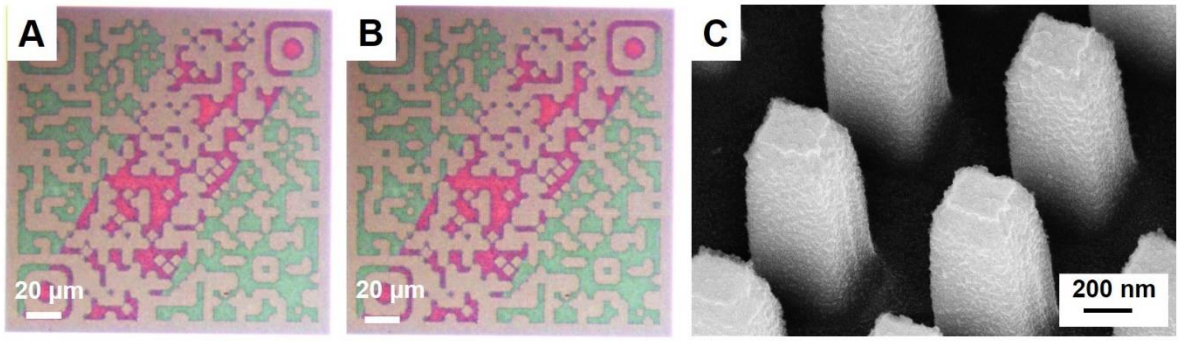

Figure 5.6 Optical image of QR code image before and after ODP modification, SEM image of antennas after modification. (A) Before ODP modification. (B) After ODP modification. No color change of the metasurface in an optical microscope is observed from them. (C) SEM image of the antenna shows the morphology remains very clean, as the self-assembled ODP molecules only form a very thin layer.

5.3.2 Wettability performance

Normally, the wettability of the sample can be easily evaluated by measuring the static value using a CA meter in the ambient environment. Here in our experiment, a 5 μL droplet of deionized water is used in the measurement. The reported CA value in the thesis is an averaged value over three measurements.

After the fabrication of two samples (with and without wettability supporting structure) with the QR image pattern in the center are at different states, CA is measured as shown in Figure 5.7. The SEM images are shown in the left column, with three recognizable areas in the QR code image area corresponding to the three antenna sizes. For the sample with supporting structure, the uniform area (SEM image at the top left corner) corresponds to the wettability supporting structures on the sample. Each metasurface with the QR code image has an area of 180 x 180 μm^2 with a total number of 225 x 225 pixels.

After fabrication without any further treatment, CAs around 70 - 100° are measured, which is a moderate value that belongs to the normal state. The wettability of this normal state is similar to the most surface, as no superwettability can be measured. On the other hand, both wettability treatments of the sample without supporting structures do not change the CA

remarkably (bottom row, CA ~26° to 108° after hydrophilic and hydrophobic treatment). In stark contrast, the sample with wettability supporting structures achieves a CA less than 10° after the hydrophilic treatment, while this value boosts to larger than 130° after the hydrophobic treatment. The larger CA difference is what we desire as it may provide both better color response and self-cleaning property according to the working principle we introduced above. The results here also verified the design strategy by embedding the metasurface within the wettability supporting structures, which makes it possible to improve the wettability performance through tuning of the structure or modification method. This wettability performance is highly possible to improve further if we can optimize the design and fabrication of the supporting structures.

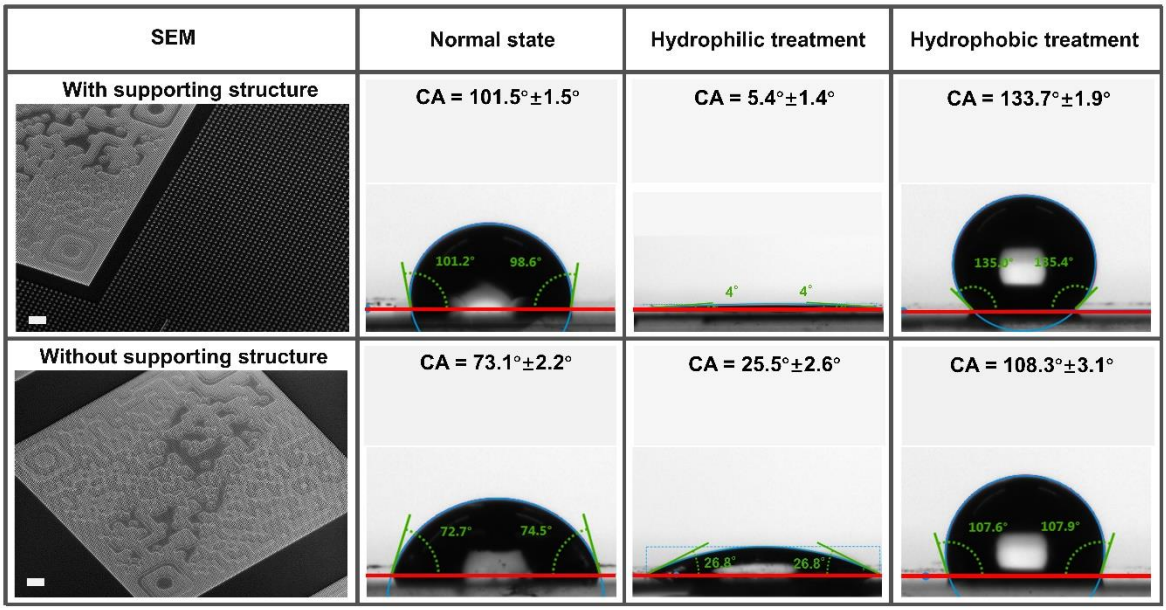

Figure 5.7 CA evolution of two samples with and without wettability supporting structure. The uniform area in the SEM image (top left corner) corresponds to the wettability supporting structures on the sample. Both samples do not show extraordinary wettability at the normal state (second column, CA ~ 101° and 73°). The sample with supporting structure shows a larger CA difference after the hydrophilic and hydrophobic treatment (last two lines, CA ~ 5° to 134° vs CA ~ 26° to 108°). Details of the CA measured results: the red lines show the baselines of the surface, the curved blue lines correspond to the profile of the water droplet, the green lines show the tangent of the water droplet, the CA is the angle between the red and the green line in each image. The reported CA in the figure is an averaged value over three measurements. Scale bars are 10 μm.

5.3.3 Optical response and self-cleaning performance of the metasurface

The optical characterization of the metasurfaces is based on a homemade microscope, under white light illumination, the images and the reflective spectra are recorded by a CCD and a spectrometer. First, a 10x lens with NA of 0.3 is used in our setup to measure the reflective spectra of uniformly arranged arrays in air and the corresponding color response (reflective

spectra) by immersing the same structure in deionized water.

From these recorded spectra, we can easily note that most of the observed colors and experimentally recorded spectra match the simulation to some extent. Similar to the simulation, for the 410 nm size antennas (Figure 5.8B), two notable peaks around 500 - 550 nm and 650 - 700 nm are present in the air, resulting in the observed green color; while the relative peak intensity around 500 - 550 nm drops a lot in the water, with the other peak at long wavelength range shifts to around 650 nm. The green-red color change can be observed when switching the sample from air to water. For the 560 nm size antennas (Figure 5.8C), two peaks around 650 nm and 700 nm are present both in air and water, and an intensity drop for both of them is observed in water. The slight peak shift and the dropping off of the intensity in water cause the color difference observed in the experiments with this design.

Still, some differences can be found between the simulation and experiment, which are possibly caused by a combination of multiple influences, including incident angle, higher-order diffraction due to the large period, and fabrication tolerances as explained above.[121, 122] Here in the experiment, the illumination white light source is focused by an objective lens, which results in a larger range of incident angles compared to the normal incident case, while the fabrication tolerances always result with a non-uniform rectangular solid antenna. Therefore, the simulation results in Figure5.3, where only one specific case of antenna geometry is calculated, show just some correspondence with the experiments. The influence from the fabrication may even be obvious when the antenna size is 260 nm, which is highly possible due to a higher sensitivity to the size and the low reflection of this design.

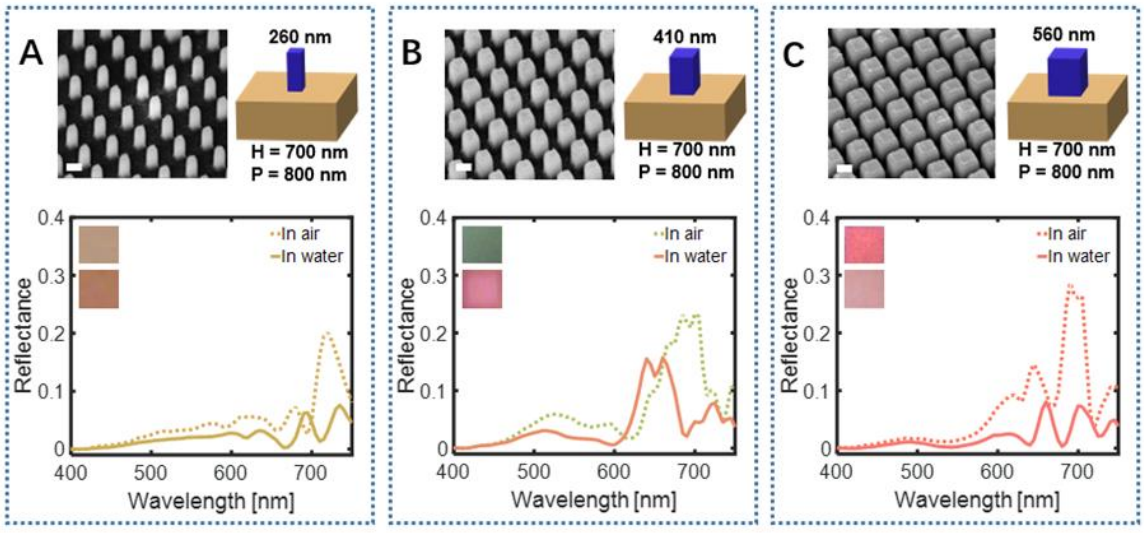

Figure 5.8 SEM images and reflective spectra from experiments for uniform arrays with three different antenna sizes in air or water. (A) 260 nm, (B) 410 nm, (C) 560 nm. The SEM images of uniform arrays for the three selected sizes are shown in the top row, good quality and corresponding sizes are observed. The corresponding RGB color of each spectrum record from the experiment is used to plot the data. Both spectrum and color from the experiment are similar to the simulation in Figure 5.3. Scale bars in the SEM images are 200 nm.

Metasurfaces showing QR code images that are made of the above three antennas are used to visualize the dynamic and self-cleaning property here. Recording the QR code image directly shows the metasurface performance at different steps. As shown in Figure 5.9, under white light illumination, similar QR code color images can be recorded in the air for both samples by different treatments. In stark contrast, only the state after hydrophilic treatment can be used to record the color change of the QR code image in the water, the other states do not show any clear image due to the formation of a water droplet on the surface. Here, the unclear image is mainly caused by two threats and cannot be improved even with further focus tuning based on our observation. Firstly, light is easily influenced by the curved surface of the water droplet on the metasurface. Secondly, the air is trapped between the antennas because of the poor hydrophilic performance, which further causes aberrations of images due to the random scattering of reflected light from the antennas. Both images in air or water are similar to the simulation (right column), especially the corresponding green-red color change from air to water. Here, although these two samples after hydrophilic treatment show a similar static image, the better hydrophilic performance of the sample with wettability supporting structures is helpful for more efficient response, as shown by Mohd-Noor et.al., who designed an ultra-fast response humidity optical sensor with hydrophilic TiO_2.[111] Unfortunately, our current setup cannot be used to observe the entire dynamic behavior to compare more details of the response time. However, a spreading time of the water droplet on the superhydrophilic surface that is less than 20 ms can be used to estimate the dynamic response, which is on a similar level to their measurement with the optical sensor. The difference in color change with different wettability is explained by an illustration of the water droplet state on each metasurface in Figure 5.9 bottom row.

Furthermore, the dynamic response of a metasurface by changing the environmental refractive index with water degenerates when the sample is stored after some time (see normal state). The degeneration of the superhydrophilic state is observed for different kinds of surfaces, which mainly results from the absorption of polar groups in air.[117, 123] With a proper wettability treatment or design, it is possible to keep this function for a longer time. Here, the hydrophilic performance with the wettability supporting structures can keep the state around double time compared to the other samples. The improvement is highly possible for better initial wettability with the supporting structure.

Except for the optical response, the perfect matching between the surrounding liquid and the metasurface can also be useful for more specific applications like underwater detecting or imaging, if we recall the refractive index matching method of traditional optical components. A similar strategy can also be used to fabricate superoleophilic surfaces, which further extends the choice of matching solution.

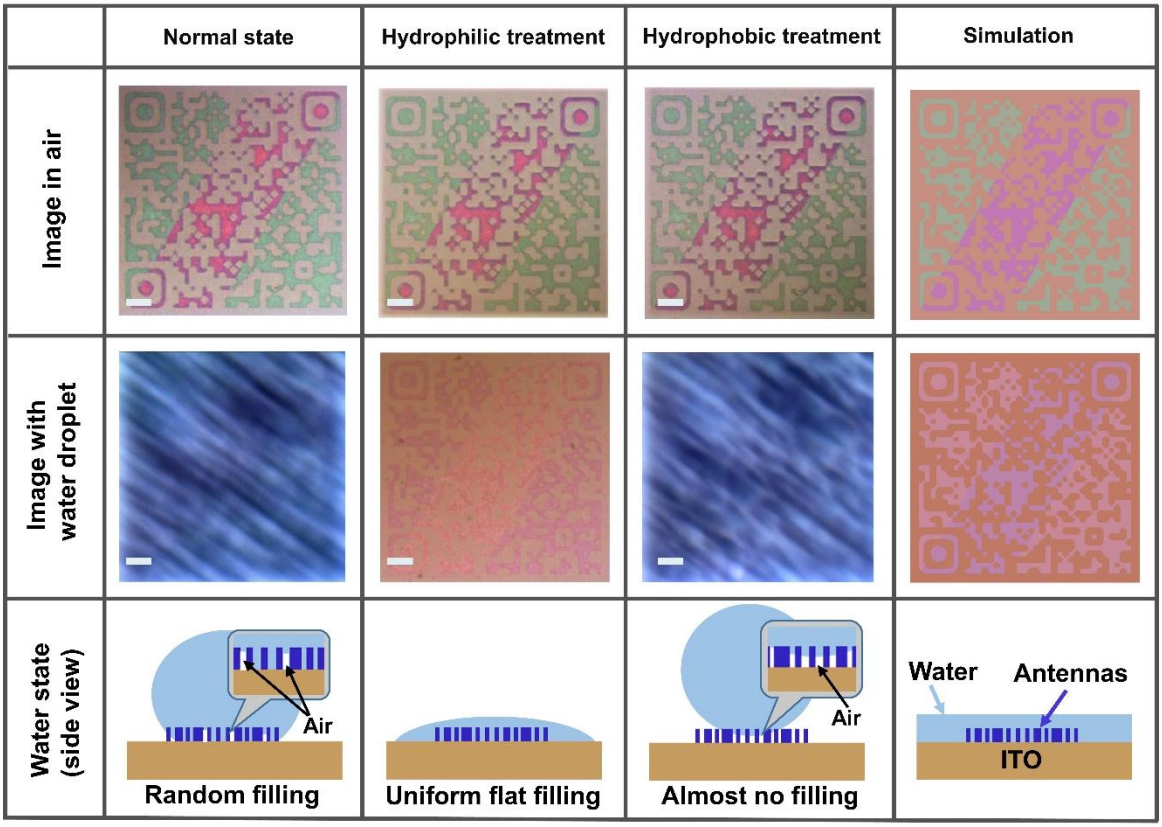

Figure 5.9 Color response of the metasurface with wettability supporting structures in air and water. All the states clearly show color images in the air (first line) similar to the simulation, while only the hydrophilic treated state (second column) shows a color change image with water droplet. The corresponding diagrams illustrate the water droplet state on the surface (last row), showing the importance of perfect matching between water and nanoantennas to the dynamic color response. Scale bars are 20 μm.

We should note here, as shown in Figure 5.10, although the statistic image from the other sample only with metasurfaces structures after hydrophilic treatment seems similar to the sample with wettability supporting structures (in Figure 5.9 above), the response is less stable for this sample, which may be mainly caused by the poor wettability performance at starting state.[118, 124]

In the following, we test the self-cleaning property and compare the performance of the two samples. The two states show better hydrophobic properties after the ODP modification are used, as a larger CA is helpful for the self-cleaning of particle-based contaminations. During cleaning, the sample is placed at a tilted angle of around 45°, with carbon particles as the artificial contamination to cover the whole sample area. Then, water at room temperature is dropped onto the metasurface to clean the surface. We observe the particles stick outside the droplets and are washed away from the metasurface area when the droplet is rolling over the contaminated area (cleaning process images in Figure 5.11). For the other sample without supporting structure and with the same cleaning condition, there is always a large water droplet that adheres to the surface together with lots of particles during the whole process, which is

caused by the poor hydrophobic area outside the metasurface region. Therefore, the balance of capillary and adhesion force between the droplet and the contamination on the substrate that determines the friction force of drops during self-cleaning causes most particles always be stuck there, so that they cannot be cleaned away anymore.

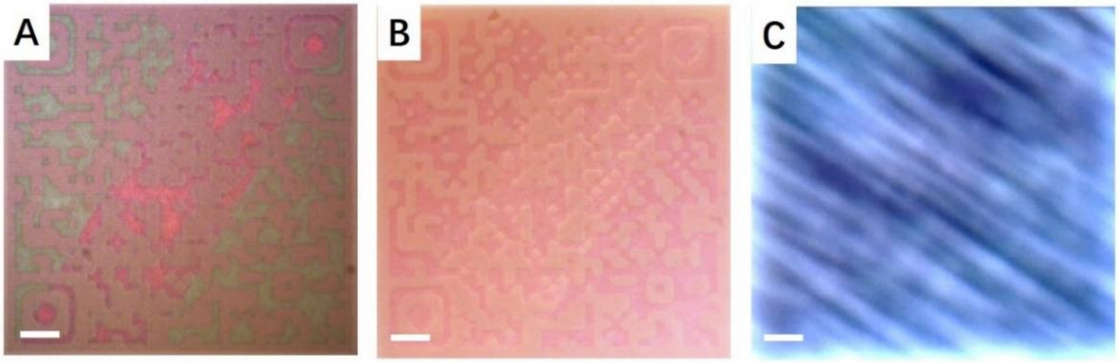

Figure 5.10 Color response of the sample without wettability supporting structure. (A) image in the air, (B) image in the water, image with a water droplet on the surface after storing for 1 hour (C). Although the sample shows a similar statistical image in the water, the ability degenerates easily due to the relatively poor hydrophilic performance after fabrication (1h for this sample, while the sample with supporting structures records a clear image after more than 2 h). Scale bars are 20 μm.

For the metasurface with self-cleaning property, Wu et.al. recently demonstrated that antennas constructed with TiO_2 can be used to remove some chemical contamination, which is mainly due to the photocatalytic reaction.[71] Besides the chemical contamination, evading particle or dust adhesion on the metasurface during daily usage is also extremely critical for most metasurface applications. Based on our observation, once the particle sticks on the sample, especially for the small particles that can reside inside the gap between the antennas, it's almost impossible to remove them anymore by water cleaning.[115, 120, 125] Due to the weakness of nanoantennas, it's also hard to clean the particles by other methods. Therefore, our design with supporting structures that can enable the one-step removal of particles is highly promising.

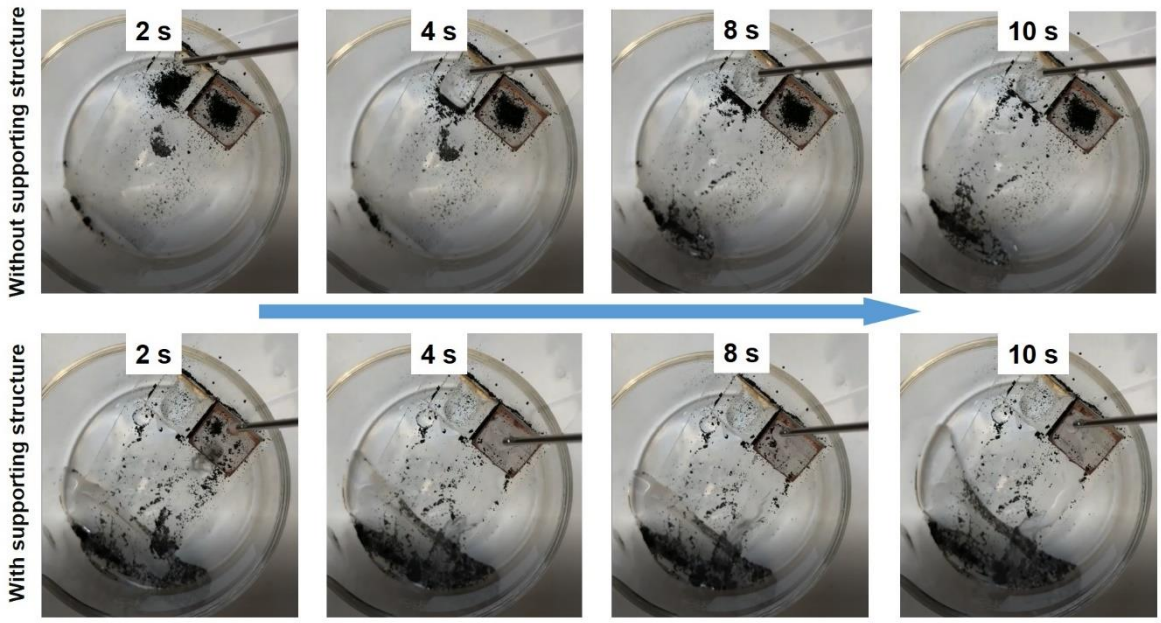

Figure 5.11 Images from the self-cleaning process. For the sample with supperwettability, the particles stick outside the droplets and are washed away from the metasurface area when the droplet is rolling over the contaminated area. While the other sample without supporting structure and with the same cleaning condition, there is always a large water droplet that adheres to the surface together with lots of particles during the whole process.

The QR code images after the self-cleaning process can be used to visualize the cleaning performance directly, with the same image as the initial one that is recorded for the metasurface embedded within the wettability supporting structures (Figure 5.12). However, lots of small dark areas caused by the contamination are found on the other sample without wettability supporting structures, and further processes cannot clean it anymore as shown in the images at the bottom. Further checking of the metasurface after cleaning is performed by SEM, where we do not find any obvious particle left in the QR code image area for the sample with supporting structures. Here, the few particles present at the metasurface edge or supporting structure are mainly caused by the blank area without any structures and also the imperfect arrangement of uniform arrays. The obvious difference in cleanness shows that the hydrophobic design with a large area improves the self-cleaning performance a lot.

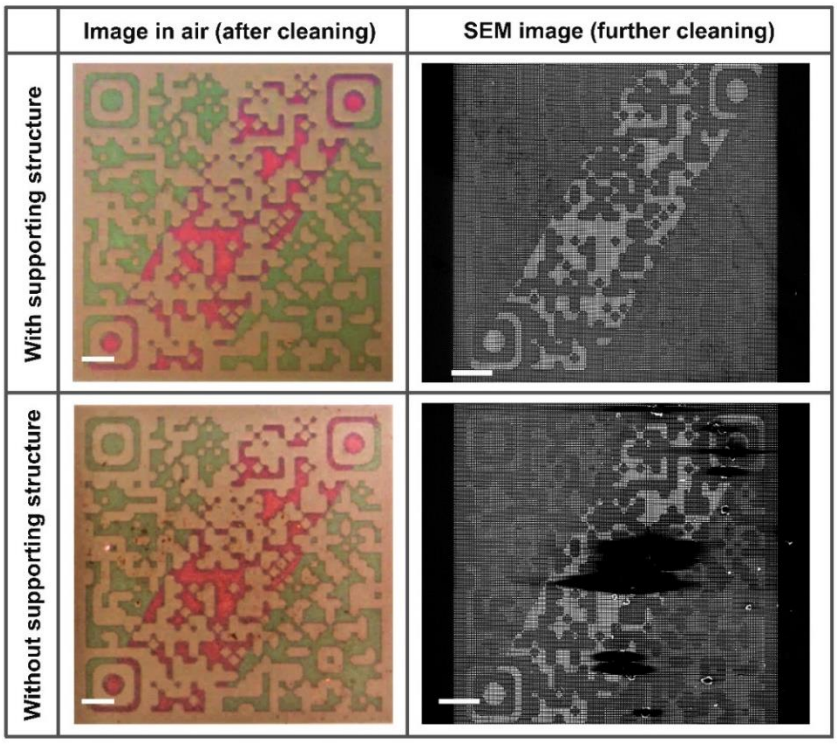

Figure 5.12 Comparison of the self-cleaning performance of metasurface. No particle is observed on the sample with wettability supporting structures (both in the optical and SEM image, top row). Lots of particles are present in the images from the sample without supporting structures (bottom row). Scale bars are 20 μm.

5.3.4 Stability working of the multifunction metasurface

More interestingly, for the metasurface with supporting structure, we can randomly choose our metasurface at the self-cleaning state or at the color response state that is guaranteed by the corresponding wettability treatment. With O_2 plasma treatment or ODP modification, the transition between superhydrophilic and quasi-superhydrophobic states including the self-cleaning process is tested by three cycles, where almost no structural color degeneration as shown in Figure 5.13. Recently, TiO_2 based dielectric metasurface gained lots of attention, with TiO_2 as a good photocatalyst and can be used to induce wettability transition under UV light irradiation; metasurface constructed by similar functional materials could provide far more exciting applications in the near future.[123, 126] Here, the switching of functionality signifies that we can choose the required state for the metasurface on-demand, i.e., the ODP modified superhydrophobic state can be used to store the sample once the structures are fabricated, this can be used to protect or easily clean them during daily use. Then, the superhydrophilic state can be induced once a specific application like a dynamic response or perfect solution matching is needed.

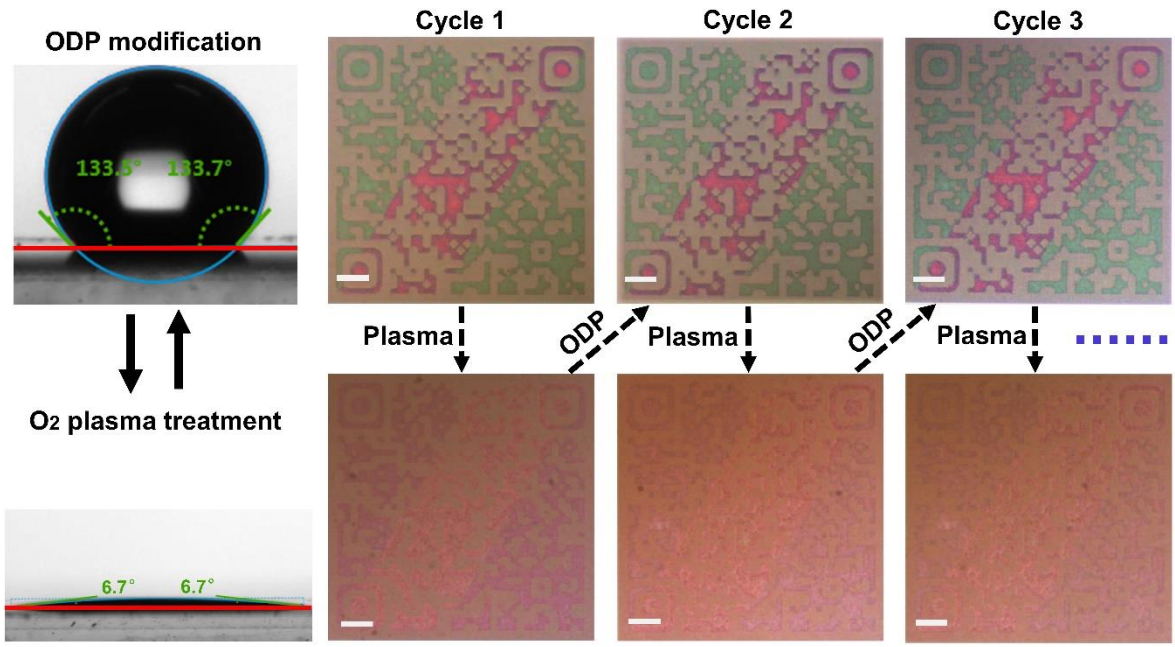

Figure 5.13 Repeatability testing for three times between the self-cleaning and dynamic response. The process starts with modifying the surface with ODP, followed by self-cleaning. Then the sample is treated with O_2 plasma, after which the dynamic response image in water is recorded. No noticeable degeneration of optical performance is observed after three cycles. Scale bars are 20 μm.

With two samples and six metasurface patterns on each (both with wettability supporting structures), we check more details of the remaining particles on the surface by SEM and summarize the repeating cleaning results in Figure 5.14 (one cycle includes both self-cleaning and color response). Both samples showed at least three metasurface fields (half of the total number) with less than five particles after three repeating cycles, and most of the fields are still kept rather clean, as only one of them shows more than twenty particles. The results show that the cleaning process works well for the design strategy. Here, we also see the importance of cleaning at every step, as once the small particles stick on the sample, it's almost impossible to remove them anymore by normal water cleaning procedures due to the weakness of nanoantennas with small particles resident inside. These results further demonstrate that the self-cleaning process works for the sample with wettability supporting design, as all the six metasurfaces are not cleaned at the first cycle for the sample without wettability supporting structure.

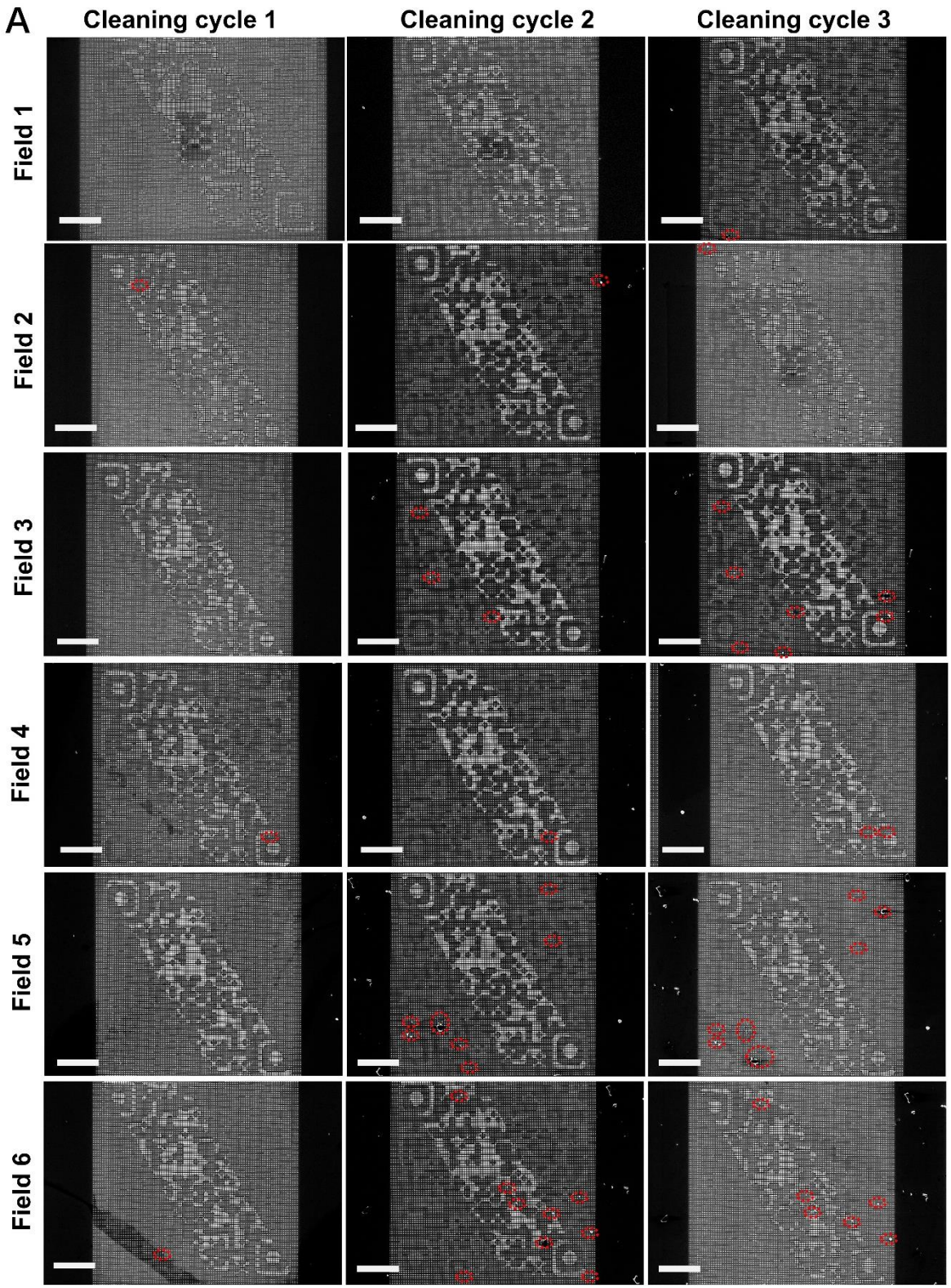
A
Cleaning cycle 1
Cleaning cycle 2
Cleaning cycle 3
Field 1
Field 2
Field 3
Field 4
Field 5
Field 6

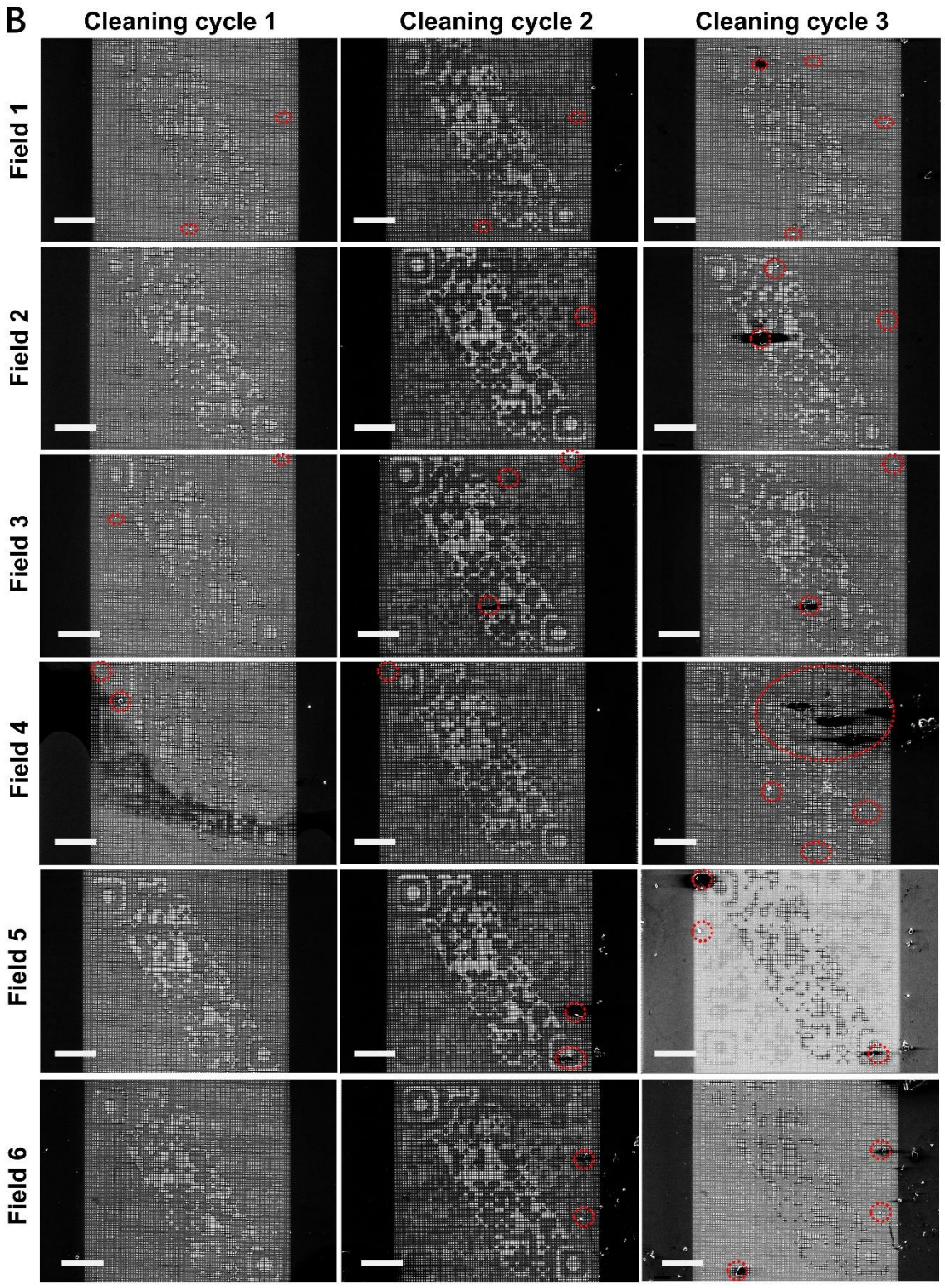
B
Cleaning cycle 1
Cleaning cycle 2
Cleaning cycle 3
Field 1
Field 2
Field 3
Field 4
Field 5
Field 6

C

	Sample 1			Sample 2		
	Cycle 1	Cycle 2	Cycle 3	Cycle 1	Cycle 2	Cycle 3
Particle number = 0	3	1	0	3	0	0
Particle number ≤ 5	3	3	3	3	6	5
Particle number > 5	0	2	3	0	0	1
Max particle number	1	9	7	2	3	>20

Figure 5.14 SEM of two samples with wettability supporting structures for 3 times repeating the testing. (A) Sample 1, (B) sample 2. The red circles mark out the remaining carbon particles after cleaning. The statistic results of 6 fields in the 2 samples cycling for 3 times are shown in (C). Both samples exist at least three metasurface fields (half of the total number) with less than five particles after three repeating cycles, and most of the fields still keep rather clean with only one field remaining with more than twenty particles. Scale bars are 20 μm.

5.4 Conclusion

By using a structural color metasurface as a platform, we show a straightforward route to achieve versatile functionality with both self-cleaning and dynamic color response based on the superwettability property. The self-cleaning ability is achieved at the ODP modified quasi-superhydrophobic state, which can be used to efficiently self-clean particle-based contamination with water. The superhydrophilic state response is used for obtaining a rapid dynamic structural color change. We found that the superhydrophilic state is stable once the surface is treated with O_2 plasma. Furthermore, the proposed metasurface can easily be switched between these two states, no performance degradation is observed after three repeating cycles.

Wettability can be achieved by many more methods beyond that we present here. For example, the two-step fabrication process or uniform wettability supporting structures can be replaced by other proper strategies to reduce the complexity of fabrication or improve the device's performance. With proper designs and wettability states, an extension to metasurfaces will provide more functionalities besides the self-cleaning and color response presented in this work. Furthermore, by constructing metasurfaces with materials like ZnO or TiO_2 that are widely used in wettability design and transition, these functionalities may be easily incorporated into metasurfaces.[71, 125-128] Our design strategy can also be extended to the fabrication of other optical metasurfaces, which can be used for applications in more complex environments.

6. Conclusion and outlook

Si nanophotonics is of great interest for the miniaturization of photonic systems, which are promising for high-speed data transmission and all-optical computing like electronic devices nowadays. In this thesis, TPhCs and metasurfaces realized with Si are used to investigate the light tailoring performance in various applications after the miniaturization of the devices' size down to the nanoscale. The design of TPhCs is based on the simulation results from COMSOL Multiphysics, and the spectra of metasurfaces are calculated by RCWA. To realize the simulated design, the fabrication of these devices is done by standard EBL process including lithography, mask evaporation, lift-off, and plasma dry etching.

Based on the weak topology theory, TPhCs are designed to realize robust and versatile topologically protected 0D localized modes at optical frequencies. When a TPhC is designed with a nontrivial Zak phase and an edge dislocation that has the same direction, we show that due to the weak topology, differently extended dislocation centers induce similarly strong light localization. Further, we use s-SNOM to verify the mid-bandgap light localization in TPhCs with different design layouts. Based on the versatile design with weak topology, a larger number of unit cell extensions at the dislocation center resulted in a reduced mode area of ~ 0.17 λ^2, which is achieved for the design with the dislocation center extensions of $N = 6$ due to the scattering suppression with a smaller vacant area in the array, which is also observed in the measurements.

The confining of light at optical frequencies to a point is promising for lots of applications from nonlinear optics, quantum optics, and miniature active photonic device integration. The feasible strategy for accessing and tuning a topologically protected 0D localized state at infrared frequencies is highly promising for these applications. On the other hand, we also show that s-SNOM is a valuable tool for characterizing TPhCs with nanoscale resolution at optical frequencies. In the near future, this design can be used to realize robust and active topological nanophotonics by programmable PCMs with tunable refractive index, which is important for on-chip light sources.[101] Furthermore, the rapid progress of nanotechnology makes it possible to equip the defect center with quantum emitters, nanocrystals, or molecules, which is highly promising for novel hybrid nanophotonic devices for single-photon generation.[39, 104]

On the other hand, the valley-dependent TPhCs provide a new degree of freedom for realizing topologically protected robust light transport. Taking these advantages, we simulate the topologically protected kink states and experimentally verified the VPCs for on-chip light control by fabricating devices with SOI material. Furthermore, the new degree of freedom provides the possibility to obtain more complex functionalities, i.e., topologically protected resonators and beam splitters, which are important fundament components for on-chip photonic integrated circuits. More specifically, a topologically protected resonator with a high Q factor

larger than 9000 can be easily obtained only with a triangle shape with a side length of around 5.5 μm. While the topologically protected beam splitters provide a design that can realize robust photon separation and interference. With the verified results by classical light measurements, we seek to extend our design to quantum optical circuits, which is highly promising to obtain robust quantum integrated optical circuits, with photon generation, transmission, and interference in small area topological photonics.

Compared with other TPhCs, the design based on the valley phase is extremely important for on-chip light control due to its easy realization with available mature technologies. Just as shown in our work, this design can also be used to integrate with traditional waveguides with low loss. Furthermore, the new degree of freedom for realizing topologically protected robust light transport bounded to different valleys is extremely important for realizing complex design within a small area. For example, different from bends with Si waveguide is typically in the order of tens of microns in size, photonic routing with topological design can realize efficiently navigated scatter-free light transmission even in very sharp bends.[1, 21] Such design in Si photonics could continue to see more advances with other Si-based or CMOS compatible materials.

In addition, it is known to all the researchers in nanophotonics that the weakness of nanostructures gives rise to the crucial problem and challenge to protect them from dust or clean the unavoidable contaminants during daily usage. How to solve this problem will continue to be a problem in the near future if this nanophotonics wants to be used in more practical cases. Inspired by the physical stability of superwettability surfaces, we conduct work to equip Si nanoantennas with the same ability. Benefiting from the special wettability design, the superhydrophilic state enables an enhanced optical response, while the quasi-superhydrophobic state imparts the fragile antennas an ability to self-clean dust contamination, with these two wettability or functional states can be easily switched and repeated stably by appropriate treatments.

As wettability design has many available methods beyond that we present here, more work can be done to improve the fabrication strategy or performance. For example, the two-step fabrication process or uniform wettability supporting structures can be replaced by other proper strategies to reduce the complexity of fabrication or improve the device's performance. With proper design and wettability states, an extension to metasurfaces will provide more functionalities except for self-cleaning and color response in this work. Furthermore, by constructing metasurfaces modified with ZnO or TiO_2 that are widely used in wettability design and transition, these functionalities may be easily incorporated into the metasurfaces.[119, 127] Our design strategy can also be extended to the fabrication of other optical metasurfaces, which can be used for applications in more complex environments.[72, 73]

In conclusion, Si-based nanophotonic elements are of special interest in integrated optical systems at a small scale, because of the potential to be compatible with the well-developed

nanofabrication technology and some devices already in place. Considering the recent success of Si TPhCs for on-chip topological light guiding and biphoton states generation, such design perhaps provides new avenues for quantum information processing, including quantum photonic logic circuits and building blocks of quantum computers. On the other hand, tuning of QVH Si photonic crystals has also been demonstrated, switching or modulation capabilities in topological Si photonic devices could also be very useful. They could then be used to demonstrate high-speed responsive devices like topological photonic modulators or optical switches.

For the further development of Si nanophotonics, another exciting route is to solve the problem of the lack of a light source on a Si chip, which is required in a variety of applications in Si nanophotonics. As Si has an indirect bandgap, lasers cannot be realized on-chip directly, but the bonding of III–V materials on it has already been proved in experiments either with TPhCs or metasurfaces. These on-chip lasers will provide superior optical properties like single-mode behavior even at higher powers. In addition, topological protection from disorder and fabrication tolerances with topological design is important for achieving high yields on-chip sources in wafer-scale fabrication.

Last but not least, unidirectional light propagation and lossless photonic routing around tight corners are useful to reduce Si integrated systems to chip footprints and enable greater device densities than presently designs with normal waveguides. With the realization of more light tailoring ability through on-chip metasurfaces, it is clear that the advancements made in Si nanophotonics hold tremendous promise, and far-reaching innovations are expected to continue in the near future.[19]

Acknowledgments

The results presented in my thesis are a summary of the major work carried out from July 2019 to March 2022 under the supervision of Professor Thomas Zentgraf. The work was initially carried out at the Department of Physics, University of Paderborn.

I would like to express my greatest thank to Professor Thomas Zentgraf, who provided me with this great opportunity to finish my thesis and continue this research at Paderborn University. He helps everyone to solve the problems that occurred not only in the research work but also in our daily life. With his powerful experience, he explained any confusion in the best way and always could show me how to do the work step by step with great patience.

I would also like to thank Professor Tim Bartley who agreed to be my second supervisor and provided suggestions for this thesis. On the other hand, many thanks to him for providing me the opportunity to do UV lithography in his lab and helping to show my results better.

I would like to thank Dr. Wenlong Gao and Dr. Basudeb Sain, both of them guided me on how to do research work at the starting point and helped me a lot to solve the problems I met. It is their help that makes me get into this research topic more easily. Thanks to Wenlong, he took the topological photonic crystal direction to our group, showed me how to do simulation step by step, and arranged all the theory work with his convincing theory knowledge. And Basudeb shared his unparalleled experience in the fabrication of samples, helping to find out the problem whenever we met trouble with fabrication.

I would also like to thank Professor Thomas Taubner at RWTH Aachen University, who provided the opportunity to cooperate with his group, guided our project, and discussed it through one of our projects. Thanks to Konstantin G. Wirth and Andreas Heßler at Professor Taubner's group for performing the near-field measurement, data processing, and keeping our research project running in an organized way. And also thank Maximilian Protte in Professor Bartley's group for helping to do the UV lithography, his great experience reduced a lot of time for some parts of my project.

I would also like to thank the senior members Bernhard Reineke, Philip Georgi, Daniel Frese, and Florian Spreyer in our group for helping to let me get more understanding of some scientific problems. They also provide very helpful explanations for the problem I encountered in my daily experiments and life whenever I asked for their advice. Furthermore, I would also like to thank other members in our research group Emmanuel Narváez Castañeda, René Geromel, Michael Brauckmann and Carsten Müller. The working experiences in this group are so great and I am truly thankful for the support from everyone above.

Last but not least, I would like to thank my parents and my family. Thank you for your support, for your patience, and for trusting in me for this path I chose. Most importantly, I

would particularly thank my wife Tingting Li for her encouragement, understanding, and patience even during some very hard times. Thanks for her support to bring our son Kasen Lu to Germany and take care of him for most of her time. Otherwise, I could lose my experience as a father and did not see how cute Kasen is due to the long-lasting corona pandemic that started the year I came to Germany.

Paderborn University is a great place to do research work, and to be familiar with the culture in Germany, I treasure every day here. The experiences here are invaluable and I will cherish them throughout my life!

Appendix

A. Simulation of band structure with COMSOL and data plotting

COMSOL Multiphysics is used to calculate the band structure of the unit cells that form the TPhCs in this thesis. It is based on the finite element method that divides the geometry of the problem that needs to be solved into small, finite elements (either in 2D or 3D cases). Each of the divided small elements constitutes a mesh, and all elements have at least one boundary in common with another mesh element. Through simplification of the partial differential equations, the geometry and physics of the simulation domain can then be expressed in terms of a high number of coupled equations. These equations then constitute matrix elements in a matrix equation that can be solved using efficient computational factorization methods. The needed results can then be derived from the solved matrix equation during some post-processing steps.

In all the numerical simulations, the final solutions include some errors. For the finite element method, the error is highly dependent on the size of the mesh, with the smaller mesh typically providing a more accurate solution and resulting in smaller errors. However, a small mesh also results in more elements and therefore a larger matrix must be solved to get a solution. These simulations with smaller meshes require more memory and simulation time, which we always need to compensate for in the particular case. The size determination rules are the same for other simulations in this thesis.

To calculate the band structure, we need to analyze the unit cell and set the Floquet periodical condition along with a certain range of k-vector in the reciprocal space. In the simulation with COMSOL, the range can be set along the edge of the irreducible BZ determined by the shape of the unit cell, where the Floquet periodical condition can be set directly in the software. To better meet the periodical condition, each pair of edges or surfaces should use the copy edge or surface function to build the mesh. An eigenfrequency solver is used to search the modes around our interested frequency.

Here, we also provide more details about how to calculate the range of the *k*-vector in reciprocal space. Using a two-dimensional honeycomb lattice as an example (the same case in chapter 4), the unit cell can be defined by its primitive vectors ($\boldsymbol{a_1}$, $\boldsymbol{a_2}$). Its reciprocal lattice is then determined by generating its two reciprocal primitive vectors, with the reciprocal lattice vectors can be calculated from $\boldsymbol{a_1}$ and $\boldsymbol{a_2}$ with the following relations:

$$\boldsymbol{b_1} = 2\pi \frac{\boldsymbol{a_2} \times \boldsymbol{a_3}}{\boldsymbol{a_1} \cdot (\boldsymbol{a_2} \times \boldsymbol{a_3})}$$

$$\boldsymbol{b_2} = 2\pi \frac{\boldsymbol{a_3}\times\boldsymbol{a_1}}{\boldsymbol{a_1}\cdot(\boldsymbol{a_2}\times\boldsymbol{a_3})} \tag{A.1}$$

where $\boldsymbol{a_3}$ is just the unit vector $\boldsymbol{e_z}$ and makes the case for two-dimensional much easier. With these calculation results, the coordinate of the irreducible Brillouin zone can be expressed with the unit cell parameters.

In the honeycomb lattice, we have $\overrightarrow{a_1} = \frac{\sqrt{3}a}{2}\hat{x} + \frac{a}{2}\hat{y}$, $\overrightarrow{a_2} = -\frac{\sqrt{3}a}{2}\hat{x} + \frac{a}{2}\hat{y}$, $\overrightarrow{a_3} = c\hat{z}$. According to the definition above, we can easily get the two reciprocal primitive vectors: $\overrightarrow{b_1} = \frac{2\pi}{\sqrt{3}a}\hat{x} + \frac{2\pi}{a}\hat{y}$, $\overrightarrow{b_2} = -\frac{2\pi}{\sqrt{3}a}\hat{x} + \frac{2\pi}{a}\hat{y}$.

To plot the band structure, a Matlab code as shown below is used to select the right eigenmodes from all the calculated data from COMSOL. This means that the eigenfrequencies with a larger imaginary part are disregarded, as the fields from these modes do not overlap with the antennas. The Matlab code to plot the band structure:

```
fidi = fopen(' band structure.txt','r'); %Read the txt file extracted from COMSOL.
Datac = textscan(fidi, repmat('%f', 1, 92), 'HeaderLines',5, 'CollectOutput',1); %Specify the colums number the header lines.
Data = Datac;
limit=0.2e13; %Select the value to disregard the useless value from simulation.
M = Data(1:61,1); %Check all the solution from difficult wave vector along the selected Brillouin zone
num_k = length(M);
num_w = length(Data(1,3:end));
max_size = 20;
Resul t= NaN*zeros(num_w,num_k);
%Plot the band structure by markers according to the imaginary part of the eigenfrequency
for m = 1:num_k
    temp = Data((p-1)*num_k+m,3:end);
    flag = 0;
    for n = 1:num_w
        if abs(imag(temp(n)))<limit
        flag = flag+1;
        Result(flag,m) = temp(n);
        figure(p)
        hold on
        plot(M(m),real(temp(n)),'ok','MarkerSize',max_size*(1-abs(imag(temp(n))/limit)))
        end
    end
end
```

The code above can also be used to determine the edge state of TPhCs with simulated results from a supercell, but the period condition only is defined for either x or y direction, while other edges or surfaces are defined as a scattering boundary condition. Similar to this, the spectrum of the TPhC is calculated in the same way, but all the edges or surfaces are defined as the scattering boundary condition.

B. Zak phase calculation from simulation

As already proved by previous research, the topology of a specifical band in a photonic system can be determined by the topological invariant linked with the Berry phase, which is the geometric phase acquired by the periodic Bloch function going a closed path in the BZ.[8] The Berry phase is defined in the following form:

$$\gamma = \oint d\boldsymbol{k} \cdot A(\boldsymbol{k}) \tag{B.1}$$

where $A(\boldsymbol{k}) = i\langle u_{\_k}|\nabla_k|u_{\_k}\rangle$ is the Berry connection, and $|u_{\_k}\rangle$ is the periodic Bloch function, with the integration is conducted in a closed path in BZ.

In a real case, the direct calculation of the Berry phase meets the problem of gauge uncertainty, and is inconsistent with all the numerical calculations as the continuous evolution of the Bloch functions in the BZ is required.[129] But the continuous evolution is impossible in numerical simulations and the BZ is always divided into some small segments. However, this calculation problem can be solved with the well-known Wilson-loop approach. Taking the Zak phase calculation as an easy example, it's a Berry phase of a specifically chosen 1D BZ (more specifically, a closed-loop for the given k_x or k_y), which can be used to understand more cases with the Wilson loop approach.

First, we rewrite the Zak phase as the following:

$$\theta = \oint d\boldsymbol{k}\boldsymbol{A}_{n,k} \tag{B.2}$$

using the Berry phase definition in B(1), where $\boldsymbol{A}_{n,k} = i\langle u_{\_k}|\nabla_k|u_{\_k}\rangle$ is the Berry connection for the nth band, $|u_{\_k}\rangle$ is the periodic Bloch function, and the integration is performed over a closed-loop for that specifically chosen k_x (with $-\pi \le k_y < \pi$ as the loop for calculation) or k_y (with $-\pi \le k_x < \pi$ as the loop) in BZ.

Then, by dividing the closed-loop of 1D BZ at the specific k point (the point corresponding to the direction of the Zak phase that we want to calculate) into N (large enough) small segments, we can approximate the integral in Equation B.2 as the summation of the contributions from each small segment. In a small segment j from k_j to k_{j+1} (range of j is from 1 to N), we have $e^{-i\theta_j} \approx 1 - i\theta_j = 1 - i\boldsymbol{A}_{n,k}\delta\boldsymbol{k}$ if N is sufficiently large, and the differentiation of the Bloch functions over k is replaced by the finite differences. Then the Berry phase θ_j in segment j is given by $e^{-i\theta_j} = \left\langle u_{n,\boldsymbol{k}_j}\middle|u_{n,\boldsymbol{k}_{j+1}}\right\rangle$.

Further, the Zak phase corresponding to this k point is just the summation of the Berry phase in all small segments:

$$e^{-i\theta} = \prod_{j=1}^{N} e^{-i\theta_j} = \prod_{j=1}^{N} \left\langle u_{n,\boldsymbol{k}_j} \middle| u_{n,\boldsymbol{k}_{j+1}} \right\rangle. \quad \text{(B.3)}$$

This method does not require the continuous evolution of the Bloch functions in the BZ, as each of them appears twice in the above product. The gauge-invariant calculation here is the basic starting point of the Wilson-loop approach and allows for the topological invariant calculation from numerical simulation.[6, 129]

In our calculation from the numerical simulation, as no magneto-electric coupling is considered, the Berry connection can be given by $\boldsymbol{A}^{E}_{n,k} = i\langle u^{E}_{n}(\boldsymbol{k})|\varepsilon(\boldsymbol{r})|\partial_k u^{E}_{n}(\boldsymbol{k})\rangle$, which is the contribution from the electric fields for the nth band. Then, with $u^{E}_{n}(\boldsymbol{k})$ for each k point obtained from numerical simulations in COMSOL Multiphysics, the Zak phase is the imaginary part of the logarithmic of all the multiplication, which is obtained from a Matlab code by dealing with the exported numerical simulation.

More specifically in our case, the 2D Zak phase for $\theta_{\Gamma X}$ in chapter three is calculated for $k_y = 0$, while the loop is $-\pi/P \le k_x < \pi/P$; $\theta_{\Gamma Y}$ is calculated for $k_x = 0$, while the loop is $-\pi/P \le k_y < \pi/P$. The results give $\theta_{\Gamma X} = \pi$, $\theta_{\Gamma Y} = 0$. θ_{XM} is calculated for $k_x = \pi/P$, while the loop is $-\pi/P \le k_y < \pi/P$; θ_{YM} is calculated for $k_y = \pi/P$, while the loop is $-\pi/P \le k_x < \pi/P$. The results give $\theta_{XM} = 0$, $\theta_{YM} = \pi$, which are the same as the determination from the electric field distribution.

C. Grating coupler simulation with COMSOL and measured grating efficiency

COMSOL Multiphysics is also used to simulate the grating coupler and perform related optimizations. The electromagnetic wave optics module from the software is used in this part for waveguide and grating coupler simulations. As the band structure and edge states of our TPhCs are based on the TE mode, a single TE mode waveguide is required for the on-chip coupling. To get the width range of the TE mode waveguide for our SOI material (the thickness of the Si layer is 340 nm), the cross-section of the waveguide as shown in Figure C.1 is used in the simulation to calculate the effective refractive index and corresponding field distribution. Here, the material from top to the bottom: air, Si and silica. The refractive indices of the Si, silica and air regions are $n_{Si} = 3.48$, $n_{SiO2} = 1.45$ and $n_{air} = 1$, respectively. The boundary mode analysis study is used, and the parameter sweep is used for different waveguide widths. The single TE mode should have a width range from 260 nm-510 nm according to the effective refractive index and the refractive index of the glass substrate.

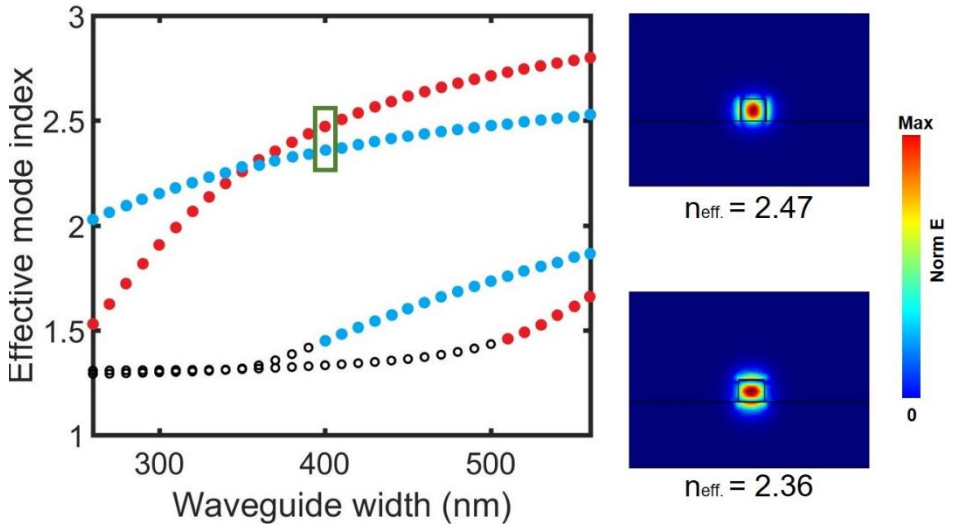

Figure C.1 Cross-section of the waveguide and definition of the model in simulation. The Scattering Boundary Condition is used for the out shape, and the center rectangle is the waveguide. The TE modes with effective refractive index ($n_{eff.}$) that are larger than 1.45 are marked with red dots. The field distribution is shown for a TE single-mode when $n_{eff.}$ is 2.47 on the right. The TM modes with $n_{eff.}$ that are larger than 1.45 are marked with blue dots. The field distribution is shown for a TM mode when $n_{eff.}$ is 2.36. A single TE mode waveguide should possess a width range from 260 nm to 500 nm as determined from the plotted $n_{eff.}$

The grating coupler is based on a varying arrangement of different materials (or sometimes structures) on or inside the material. On the typical SOI-based photonic chips like

our design, it is realized by selectively etching Si on the top of SOI or depositing other material on the surface according to the design. Either etching or deposition is possible to create this wanted refractive index variation for grating design. If the index variation has a suitable period for the selected wavelength of light, a diffraction effect occurs. The diffraction behavior for a grating coupler can be described with the Bragg condition (also called the phase-matching condition). To achieve the first-order constructive interference with grating, the phase-matching condition should be considered, which is given as[130, 131]

$$P = \frac{\lambda}{n_{eff} - \sin\theta} \ , \tag{C.1}$$

where P is the grating period, λ is the input wavelength, θ is the incident angle, and n_{eff} is the effective refractive index of the waveguide mode on the grating coupler. This equation tells that for a certain grating period and incident angle, the obtained wavelength should satisfy the above Bragg condition. In addition, a high directionality requires both optimizations of the etch depth and grating period, as both of them can influence the value of n_{eff}. In addition, it's also important to realize the maximum mode overlap with the single-mode fiber and the grating.

To find the best parameters to meet the above condition and achieve the highest coupling efficiency, performing simulation as accurately as possible is always better, but this means we have to build a 3D model and run COMSOL simulations on those structures similar to the real case. However, due to memory requirements and time consumption, we will only restrict our simulations to two dimensions. In this case, there will be some tiny difference between the real situation and our simulations.

The geometry and definition of our COMSOL model are depicted in Figure C.2. The Si substrate is set at the bottom and colored blue, while on top of it is the silica cladding, with 1 μm thickness and is colored orange. The waveguide can be found with a thin line between the orange silica cladding and the green air above it. The gratings are present in the same line with the waveguide but with a periodic air region along with it. On top of the grating and inside the air domain, there is a fiber source with a thin rectangle that can be used to model the input light. The length of the waveguide and air region is set with the proper size to reduce the memory requirements. The gratings include 40 periods, which are large enough to cover the input light from the fiber.

In the real device, light is both transmitted through and reflected from the grating structures. Perfectly matched layer domains that can absorb all radiation are included at the edges of the air and Si regions, which aims to ensure that the same situation does not cause light to be reflected off the exterior edges of our model. Three ports include the fiber port for light emission, right and left ports that simulate the waveguide are defined in the model. These ports for the waveguide can be used to measure the light transmitted or reflected inside them with a boundary mode analysis step to mimic the mode of the waveguide. This ensures that we only include light coupled into the waveguide in our simulation like measurements in

experiments. COMSOL can be used to do boundary mode analyses for specified frequencies and refractive indices and find the supported waveguide mode(s). Note that the ports for the waveguide are always defined as much taller than the waveguide itself, which is aimed to ensure that we also include any evanescent components of the electromagnetic fields of the radiation propagating within the waveguide. The fiber port (long tiled rectangle in the center) is defined to both emit and absorb radiation by scattering boundary conditions. In addition to simulating the optical fiber output, we can also measure the amount of light that is reflected back towards the optical fiber by the grating structure if needed.

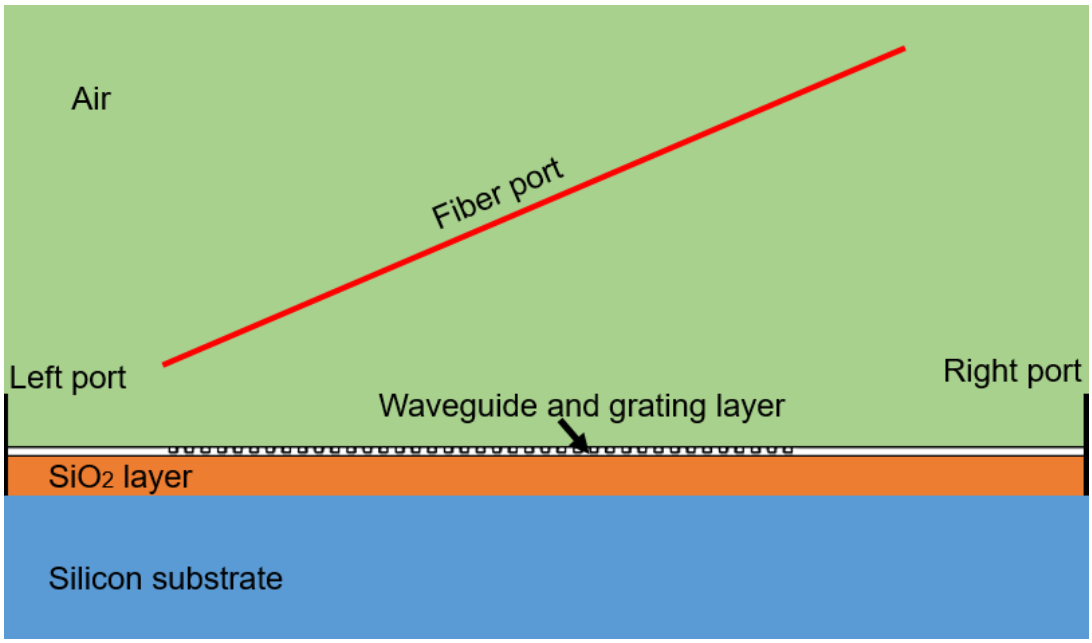

Figure C.2 Layout of the geometry and definition of the COMSOL model that is adapted to simulate the grating coupler in 2D. The colors are used to indicate different materials: The air region is colored green; the Si substrate is colored blue and the silica region is colored orange. The thin region between the SiO_2 and air is the waveguide and grating layer, with left and right ports are defined to monitor the power. The fiber region is colored red, which emits a Gaussian beam.

We run a parameter sweep of period and etching ratio in the study, this results in the uniform grating coupler (air and Si tooth have the same width). According to the optimization in previous work, the best coupling efficiency achieved for a completely uniform structure is around 40%. The relatively low efficiency is mainly caused by the energy loss to the bottom part, which can be further optimized through the turning of etching depth of grating (but also should consider the fabrication). The etching depth is then set to 140 nm, which can be fabricated by the etching step with resist as the mask and reduce the fabrication challenge. Similar to the full etched grating, run a parameter sweep of period and etching ratio. The highest coupling efficiency is realized for P = 580 nm, etching ratio of 0.5. The field distribution comparison for the highest efficiency in the two cases here verified that the loss at the bottom is highly reduced, which is mainly responsible for the efficiency improvement. We should note

that although further optimized designs like Chirped Grating with a varying period or covering the top with another thin matching layer can increase the coupling efficiency, this makes the fabrication too complex as we also need to fabricate TPhCs.

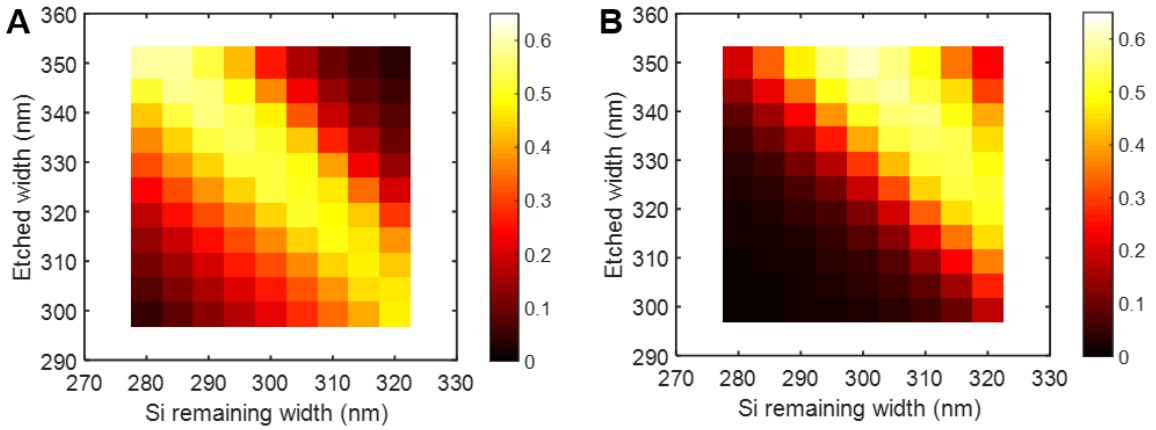

Figure C.3 Coupling efficiency from the right port under different etching ratios of Si for fiber inclined angles of 10 and 14 degrees. (A) the inclined angle of 10 degrees, (B) inclined angle of 14 degrees. An efficiency of around 65% can be achieved here.

We measured the grating coupling efficiency by calculating the intensity from the recorded images. The total efficiency (E) is

$$E = \frac{P_{out}}{P_{in} * t * 4} \tag{C.2}$$

where P_{out} is the intensity from the coupling-out spot, P_{in} is the intensity from an Ag mirror for normalization, and the t is the integration difference for recording the images. The 4 times relation arises as a polarizer is used before the Ag mirror to detect the reflection as for the polarized beam splitter. A grating coupling efficiency of around 30 – 40% is estimated based on our results.

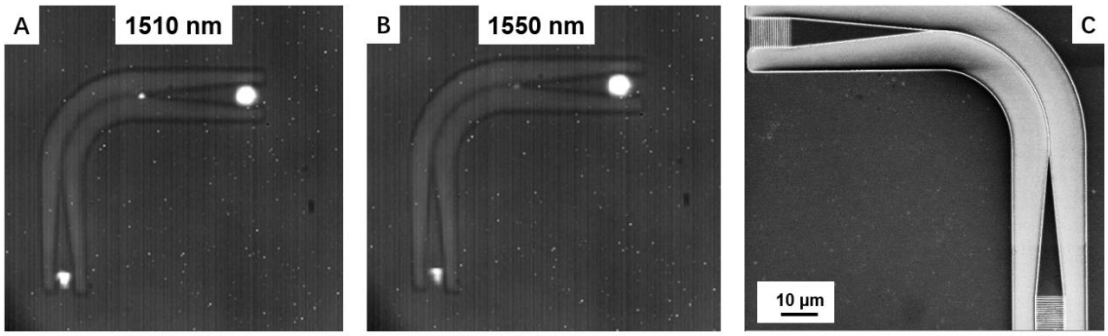

Figure C.4 Coupling efficiency of the grating measured at 1510 and 1550 nm as an example. (A and B) In recorded images from the grating, light coupling-out from the grating is observed from the two measured wavelengths at 1510 and 1550 nm. (C) SEM image of the fabricated grating for measuring.

D. Optimizing the fabrication of partly etched grating coupler

Based on the simulation above, a partly etched grating is useful for achieving high coupling efficiency. When the partly etched depth is around 120-220 nm, it can reduce the transmitted light to the bottom substrate. To reduce the fabrication complexity, we choose to use the resist mask as an etching mask directly. As shown in the optimization testing below, the resist mask with a thickness of around 600 nm can only protect a partly etch of 140 nm Si. This 600 nm resist is already quite thick, which makes it difficult to find the right position on the taper to start the fabrication under SEM images. On the other hand, a thicker resist could influence the shape of the grating as for the defocus of the electron beam.

In addition, as the grating is fabricated based on the structures from the first step, it's very crucial to remove the Cr mask completely and keep the surface as clean as possible. And any uncleaned particles on the grating area may influence the fabrication quality as shown below.

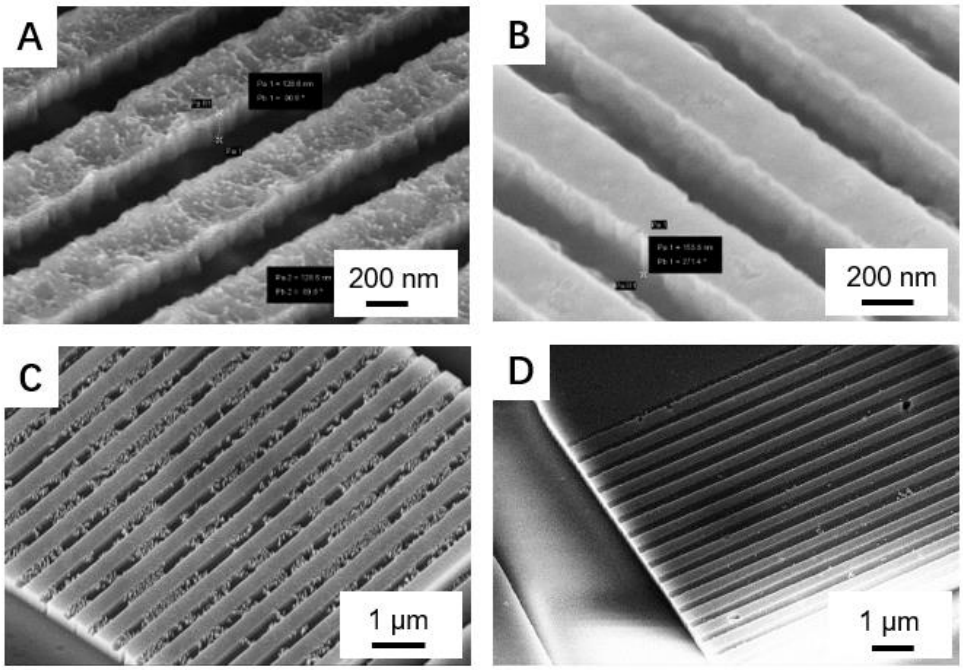

Figure D.1 SEM images during the optimization of the fabrication process. (A-B) The 600 nm resist mask can only provide etching protection when the etching depth is around 140 nm. (C-D) To completely remove the Cr mask from the previous step and keep the surface clean is extremely important for the fabrication of grating with good quality.

E. Reflective spectrum simulation with RCWA method

The rigorous coupled-wave analysis (RCWA), also known as the Fourier modal method or scattering matrix method, is another popular numerical method for numerically calculating the optical properties of stacked structures efficiently and simply.[132] For more details, if the structure needs to be simulated including an invariance in one spatial direction, the field distributions in this direction (both forward or backward) only acquire a change in the global amplitude and phase. Furthermore, if the system needs to be solved is periodic in the other two directions (like x and y-direction if the antennas are along the z-direction in our case), the eigenvalue problem is solved more efficiently by an expansion of the Fourier series. The solutions are so-called Fourier-Bloch modes and explain the origin of the name, Fourier modal method.

If we want to simulate the optical properties from several stacked layers including identical directions of invariance, the solutions of neighboring layers can then be combined by considering the corresponding correct boundary conditions. This requirement of periodicity restricts the Fourier modal method to some specific geometries but includes a correct formulation of periodic boundary conditions intrinsically at the same time. Most structures fabricated by EBL, are already limited to planar structures and meet the required condition with RCWA.

In our simulation, the optimal structure sizes showing a larger color change from air background to water were found for Si nanoantennas on an ITO substrate, with the refractive indexes are determined from our measured data. The square crossed nanoantenna with a width range from 200 nm to 700 nm is placed in the center of a quadratic unit cell with a periodicity of 800 nm. To keep the compatibility with top-down nano-fabrication, the parameter sweep for width is done while keeping the height and periodicity fixed. The calculated results can then be used to obtain the reflection or transmission spectral constructed from these antennas, with $T = \mathrm{abs}(t_{xx})^2$; $R = \mathrm{abs}(r_{xx})^2$; where t_{xx} or r_{xx} are get from the transmission matrix below:

$$t = \begin{pmatrix} t_{xx} & t_{yx} \\ t_{xy} & t_{yy} \end{pmatrix} \tag{E.1}$$

And the transmission or reflection matrix is $T = t_{xx}^2 = t_{yy}^2$ or $R = r_{xx}^2 = r_{yy}^2$, as square antennas are used in our simulation.

F. Scientific publications

Journal publication during the PhD period

1. **Jinlong Lu**†, Konstantin G. Wirth†, Wenlong Gao†, et al. Observing 0D subwavelength-localized modes at ~100 THz protected by weak topology. **Science Advances** 7, eabl3903 (2021).

2. **Jinlong Lu**, Basudeb Sain, Philip Georgi, et al. A versatile metasurface enabling superwettability for self-cleaning and dynamic color response. **Advanced Optical Materials** 2101781 (2021).

Conference contribution during the PhD period

1. **Jinlong Lu**, Konstantin G. Wirth, Wenlong Gao, et al. Robustness and versatility of subwavelength-localized modes protected by weak topology. OPTICS & PHOTONICS International Congress 2022.

Journal publication before the PhD period

1. **J Lu,** CV Ngo, SC Singh, et al. Bioinspired Hierarchical Surfaces Fabricated by Femtosecond Laser and Hydrothermal Method for Water Harvesting. Langmuir 35 (9), 3562-3567 (2019).

2. **J Lu,** J Yang, SC Singh, et al. Hierarchical micro/nanostructured TiO_2/Ag substrates based on femtosecond laser structuring: A facile route for enhanced SERS performance and location predictability. Applied Surface Science 478, 737-743 (2019).

3. **J Lu,** T Huang, Z Liu, et al. Long-term wettability of titanium surfaces by combined femtosecond laser micro/nano structuring and chemical treatments. Applied Surface Science 459, 257-262 (2018).

4. T Huang, **J Lu,** X Zhang, et al. Femtosecond Laser Fabrication of Anatase TiO_2 Micro-nanostructures with Chemical Oxidation and Annealing. Scientific reports 7 (1), 2089 (2017).

5. T Huang, **J Lu,** R Xiao, et al. Enhanced photocatalytic properties of hierarchical three-dimensional TiO_2 grown on femtosecond laser structured titanium substrate. Applied Surface Science 403, 584-589 (2017).

References

1. Bogaerts W*, et al.* Programmable photonic circuits. *Nature* **586**, 207-216 (2020).
2. Feldmann J*, et al.* Parallel convolutional processing using an integrated photonic tensor core. *Nature* **589**, 52-58 (2021).
3. Tan DTH. Topological Silicon Photonics. *Advanced Photonics Research* **2**, 2100010 (2021).
4. Wu Y, Li C, Hu X, Ao Y, Zhao Y, Gong Q. Applications of Topological Photonics in Integrated Photonic Devices. *Advanced Optical Materials* **5**, 1700357 (2017).
5. Silverstone JW*, et al.* On-chip quantum interference between silicon photon-pair sources. *Nature Photonics* **8**, 104-108 (2013).
6. Li FF*, et al.* Topological light-trapping on a dislocation. *Nature Communications* **9**, 2462 (2018).
7. Lu L, Joannopoulos JD, Soljačić M. Topological photonics. *Nature Photonics* **8**, 821-829 (2014).
8. Ozawa T*, et al.* Topological photonics. *Reviews of Modern Physics* **91**, 015006 (2019).
9. Wang Z, Chong Y, Joannopoulos JD, Soljacic M. Observation of unidirectional backscattering-immune topological electromagnetic states. *Nature* **461**, 772-775 (2009).
10. Ota Y, Katsumi R, Watanabe K, Iwamoto S, Arakawa Y. Topological photonic crystal nanocavity laser. *Communications Physics* **1**, 1-8 (2018).
11. Obana D, Liu F, Wakabayashi K. Topological edge states in the Su-Schrieffer-Heeger model. *Physical Review B* **100**, 075437 (2019).
12. Sabyasachi Barik AK, Christopher Flower, Tao Cai, Hirokazu Miyake, Wade DeGottardi, Mohammad Hafezi, Edo Waks. A topological quantum optics interface. *Science* **359**, 666–668 (2018).
13. Zhong H*, et al.* Topological Valley Hall Edge State Lasing. *Laser & Photonics Reviews* **14**, 2000001 (2020).
14. Zeng Y*, et al.* Electrically pumped topological laser with valley edge modes. *Nature* **578**, 246-250 (2020).
15. Xue H, Yang Y, Zhang B. Topological Valley Photonics: Physics and Device Applications. *Advanced Photonics Research* **2**, 2100013 (2021).
16. Yang Y*, et al.* Terahertz topological photonics for on-chip communication. *Nature Photonics* **14**, 446-451 (2020).

17. Du K, Barkaoui H, Zhang X, Jin L, Song Q, Xiao S. Optical metasurfaces towards multifunctionality and tunability. *Nanophotonics*, (2022), DOI: 10.1515/nanoph-2021-0684.

18. L. Zhu XL, B. Sain, M. Wang, C. Schlickriede, Y. Tang, J. Deng, K. Li, J. Yang, M. Holynski, S. Zhang, T. Zentgraf, K. Bongs, Y.-H. Lien, G. Li. A dielectric metasurface optical chip for the generation of cold atoms. *Science Advances* **6**, eabb6667 (2020).

19. Zhou H*, et al.* Dielectric Metasurfaces Enabled Ultradensely Integrated Multidimensional Optical System. *Laser & Photonics Reviews*, 2100521 (2022).

20. Atabaki AH*, et al.* Integrating photonics with silicon nanoelectronics for the next generation of systems on a chip. *Nature* **556**, 349-354 (2018).

21. Doerr CR. Silicon photonic integration in telecommunications. *Frontiers in Physics* **3**, 37 (2015).

22. Amiri IS*, et al.* Introduction to Photonics: Principles and the Most Recent Applications of Microstructures. *Micromachines (Basel)* **9**, 452 (2018).

23. Weimann C, Lauermann M, Hoeller F, Freude W, Koos C. Silicon photonic integrated circuit for fast and precise dual-comb distance metrology. *Optics Express* **25**, 30091-30104 (2017).

24. Hafezi M, Demler EA, Lukin MD, Taylor JM. Robust optical delay lines with topological protection. *Nature Physics* **7**, 907-912 (2011).

25. Haldane FD. Model for a quantum Hall effect without Landau levels: Condensed-matter realization of the "parity anomaly". *Physical Review Letters* **61**, 2015-2018 (1988).

26. Raghu S, Haldane FDM. Analogs of quantum-Hall-effect edge states in photonic crystals. *Physical Review A* **78**, 033834 (2008).

27. Shalaev MI, Walasik W, Tsukernik A, Xu Y, Litchinitser NM. Robust topologically protected transport in photonic crystals at telecommunication wavelengths. *Nature Nanotechnology* **14**, 31-34 (2019).

28. Zak J. Berry's phase for energy bands in solids. *Physical Review Letters* **62**, 2747-2750 (1989).

29. Khanikaev AB, Shvets G. Two-dimensional topological photonics. *Nature Photonics* **11**, 763-773 (2017).

30. Su WP, Schrieffer JR, Heeger AJ. Solitons in Polyacetylene. *Physical Review Letters* **42**, 1698-1701 (1979).

31. Asbóth JK, Oroszlány L, Pályi A. A Short Course on Topological Insulators: Band-structure topology and edge states in one and two dimensions. arXiv:1509.02295 (2015).

32. Zhang L*, et al.* Valley Kink States and Topological Channel Intersections in Substrate-

Integrated Photonic Circuitry. *Laser & Photonics Reviews* **13**, 1900159 (2019).

33. Kim M, Jacob Z, Rho J. Recent advances in 2D, 3D and higher-order topological photonics. *Light: Science & Applications* **9**, 130 (2020).
34. Wang M, Zhou W, Bi L, Qiu C, Ke M, Liu Z. Valley-locked waveguide transport in acoustic heterostructures. *Nature Communications* **11**, 3000 (2020).
35. Xiong H*, et al.* Topological Valley Transport of Terahertz Phonon–Polaritons in a LiNbO3 Chip. *ACS Photonics* **8**, 2737-2745 (2021).
36. Ma J, Xi X, Sun X. Topological Photonic Integrated Circuits Based on Valley Kink States. *Laser & Photonics Reviews* **13**, 1900087 (2019).
37. He XT*, et al.* A silicon-on-insulator slab for topological valley transport. *Nature Communications* **10**, 872 (2019).
38. He L, Ji HY, Wang YJ, Zhang XD. Topologically protected beam splitters and logic gates based on two-dimensional silicon photonic crystal slabs. *Optics Express* **28**, 34015-34023 (2020).
39. Jalali Mehrabad M*, et al.* Chiral topological photonics with an embedded quantum emitter. *Optica* **7**, 1690 (2020).
40. Xie X*, et al.* Topological Cavity Based on Slow-Light Topological Edge Mode for Broadband Purcell Enhancement. *Physical Review Applied* **16**, 014036 (2021).
41. Zhao H*, et al.* Topological hybrid silicon microlasers. *Nature Communications* **9**, 981 (2018).
42. Zhang W*, et al.* Low-threshold topological nanolasers based on the second-order corner state. *Light: Science & Applications* **9**, 109 (2020).
43. Gong Y, Wong S, Bennett AJ, Huffaker DL, Oh SS. Topological Insulator Laser Using Valley-Hall Photonic Crystals. *ACS Photonics* **7**, 2089-2097 (2020).
44. Ma J*, et al.* Room-temperature continuous-wave Dirac-vortex topological lasers on silicon. arXiv:2106.13838 (2021).
45. Jiang Z, Ding Y, Xi C, He G, Jiang C. Topological protection of continuous frequency entangled biphoton states. *Nanophotonics* **10**, 4019-4026 (2021).
46. Chen Y*, et al.* Topologically protected valley-dependent quantum photonic circuits. arXiv:2103.06686 (2021).
47. Elshaari AW, Pernice W, Srinivasan K, Benson O, Zwiller V. Hybrid integrated quantum photonic circuits. *Nature Photonics* **14**, 285-298 (2020).
48. Arbabi A, Horie Y, Bagheri M, Faraon A. Dielectric metasurfaces for complete control of phase and polarization with subwavelength spatial resolution and high transmission.

Nature Nanotechnology **10**, 937-943 (2015).

49. Huang L*, et al.* Dispersionless phase discontinuities for controlling light propagation. *Nano Letters* **12**, 5750-5755 (2012).

50. Li G, Zhang S, Zentgraf T. Nonlinear photonic metasurfaces. *Nature Reviews Materials* **2**, 17010 (2017).

51. Zheng G, Muhlenbernd H, Kenney M, Li G, Zentgraf T, Zhang S. Metasurface holograms reaching 80% efficiency. *Nature Nanotechnology* **10**, 308-312 (2015).

52. Hu T*, et al.* CMOS-compatible a-Si metalenses on a 12-inch glass wafer for fingerprint imaging. *Nanophotonics* **9**, 823-830 (2020).

53. Leitis A*, et al.* All-Dielectric Programmable Huygens' Metasurfaces. *Advanced Functional Materials* **30**, 1910259 (2020).

54. Hu Y*, et al.* Trichromatic and Tripolarization-Channel Holography with Noninterleaved Dielectric Metasurface. *Nano Letters* **20**, 994-1002 (2020).

55. Sain B, Meier C, Zentgraf T. Nonlinear optics in all-dielectric nanoantennas and metasurfaces: a review. *Advanced Photonics* **1**, 024002 (2019).

56. Chantakit T*, et al.* All-dielectric silicon metalens for two-dimensional particle manipulation in optical tweezers. *Photonics Research* **8**, 1435 (2020).

57. Chen WT*, et al.* A broadband achromatic metalens for focusing and imaging in the visible. *Nature Nanotechnology* **13**, 220 (2018).

58. Arbabi E, Arbabi A, Kamali SM, Horie Y, Faraji-Dana M, Faraon A. MEMS-tunable dielectric metasurface lens. *Nature Communications* **9**, 812 (2018).

59. Lim KTP, Liu H, Liu Y, Yang JKW. Holographic colour prints for enhanced optical security by combined phase and amplitude control. *Nature Communications* **10**, 25 (2019).

60. Wen D, Cadusch JJ, Meng J, Crozier KB. Multifunctional Dielectric Metasurfaces Consisting of Color Holograms Encoded into Color Printed Images. *Advanced Functional Materials* **30**, 1906415 (2019).

61. X. Li LC, Y. Li, X. Zhang, M. Pu, Z. Zhao, X. Ma, Y. Wang, M. Hong, X. Luo. Multicolor 3D meta-holography by broadband plasmonic modulation. *Science Advances* **2**, e1601102 (2016).

62. Wei Q*, et al.* Simultaneous Spectral and Spatial Modulation for Color Printing and Holography Using All-Dielectric Metasurfaces. *Nano Letters* **19**, 8964-8971 (2019).

63. Yang W*, et al.* All-dielectric metasurface for high-performance structural color. *Nature Communications* **11**, 1864 (2020).

64. Frank Neubrech XD, Na Liu. Dynamic plasmonic color generation enabled by functional

materials. *Science Advances* **6**, eabc2709 (2020).

65. Li J, Chen Y, Hu Y, Duan H, Liu N. Magnesium-Based Metasurfaces for Dual-Function Switching between Dynamic Holography and Dynamic Color Display. *ACS Nano* **14**, 7892-7898 (2020).

66. Sun S*, et al.* Real-Time Tunable Colors from Microfluidic Reconfigurable All-Dielectric Metasurfaces. *ACS Nano* **12**, 2151-2159 (2018).

67. Checcucci S, Bottein T, Gurioli M, Favre L, Grosso D, Abbarchi M. Multifunctional Metasurfaces Based on Direct Nanoimprint of Titania Sol–Gel Coatings. *Advanced Optical Materials* **7**, 1801406 (2019).

68. Li J, Yu P, Zhang S, Liu N. A Reusable Metasurface Template. *Nano Letters* **20**, 6845-6851 (2020).

69. Chen C*, et al.* In Situ Electric-Induced Switchable Transparency and Wettability on Laser-Ablated Bioinspired Paraffin-Impregnated Slippery Surfaces. *Advanced Science* **8**, 2100701 (2021).

70. Liu B, He Y, Wong SW, Li Y. Multifunctional Vortex Beam Generation by a Dynamic Reflective Metasurface. *Advanced Optical Materials* **9**, 2001689 (2020).

71. Wu Y*, et al.* Self-Cleaning Titanium Dioxide Metasurfaces with UV Irradiation. *Laser & Photonics Reviews* **15**, 2000330 (2020).

72. Zhao F*, et al.* Metalens-Assisted System for Underwater Imaging. *Laser & Photonics Reviews* **15**, 2100097 (2021).

73. Zuo Y, Zheng L, Zhao C, Liu H. Micro-/Nanostructured Interface for Liquid Manipulation and Its Applications. *Small* **16**, e1903849 (2020).

74. Wu Y, Chen Y, Song Q, Xiao S. Dynamic Structural Colors Based on All-Dielectric Mie Resonators. *Advanced Optical Materials* **9**, 2002126 (2021).

75. Li Z, Wan C, Dai C, Zhang J, Zheng G, Li Z. Actively Switchable Beam-Steering via Hydrophilic/Hydrophobic-Selective Design of Water-Immersed Metasurface. *Advanced Optical Materials* **9**, 2100297 (2021).

76. Pimpin A, Srituravanich W. Review on Micro- and Nanolithography Techniques and their Applications. *Engineering Journal* **16**, 37-56 (2012).

77. Huff M. Recent Advances in Reactive Ion Etching and Applications of High-Aspect-Ratio Microfabrication. *Micromachines* **12**, 991 (2021).

78. Gopinath A, Miyazono E, Faraon A, Rothemund PW. Engineering and mapping nanocavity emission via precision placement of DNA origami. *Nature* **535**, 401-405 (2016).

79. Hennessy K*, et al.* Quantum nature of a strongly coupled single quantum dot-cavity

system. *Nature* **445**, 896-899 (2007).

80. Jin J, Yin X, Ni L, Soljacic M, Zhen B, Peng C. Topologically enabled ultrahigh-Q guided resonances robust to out-of-plane scattering. *Nature* **574**, 501-504 (2019).

81. Yamamoto T, Pashkin YA, Astafiev O, Nakamura Y, Tsai JS. Demonstration of conditional gate operation using superconducting charge qubits. *Nature* **425**, 941-944 (2003).

82. Chen XD, Deng WM, Shi FL, Zhao FL, Chen M, Dong JW. Direct Observation of Corner States in Second-Order Topological Photonic Crystal Slabs. *Physical Review Letters* **122**, 233902 (2019).

83. Gao X*, et al.* Dirac-vortex topological cavities. *Nature Nanotechnology* **15**, 1012-1018 (2020).

84. Ota Y*, et al.* Photonic crystal nanocavity based on a topological corner state. *Optica* **6**, 786 (2019).

85. Soljacic MJ, JD. Enhancement of nonlinear effects using photonic crystals. *Nature Materials* **3**, 211-219 (2004).

86. Song B-S, Noda S, Asano T, Akahane Y. Ultra-high-Q photonic double-heterostructure nanocavity. *Nature Materials* **4**, 207-210 (2005).

87. Kim HR, Hwang MS, Smirnova D, Jeong KY, Kivshar Y, Park HG. Multipolar lasing modes from topological corner states. *Nature Communications* **11**, 5758 (2020).

88. Kruk SS, Gao W, Choi DY, Zentgraf T, Zhang S, Kivshar Y. Nonlinear Imaging of Nanoscale Topological Corner States. *Nano Letters* **21**, 4592-4597 (2021).

89. Xie B*, et al.* Higher-order quantum spin Hall effect in a photonic crystal. *Nature Communications* **11**, 3768 (2020).

90. Grinberg IH, Lin M, Benalcazar WA, Hughes TL, Bahl G. Trapped State at a Dislocation in a Weak Magnetomechanical Topological Insulator. *Physical Review Applied* **14**, 064042 (2020).

91. Noh J*, et al.* Topological protection of photonic mid-gap defect modes. *Nature Photonics* **12**, 408-415 (2018).

92. Peterson CW, Li T, Jiang W, Hughes TL, Bahl G. Trapped fractional charges at bulk defects in topological insulators. *Nature* **589**, 376-380 (2021).

93. Atala M*, et al.* Direct measurement of the Zak phase in topological Bloch bands. *Nature Physics* **9**, 795-800 (2013).

94. Mermin ND. The topological theory of defects in ordered media. *Reviews of Modern Physics* **51**, 591-648 (1979).

95. Ran Y. Weak indices and dislocations in general topological band structures.

arXiv:1006.5454 (2010).

96. Arora S, Bauer T, Barczyk R, Verhagen E, Kuipers L. Direct quantification of topological protection in symmetry-protected photonic edge states at telecom wavelengths. *Light: Science & Applications* **10**, 9 (2021).

97. Vakulenko A*, et al.* Near-Field Characterization of Higher-Order Topological Photonic States at Optical Frequencies. *Advanced Materials* **33**, e2004376 (2021).

98. Dubrovkin AM*, et al.* Near-field mapping of the edge mode of a topological valley slab waveguide atλ=1.55μm. *Applied Physics Letters* **116**, 191105 (2020).

99. Wirth KG*, et al.* Tunable s-SNOM for Nanoscale Infrared Optical Measurement of Electronic Properties of Bilayer Graphene. *ACS Photonics* **8**, 418-423 (2021).

100. Richards D, Zayats A, Keilmann F, Hillenbrand R. Near-field microscopy by elastic light scattering from a tip. *Philosophical Transactions of the Royal Society of London Series A: Mathematical, Physical and Engineering Sciences* **362**, 787-805 (2004).

101. Heßler A*, et al.* In3SbTe2 as a programmable nanophotonics material platform for the infrared. *Nature Communications* **12**, 924 (2021).

102. Michel AU*, et al.* Advanced Optical Programming of Individual Meta-Atoms Beyond the Effective Medium Approach. *Advanced Materials* **31**, e1901033 (2019).

103. Wuttig M, Bhaskaran H, Taubner T. Phase-change materials for non-volatile photonic applications. *Nature Photonics* **11**, 465-476 (2017).

104. Benson O. Assembly of hybrid photonic architectures from nanophotonic constituents. *Nature* **480**, 193-199 (2011).

105. Najer D*, et al.* A gated quantum dot strongly coupled to an optical microcavity. *Nature* **575**, 622-627 (2019).

106. Kim J-H, Aghaeimeibodi S, Carolan J, Englund D, Waks E. Hybrid integration methods for on-chip quantum photonics. *Optica* **7**, 291 (2020).

107. Cheng Z, Zhang D, Luo X, Lai H, Liu Y, Jiang L. Superwetting Shape Memory Microstructure: Smart Wetting Control and Practical Application. *Advanced Materials* **33**, e2001718 (2021).

108. Wang D*, et al.* Design of robust superhydrophobic surfaces. *Nature* **582**, 55-59 (2020).

109. Chen Y*, et al.* Bioinspired Superwettable Microspine Chips with Directional Droplet Transportation for Biosensing. *ACS Nano* **14**, 4654-4661 (2020).

110. Zhang X*, et al.* Bioinspired Tunable Structural Color Film with Janus Wettability and Interfacial Floatability towards Visible Water Quality Monitoring. *Advanced Functional Materials*, 2010406 (2021).

111. Mohd-Noor S*, et al.* Ultrafast humidity-responsive structural colors from disordered nanoporous titania microspheres. *Journal of Materials Chemistry A* **7**, 10561-10571 (2019).

112. Wen H*, et al.* Reversible data encryption-decryption using a pH stimuli-responsive hydrogel. *Journal of Materials Chemistry C* **9**, 2455-2463 (2021).

113. Yu Wang LS, Guopu Chen, Lingyu Sun, Xiaoxuan Zhang, Yuanjin Zhao. Bioinspired structural color patch with anisotropic surface adhesion. *Science Advances* **6**, eaax8258 (2020).

114. Rombaut J, Martínez S, Matera UM, Mazumder P, Pruneri V. Antireflective Multilayer Surface with Self-Cleaning Subwavelength Structures. *ACS Photonics* **8**, 894-900 (2021).

115. Reiner Fürstner WB. Wetting and Self-Cleaning Properties of Artificial Superhydrophobic Surfaces. *Langmuir* **21**, 956-961 (2005).

116. Sun RZ, Bai H, Ju J, Jiang L. Droplet emission induced by ultrafast spreading on a superhydrophilic surface. *Soft Matter* **9**, 9285-9289 (2013).

117. Rong Wang KH, Akira Fujishima. Light-induced amphiphilic surfaces. *Nature* **299**, 431-432 (1997).

118. Su B, Tian Y, Jiang L. Bioinspired Interfaces with Superwettability: From Materials to Chemistry. *Journal of the American Chemical Society* **138**, 1727-1748 (2016).

119. Xintong Zhang MJ, Zhaoyue Liu, Donald A. Tryk, Shunsuke Nishimoto, Taketoshi Murakami, and Akira Fujishima. Superhydrophobic TiO2 Surfaces: Preparation, Photocatalytic Wettability Conversion, and Superhydrophobic-Superhydrophilic Patterning. *The Journal of Physical Chemistry C* **111**, 14521-14529 (2007).

120. Milles S, Soldera M, Kuntze T, Lasagni AF. Characterization of self-cleaning properties on superhydrophobic aluminum surfaces fabricated by direct laser writing and direct laser interference patterning. *Applied Surface Science* **525**, 146518 (2020).

121. Yang JH, Babicheva VE, Yu MW, Lu TC, Lin TR, Chen KP. Structural Colors Enabled by Lattice Resonance on Silicon Nitride Metasurfaces. *ACS Nano* **14**, 5678-5685 (2020).

122. Bao Y, Yan J, Yang X, Qiu CW, Li B. Point-Source Geometric Metasurface Holography. *Nano Letters* **21**, 2332-2338 (2021).

123. Peeters H*, et al.* Plasmonic gold-embedded TiO2 thin films as photocatalytic self-cleaning coatings. *Applied Catalysis B: Environmental* **267**, 118654 (2020).

124. Lu J, Huang T, Liu Z, Zhang X, Xiao R. Long-term wettability of titanium surfaces by combined femtosecond laser micro/nano structuring and chemical treatments. *Applied Surface Science* **459**, 257-262 (2018).

125. Zhang X, Guo Y, Zhang Z, Zhang P. Self-cleaning superhydrophobic surface based on

titanium dioxide nanowires combined with polydimethylsiloxane. *Applied Surface Science* **284**, 319-323 (2013).

126. Ren-De Sun AN, Akira Fujishima, Toshiya Watanabe, and Kazuhito Hashimoto. Photoinduced Surface Wettability Conversion of ZnO and TiO2 Thin Films. *The Journal of Physical Chemistry B* **105**, 1984-1990 (2001).

127. Yunkai Wu WY, Yubin Fan, Qinghai Song, Shumin Xiao. TiO2 metasurfaces: From visible planar photonics to photochemistry. *Science Advances* **5**, eaax0939 (2019).

128. Semmlinger M*, et al.* Generating Third Harmonic Vacuum Ultraviolet Light with a TiO2 Metasurface. *Nano Letters* **19**, 8972-8978 (2019).

129. Wang C, Zhang H, Yuan H, Zhong J, Lu C. Universal numerical calculation method for the Berry curvature and Chern numbers of typical topological photonic crystals. *Frontiers of Optoelectronics* **13**, 73-88 (2020).

130. Zhang Z*, et al.* High-efficiency apodized bidirectional grating coupler for perfectly vertical coupling. *Optics Letters* **44**, 5081-5084 (2019).

131. Khoo E, Liu A, Wu J. Nonuniform photonic crystal taper for high-efficiency mode coupling. *Optics Express* **13**, 7748-7759 (2005).

132. Weiss T. Advanced numerical and semi-analytical scattering matrix calculations for modern nano-optics. *PHD thesis, University of Stuttgart*, (2011).